Domain Broadening in Periodic Poling of Thinned Lithium Niobate and Spectroscopic Methods for Whole Blood Analysis

Peter S. Bullen

Submitted in partial fulfillment of the
requirements for the degree of
Doctor of Philosophy
in the Graduate School of Arts and Sciences

COLUMBIA UNIVERSITY
2019

ABSTRACT

Domain Broadening in Periodic Poling of Thinned Lithium Niobate and Spectroscopic Methods for Whole Blood Analysis

Peter S. Bullen

This dissertation is divided into two separate parts covering my research in two different fields of optics. Part I consists of chapters 1-3 and covers experiments on periodically poled lithium niobate while Part II consists of chapters 4-6 and covers various spectroscopic methods designed for the application of in vivo blood analysis. Chapter 1 serves as a brief introduction to periodically poled lithium niobate and its fabrication process. In chapter 2, the key results of Part I, derived from a series of experiments on poling of thinned lithium niobate, are presented. Building upon these experiments, chapter 3 concludes Part I with a study on poling of crystal ion sliced lithium niobate. Part II begins with chapter 4, which describes a spectroscopic approach for non-invasive blood analysis in vivo. In chapter 5, experiments analyzing aqueous glucose solutions with mid-infrared and Raman spectroscopy are discussed. Chapter 6 concludes this dissertation with the design and demonstration of a innovative stimulated Raman spectroscopy system.

In Part I, ferroelectric poling fabrication procedures were developed, optimized, and implemented for periodic poling of thinned lithium niobate. The free-standing samples of thickness from 500 μm down to 25 μm were thinned by chemical mechanical planarization and annealed before poling. Domain structure was investigated as a function of sample thickness using Raman, scanning electron, atomic force, and optical microscopy, and broadening of poled domains was consistently found to vary with sample thickness in a strong linear correlation. Domain broadening was reduced by 38% as the thickness of the poled sample was reduced from 500 to 25 μm. Micro Raman probe measurements showed a thickness-dependent contrast in Raman active mode intensity between poled and unpoled regions, with the thinner samples having a higher intensity contrast.

To explore poling on even thinner free-standing samples, crystal ion sliced lithium niobate thin films of 10 μm in thickness were fabricated. Chemical mechanical planarization of the ion-implanted layer and annealing was performed to prepare the thin films for poling. Ferroelectric poling of the crystal ion sliced samples was attempted, but unsuccessful, suggesting that alternative fabrication processes may be necessary for poling of crystal ion sliced thin films.

In Part II, several disparate experiments were conducted to progress towards a common overarching goal of developing a spectroscopic method for non-invasive whole blood analysis and metabolite monitoring. A portable visible and near-infrared spectroscopy system for in vivo blood spectral identification was developed and demonstrated in a clinical setting. A custom-designed clip attached the illumination and collection optics to opposite sides of the patients' fifth fingertip, and applied gentle pressure, gradually pushing a small quantity of blood away from the measurement site, and inducing a time-dependent change in the effective path length of blood. Time-dependent visible and near-infrared spectra were measured from the collected transmitted and scattered light. A maximum likelihood model was developed to leverage the time-dependent spectral component and identify the spectrum of blood, isolating it from that of surrounding tissue.

A second set of experiments were conducted to develop a model for predicting glucose concentrations from measured mid-infrared transmission and spontaneous Raman scattering spectra. Partial least squares regression models were trained, validated, and tested on the spectra of aqueous 0-10 mM glucose solutions measured by both spectroscopic modalies. The models proved to be accurate predictors of glucose concentration as the mean squared error of the model based on mid-infrared spectra ranged from 0.10 - 0.74 mM, and that of the Raman-based model ranged from 0.26 - 0.93 mM.

Finally, an LED-based stimulated Raman system was innovated to improve upon the relatively weak spontaneous Raman signal in a cost-effective manner. Stimulated Raman gain using a broadband LED Stokes source was demonstrated in the measuring of vibrational spectra of aqueous 0-10 mM glucose solutions. Scattered light was detected via photomultiplier tube and measured using either a photon counter or a lock-in amplifier in two alternative versions of the system. Both

stimulated and spontaneous Raman spectra were collected with each instrument for a total of four measurement modalities. The stimulated Raman spectra measured with the photon counter showed up to 100% higher intensity for some glucose modes compared to the corresponding spontaneous Raman spectra, but also had significantly greater noise. For the spectra measured with the lock-in amplifier, the glucose modes of the stimulated Raman spectra were only 20-30% higher in intensity than those of the spontaneous Raman spectra, but had similar levels of noise. Partial least squares regression models based on spectra measured by each modality were developed and compared. The model based on stimulated Raman spectra measured with the lock-in amplifier had the strongest predictive power of all modalities and predicted the concentrations of the aqueous 0-10 mM glucose solutions with a mean squared error as low as 9.96×10^{-4} mM, an order of magnitude lower than that of the model based on spontaneous Raman spectra.

Contents

List of Figures iv

Abbreviations xii

Acknowledgements xiii

Dedication xv

Preface xvi

Part I

Domain Broadening in Periodic Poling of Thinned Lithium Niobate

1 Periodically Poled Lithium Niobate

1.1 Introduction 2

1.2 Fabrication 2

1.3 References 6

2 Domain Broadening in Thinned Lithium Niobate

2.1 Introduction 8

2.2 Visualization and Measuring of Domains 9

2.3 Poling Voltage 10

2.4 Domain Broadening 12

2.5 Micro Raman Measurements 15

2.6 Conclusion 21

2.7 References 21

3 Poling in Crystal Ion Sliced Lithium Niobate

3.1 Introduction 25
3.2 Fabrication 26
3.3 Poling 29
3.4 Discussion 32
3.5 References 33

Part II

Spectroscopic Methods for Whole Blood Analysis

4 Apparatus for Portable In Vivo Blood Spectroscopic Analysis with Pressure Induced Time-Dependent Component

4.1 Introduction 36
4.2 Portable Spectroscopy System 39
4.3 Measurement Procedure 41
4.4 Computational Methods 43
4.5 Results 44
4.6 Discussion 48
4.7 Human Subjects 50
4.8 References 50

5 Vibrational Spectroscopy for Analysis of Glucose Solutions

5.1 Introduction 53
5.2 MIR Experiment 54
5.3 Spectral Processing and Modeling 56
5.4 Raman Experiment 57
5.5 Discussion 62
5.6 References 63

6 Stimulated Raman Spectroscopy with LED Broadband Stokes Source

6.1 Introduction 64
6.2 Optical Setup 67
6.3 Stimulated Raman Measurements 70
6.4 Experimental Process 74
6.5 Spontaneous and Stimulated Raman Comparison 75
6.6 Partial Least Squares Regression Model 79
6.7 Discussion 82
6.8 Temperature Stability 84
6.9 References 85

List of Figures

Figure 1.1 3
Schematic of the poling setup. The external voltage is applied across the crystal via a lithium chloride solution in contact with the bare regions (i.e., regions where the resist is absent) of the surface. The materials used in the poling process are labeled in the figure.

Figure 1.2: 5
Plot of a typical poling waveform, i.e., voltage vs. time. When the voltage crosses a critical threshold value, a current spike is seen, indicating the onset of poling current. The inset shows an expanded waveform for both current and voltage.

Figure 2.1: 11
The measured poling voltage vs. sample thickness. Notice that the y-axis intercept does not intersect the origin. Thickness error bars are standard deviations from a set of multiple thickness measurements at different locations for each sample. The voltage error bars are determined from the poling voltage step size. The three green triangles towards the lower left corner of the graph correspond to samples from earlier experiments conducted with a less refined polishing technique. The error margin for these three data points was ±0.1 kV and less than ±5 μm. Error bars were removed for visual clarity.

Figure 2.2 13
Domain width vs. thickness. Both the error bars for the domain width and thickness are standard deviations obtained from a set of multiple measurements, as explained in the caption of Figure 2.1. The inset shows the electric field plot obtained with a high-resolution finite element method Poisson computation for the field in the vicinity of the

photoresist opening in the surface mask; the sample is 25 μm thick, and the opening is 9.3 μm in width.

Figure 2.3: 14
(a) SEM cross-section images of poled domains revealed by HF etching. For the 500-μm-thick sample, the domains are clearly wider than the domains in the 150 or 25-μm-thick sample domains. The etching between poled and non-poled domains appears different in this figure because the Y+ face is shown for the 25 and 150-μm samples while the Y- face is shown for the 500-μm sample. Panels (b) and (c) show zoomed out SEM images showing the full cross-section from Z+ to Z- sides with (b) 150-μm and (c) 500-μm-thick samples, respectively. The uniformity of domain width through the depth of the crystal is seen.

Figure 2.4: 17
A Raman scan using 5 different Raman wavelengths along the top surface of a poled 150 μm sample with the scan direction perpendicular to the long axis of the poling stripe. This microscope image of the poled sample surface shows the path of the scan (horizontal line) and poled (P) and non-poled (N-P) regions.

Figure 2.5: 19
Raman images of a poled 150-μm-thick sample at the Raman modes shown in the white boxes. Spatial dimensions are in μm. Note the relative uniformity of the poled region.

Figure 3.1: 26
SRIM implantation depth simulation showing the distribution in stopping depth of helium ions implanted in lithium niobate. The initial energy of the ions was 3.6 MeV, and the average stopping depth was about 10 μm. The simulation shows that the ions are highly concentrated around the mean stopping distance, which results in a thin ion implanted layer.

Figure 3.2: 27
Ion beam at University of Albany. This Dynamitron has six installed beamlines, one of which is used for ion implantation. We sent 3.6 MeV helium ions at a dosage of $5x10^{16}$ ions/cm^2 into the Z+ surface of our lithium niobate samples.

Figure 3.3: 29
Optical micrograph of the Z- surface of a 10-μm-thick CIS-LNO thin film sample. The micro-channels of the implantation layer are visible on this annealed sample before undergoing the CMP polishing process.

Figure 3.4: 31
10-μm-thick crystal-ion-sliced lithium niobate thin film (LNTF) sample wax-mounted on glass substrate over 3-mm-diameter through-sample via. This particular sample has been polished to remove micro-channels from the Z- surface and annealed afterwards to relieve strain. A layer of patterned photoresist covers the sample and specifies the intended periodic poling pattern.

Figure 4.1: 40
(a) Spectroscopy system setup diagram. The spectrometers, microcontroller and associated circuitry, and halogen lamp are all enclosed in a plastic container for protection and efficient disinfecting. (b) Spectroscopy system on portable cart for convenient transport between patients. The laptop computer rests on the plastic container, and the UPS is enclosed in the lower compartment of the cart.

Figure 4.2: 42
Clip design for (a) visible and (b) NIR spectral measurements. The visible design includes the LED light source on the clip itself while the halogen lamp, which acts as the NIR light source, is positioned on the cart, and the light is directed to the clip via liquid light guide.

Figure 4.3: 43
L2-norm of (a) visible and (b) NIR spectra over time. Both spectra increase gradually with time due to the decreasing effective path length of blood. The rate of increase in spectral intensity ranges from about 0.1-0.2% per second for the visible spectrum and 0.03-0.07% per seoncd for the NIR spectrum.

Figure 4.4: 45
(a) Measured visible transmission spectrum (at t=0). (b) Absorption spectrum of blood extracted from time-dependent component of the visible measurement. The spectral peaks at 528 and 568 nm correspond to absorption peaks of hemoglobin. Although the total measured signal is low at these peaks, the time-dependent character was modeled. The regions of high noise on the sides of the blood spectrum correspond to regions of the spectrum outside the bandwidth of the light source.

Figure 4.5: 47
(a) Measured NIR transmission spectrum. (b) Absorption spectrum of blood extracted from time-dependent component of the NIR measurement. In contrast to the visible spectra, due to less absorption by skin and other surrounding tissue, the NIR absorption spectrum of blood is similar to the inverse of the measured transmission spectrum.

Figure 5.1: 55
MIR glucose spectra with concentrations 0-10 mM. (a) Full spectrum from 600-3600 cm^{-1}. Although the 10 spectra are similar and appear to overlap, there are subtle differences due to glucose concentration, especially in the 1000-1250 cm^{-1} and 2400-2700 cm^{-1} wavenumber ranges. (b) Zoomed in spectrum from approximately 1000-1250 cm^{-1}. The spectra of higher glucose concentrations have lower intensity in this range, indicating lower transmission or greater absorption due to interactions with glucose.

Figure 5.2: 57
PLS glucose concentration prediction based on MIR spectra. Each point represents the glucose concentration prediction of the PLS model using the spectrum from a solution from the testing set. The line represents an idealized glucose prediction model. The data points are generally close to the idealized line, with the greatest deviations being on the order of tenths of mM. The mean squared error is 0.10 mM, indicating the high accuracy of the model.

Figure 5.3: 58
Raman spectra of glucose solutions up to 1000 mM in concentration. The high variation in concentration allows better examination of spectral features corresponding to aqueous glucose. Key features include those at the 1124 cm^{-1} mode and the group of modes at approximately 407, 492, and 592 cm^{-1}.

Figure 5.4: 59
Raman spectra of glucose solutions with concentrations 0-10 mM. (a) Full spectrum from about 200-1850 cm^{-1}. Small variations can be seen throughout the spectrum, but especially in the 400-600 cm^{-1} wavenumber range. (b) Zoomed in spectrum. Spectra of higher glucose concentration generally have higher intensity in this range, corresponding to glucose Raman modes.

Figure 5.5: 61
Glucose concentration predictions based on Raman spectra of solutions with glucose concentrations from 0 to 10 mM. Each point represents the glucose concentration prediction of the PLS model using the spectrum from a solution from the testing set. The line represents the concentration predictions of an idealized PLS model. The predictions of our Raman-based PLS model are highly accurate for most of the solutions, except for the 3 mM solution. Inaccuracies such as this are to be expected given the small training set of only 11 solutions, and may be due to slight variations in the positioning of the

cuvettes in the measurement system. The mean squared error of the PLS model represented here is 0.26 mM. With a different combination of training, validation, and testing sets, the mean squared error of the PLS model varied as high as 0.93 mM, indicating the accuracy of the model is partially dependant on data set.

Figure 6.1: 68
Stimulated Raman Spectroscopy system diagram. The beams from the excitation laser and LED are combined via dichroic beam splitter and focused into the sample. Scattered light is ultimately detected by Photomultiplier Tube (PMT) and measured using either a photon counter or lock-in amplifier. The optical chopper is only used in conjunction with the lock-in amplifier and provides the reference frequency. PD = photodiode, BS = beam splitter, MR = mirror, AS = aperture stop, LF = line filter, DC = dichroic beam splitter, LN = lens, SA = sample, CL = collimating/coupling lens, LP = longpass filter, PL = polarizer, MT = optical fiber mount

Figure 6.2: 71
Natural logarithm of Raman gain as a function of pump power for 1062 cm^{-1} mode in methanol. The natural logarithm follows a linear trend with respect to pump power with R^2 value of 0.995, indicating that the variation between Raman gain and pump power may be modeled by exponential fit. However, the Raman gain itself also follows a linear trend with respect to pump power with R^2 value of .993, indicating that the Raman gain may appropriately be modeled by its first-order expansion in equation (3) at these pump power levels.

Figure 6.3: 73
(a) Combined (pump laser and Stokes LED) and Stokes (only Stokes LED) signals for 10 mM glucose sample measured via photon counter. (b) Unnormalized Stimulated Raman Gain signal is approximated as the difference between the combined and Stokes signals.

Figure 6.4: 76
Comparison of stimulated and spontaneous Raman spectra of a 10 mM glucose solution measured with (a) photon counter and (b) lock-in amplifier. The enhancement between stimulated and spontaneous spectra is greater with the photon counter spectra, but the stimulated photon counter spectra also has significantly higher noise.

Figure 6.5: 78
(a) Photon counter spontaneous, (b) photon counter stimulated, (c) lock-in spontaneous, (d) lock-in stimulated Raman spectra of glucose solutions with concentrations from 0-10 mM. Both sets of photon counter spectra are normalized to the highest point of the photon counter stimulated data, and both sets of lock-in spectra are similarly normalized to the highest point of the lock-in stimulated data. Differentiation between the glucose solutions of different concentration can be seen for all measurement techniques. The relative Raman intensity is generally higher for the stimulated spectra compared to the respective spontaneous spectra, but the enhancement factor between stimulated and spontaneous measurements is higher for the photon counter measurements overall. The photon counter stimulated spectra are significantly noisier than the other spectra. The stimulated lock-in spectra show slightly narrower spectral features than the corresponding spontaneous spectra, and Raman modes can be resolved to a slightly higher degree in the 424-575 cm^{-1} region.

Figure 6.6: 80
PLS model predicted glucose concentration with respect to actual concentration using the full spectrum of data from each of the four measurement methods: (a) Photon counter spontaneous (R^2 = 0.9995), (b) photon counter stimulated (R^2 = 0.987), (c) lock-in spontaneous (R^2 = 0.9998), (d) lock-in stimulated (R^2 = 0.9998). The greater the strength of the linear regression fit, the lower the mean squared error, and the stronger the predictive power of the PLS model.

Figure 6.7: 81
Mean squared error between predicted and actual glucose concentrations for each measurement method over three different spectral ranges. Lower mean squared error values indicate stronger predictive power of the model, so the PLS model based on lock-in stimulated data was consistently the strongest predictive model.

Abbreviations

AFM	-	Atomic Force Microscopy
CARS	-	Coherent anti-Stokes Raman Scattering
CIS	-	Crystal Ion Sliced
CMP	-	Chemical Mechanical Planarization
FSRS	-	Femtosecond Stimulated Raman Spectroscopy
LED	-	Light Emitting Diode
LNO	-	Lithium Niobate
MIR	-	Mid Infrared
NICU	-	Neurological Intensive Care Unit
NIR	-	Near Infrared
PLS	-	Partial Least Squares
PPLN	-	Periodically Poled Lithium Niobate
SEM	-	Scanning Electron Microscopy
SERS	-	Surface-Enhanced Raman Spectroscopy
SRG	-	Stimulated Raman Gain
SRL	-	Stimulated Raman Loss
SRS	-	Stimulated Raman Scattering
UPS	-	Uninterruptible Power Supply
UV	-	Ultraviolet

Acknowledgements

There are many individuals who have helped me along this challenging journey, so I would like to take the time to thank them here. First of all, I'd like to thank my first advisor, Professor Richard Osgood Jr., and my thesis advisor, Professor John Kymissis. Professor Osgood was a great role model for me during the first half of my PhD who showed me that a researcher could be hard working while also having fun. Professor Kymissis welcomed me into his group after Professor Osgood retired and helped me develop a whole new set of skills and plan for my future career. I'm very grateful to have had the opportunity to work with two excellent advisors. I'd also like to thank Professor Adler Perotte, the principal investigator on the whole blood spectroscopy project, who was a great mentor for me. Professor Perotte introduced me to the statistical models used in my research and was a patient test subject for several in vivo spectroscopic experiments.

I've been lucky to have the chance to work with many research mentors and collaborators in several different labs. In particular, I'd like to thank Hsu-Cheng (Stan) Huang, who was my research mentor for the first few years of my PhD. I'd also like to thank Jerry Dadap for his guidance on many different projects and Guillaume David for helping me with programming in python and with microcontrollers. I'd like to thank all the faculty and administrative staff who have answered my numerous questions, especially Svitlana Samoilina, Montse Fernandez-Pinkley, and Christina Rohm in the APAM department.

Outside of research, I enjoyed planning events with the Columbia OSA/SPIE joint chapter and working as a superuser in the Columbia Makerspace. I'd like to thank Xiang (Alex) Meng, Christine Chen, Nathan Abrams, Raj Singh-Moon, Yi Lin for helping bring the laser maze to Maker Faire and for being great friends. I'd also like to thank Mohamed (Mo) Haroun for being such an enthusiastic leader of the Makerspace. I was also fortunate to be a Teaching Assistant for several Barnard physics labs, and would like to that Dr. Stiliana Savin and Professor Timothy Halpin-Healy for helping me grow in curiosity as a physicist and teacher.

Finally, I'd like to thank my family for all the love and support throughout the years. Theresa, I've always enjoyed our phone conversations where we encourage

each other through whatever life throws as us. Thanks for being the one I can always talk to about anything. Harry, I'm glad you started working in New York around the same time as I started grad school so we could be roommates for the first couple of years. Thanks for always being interested in listening to my research. Mom and Dad, you've given me everything and taught me the most important lessons in life. Thanks for raising me to be the man I am today. M.J, you're the love of my life and know better than anyone how hard I've worked over the past several years. Thanks for being with me during my journey, taking care of me when things got tough, and always finding a way to make me laugh.

~ for M.J ~

Preface

The one thing that stands out about my PhD experience is that I worked in two different research groups on two separate topics resulting in a two part dissertation. I began my graduate research in Professor Osgood's Optical Devices and Science group working on periodically poled lithium niobate. About halfway through, I moved on to Professor Kymissis's group, aptly called, Columbia Laboratory for Unconventional Electronics, and worked on a new project on biomedical spectroscopy. Changing groups and research topics was a challenge, as I needed to become an expert in a new field in a short amount of time, and take ownership of an unfamiliar project. On the other hand, this change was a great learning experience that broadened my skills as a scientist and engineer. During the first project, I mastered the techniques for fabricating tiny and fragile optical devices, while in the second project, learned how to use python to build statistical models. In addition to the difference in topics and skill sets required, the two projects differed in where I fit in the overarching project timeline. The periodically poled lithium niobate project was a longstanding project in the group, so I built on the work of many students before me. In contrast, I joined the biomedical spectroscopy project as it was starting, so I hope that future students will build upon my first prototypes and experiments.

Upon further reflection, I've realized that there are several interesting parallels between my research in the two groups. On several occasions, I worked a similar topic, but on a different scale or in a different context for each project. For example, I learned to both fabricate optical devices in the cleanroom and assemble an optical system in the lab. I created domain patterns in photoresist with the laser writer on the order of microns and designed medical devices in acrylic with the laser cutter on the order of centimeters. I used a high-end Raman microscope to measure poled domains in lithium niobate and developed a custom stimulated Raman system to measure glucose solutions. There are also some overlapping themes. The most obvious common theme is Raman spectroscopy as Raman played a key role in both projects. A more abstract common theme is the idea of repeatability in a scientific experiment. In the first project, fabricating periodically poled lithium niobate required

many delicate and sensitive steps, and a small error at any point would result in inconsistent poled domain patterns. Making the device with highly repeatable procedures was one of the project's greatest challenges, but it was essential for achieving meaningful results. Developing a spectroscopic system that would measure repeatable spectra was similarly a great challenge in the second project, but building strong predictive statistical models required repeatable spectral measurements.

Overall, I'm grateful for the opportunity to work on two very different projects and learn a wide variety of things. Perhaps the most important lesson that I've learned during my time as a PhD student is that no matter know much you know there is always more to learn.

Part I

Domain Broadening in

Periodic Poling of Thinned Lithium Niobate

Chapter 1

Periodically Poled Lithium Niobate

1.1 Introduction

Ferroelectric poling of periodic domains, such as used in the periodic poling of lithium niobate (PPLN) [1], [2] and in other electro-optical devices, has become an essential technology for efficient control of guided-wave optical and infrared beams [3], [4]. Thus, this technique allows quasi-phase-matching in nonlinear materials with non-phase-matched material refractive indices and, hence, enhances the desired frequency conversion process. Two important issues in quasi-phase matching are the material quality and the dimensions of the patterned domain structure for progressively smaller poling dimensions. Understanding this issue is a particularly pressing problem for both nanodevice applications and more conventional integrated optical devices operating at short wavelengths in thin-film ferroelectric crystals, such as $LiNbO_3$ or $LiTaO_3$ [5]. For applications in discrete waveguide optical devices, frequency conversion that is designed to generate blue and near-UV radiation requires periods with resolution of <1 μm [1], [6], [7], [8]. Other devices, such as switchable Bragg filters [9], backward second harmonic generation devices [10], [11], [12] and parametric oscillators [13], have similarly demanding requirements on poling resolution and quality. Thus understanding the materials properties of poling has basic device physics motivation.

1.2 Fabrication

Our basic experimental approach was to examine the domain material and structure of periodically poled $LiNbO_3$ (LNO) for free-standing samples of different thickness, using various microscopies and micro Raman spectroscopy. Each sample was prepared using polishing, annealing, photolithography, poling, etching,

post-poling annealing, and imaging. Note that sample preparation was a major issue in this experiment since samples of less than ~75 μm were fragile in handling, and preparation of such deeply thinned samples is not discussed in the literature. Examples of the cross sections of these samples with thicknesses from 500 to 25 μm, obtained with SEM, are shown later in the Chapter 2 below. In each case, the initial sample was a 500-μm-thick, Z-cut congruent LNO wafer, diced into 5 × 5 mm coupons. The Z+ side of each sample was polished to the desired thickness using chemical mechanical planarization (CMP). Polishing was carried out using diamond polishing pads with successively smaller particle size down to 0.5 μm so as to minimize surface scratches or abnormalities. The sample thickness was verified and measured by imaging the cross section with optical microscopy. Deviations in thickness were maintained at 6% or lower for all samples and the sample thicknesses ranged from 500 to 25 μm. In order to relieve any internal strain in the crystal lattice that built up as a result of dicing and polishing, each sample was annealed at 600 °C for 10 hours. To reduce lithium-ion out-diffusion, which would increase the required poling field [14], each sample was positioned between two larger LNO wafers during the annealing process. The efficacy of this process was confirmed by using Raman spectroscopy to compare the lithium concentration at the surface of an annealed and unannealed sample and it was found that the concentrations were equal within experimental error.

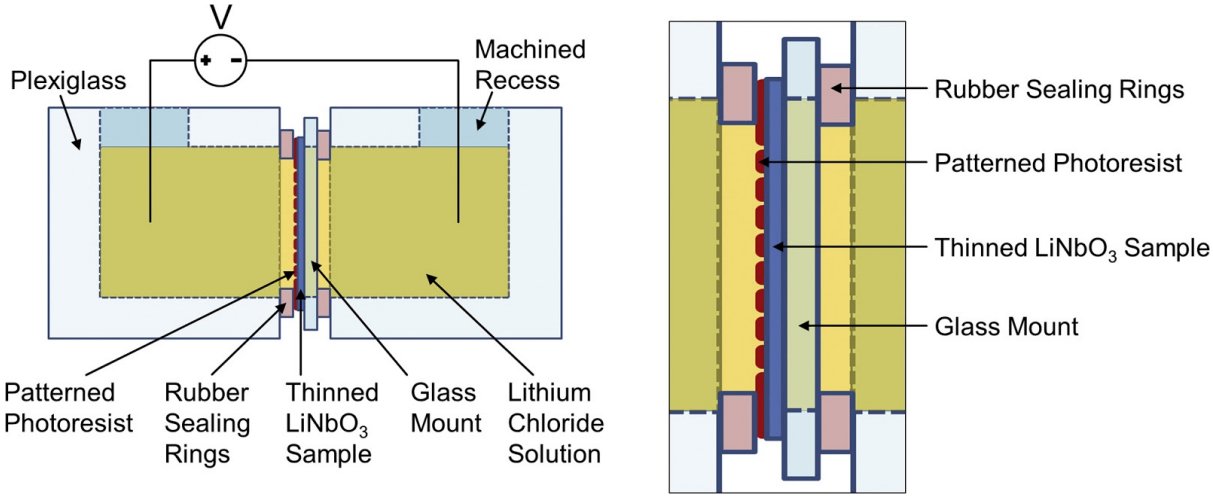

Figure 1.1: Schematic of the poling setup. The external voltage is applied across the crystal via a lithium chloride solution in contact with the bare regions (i.e., regions

where the resist is absent) of the surface. The materials used in the poling process are labeled in the figure.

Poling was carried out using an electrolyte solution in contact with the Z+ and Z- sides, with the poled pattern defined by a photoresist layer (Fig. 1.1). Such electrolytic poling has been described extensively in prior publications [5], [15], [16]. The positive photoresist layer was spun onto the Z+ side of the mounted samples for 30 seconds at 4000 RPM and then baked at 60 °C for 2 minutes. Lithographic patterning was done using laser writing (Heidelberg μPG 101 Laser Writer), so as to form a 1D periodic poling pattern into the photoresist over an area of 2 × 3 mm^2 on the samples. The poling period was 37.2 μm and the exposed vertical stripe width was 9.3 μm, resulting in a 25% duty cycle. These particular pattern dimensions are typical for nonlinear-optical second-harmonic conversion from a wavelength of 1550 nm to 775 nm by second-order quasi-phase matching. These exposed vertical stripes defined the location of the poling electrodes for the saturated lithium chloride electrolyte solution contacted the sample surface in these regions. Following photolithography, the samples were post-baked at 100 °C for 16 hours (an experimentally derived schedule which has been found, via Raman measurements, to relieve much of any handling-induced strain during fabrication and yet not disturb the poling period).

Each sample was mounted on a glass substrate with a 3-mm-diameter through-sample via; the use of this via-mounted substrate reduced the mechanical pressure on each sample and, thus, prevented breakage during the poling process. After mounting each sample, the electrolyte reservoir was filled with the electrolyte, with care taken to avoid bubbles or partially filled structures. Using the apparatus sketched in Figure 1.1, we applied a voltage waveform (Fig. 1.2) via the electrolyte to the bare regions of sample surface; in each case the peak voltage was incrementally increased until the waveform was sufficient to pole the sample.

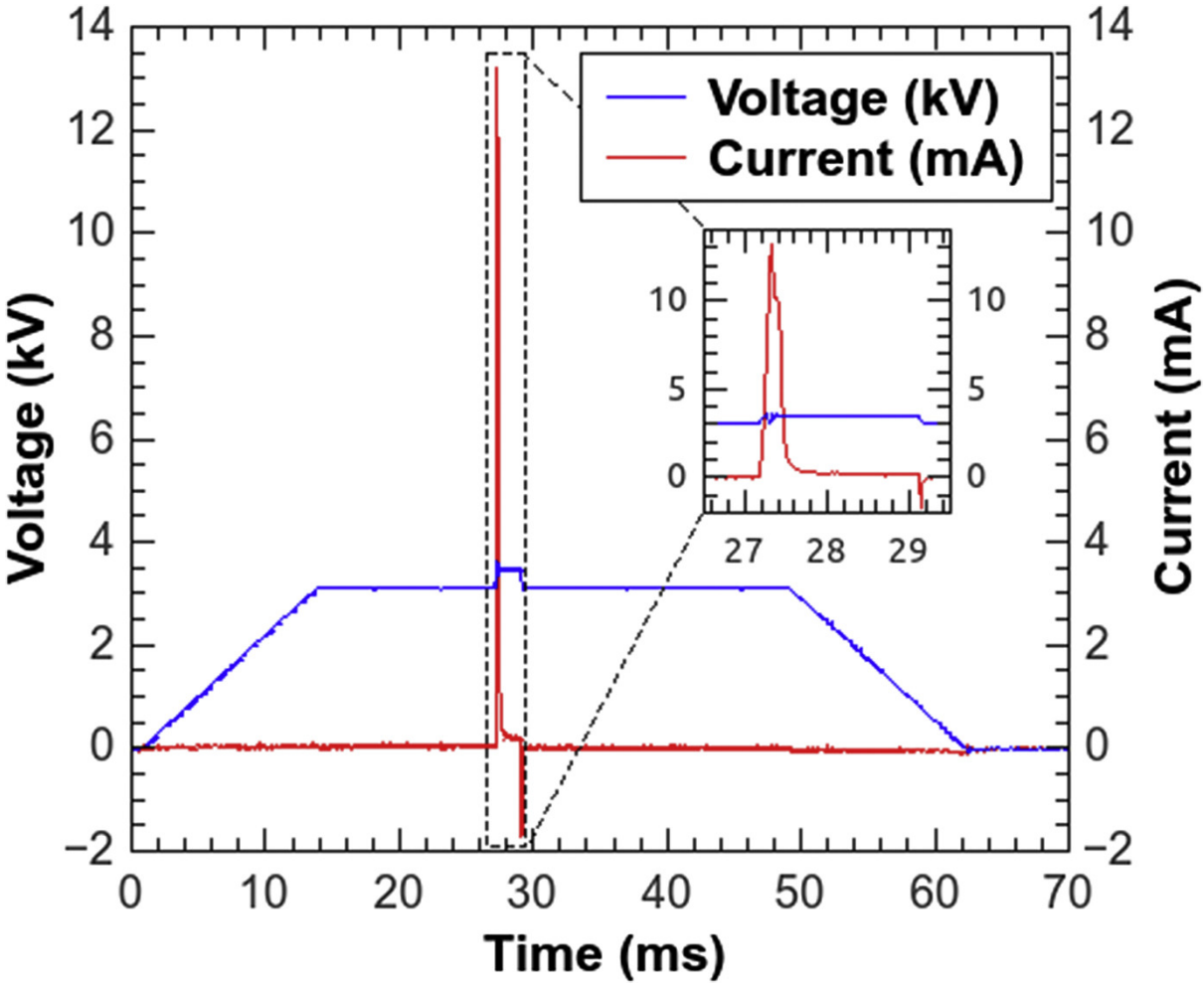

Figure 1.2: Plot of a typical poling waveform, i.e., voltage vs. time. When the voltage crosses a critical threshold value, a current spike is seen, indicating the onset of poling current. The inset shows an expanded waveform for both current and voltage.

It was possible to determine whether or not a particular waveform had poled the sample by monitoring the current through the poling circuit. A sharp spike in the current as the waveform reached the peak voltage indicated reversal of the ferroelectric domains; an expanded version of the waveform is shown in the inset of Figure 1.2. The negative current pulse, seen when the applied voltage decreases suddenly from the poling level, is due to the displacement current rather than back-poling. This feature reflects the rapid change in the applied voltage and has been observed in the earlier work cited above.

1.3 References

[1] G. A. Magel, M. M. Fejer, and R. L. Byer, “Quasi-phase-matched second-harmonic generation of blue light in periodically poled LiNbO3,” *Appl. Phys. Lett.*, vol. 56, no. 2, pp. 108–110, 1990.

[2] M. M. Fejer, G. A. Magel, D. H. Jundt, and R. L. Byer, “Quasi-phase-matched second harmonic generation: tuning and tolerances,” *IEEE J. Quantum Electron.*, vol. 28, no. 11, pp. 2631–2654, 1992.

[3] D. Djukic, R. Roth, J. Yardley, R. Osgood, S. Bakhru, and H. Bakhru, “Low-voltage planar-waveguide electrooptic prism scanner in Crystal-Ion-Sliced thin-film LiNbO3,” *Opt. Express*, vol. 12, no. 25, pp. 6159–6164, 2004.

[4] D. Djukic, G. Cerda-Pons, R. M. Roth, R. M. Osgood, S. Bakhru, and H. Bakhru, “Electro-optically tunable second-harmonic-generation gratings in ion-exfoliated thin films of periodically poled lithium niobate,” *Appl. Phys. Lett.*, vol. 90, no. 17, p. 171116, 2007.

[5] G. D. Miller, “Periodically poled lithium niobate: Modeling, fabrication, and nonlinear-optical performance”, Ph.D thesis, Stanford University, 1998.

[6] K. Mizuuchi, K. Yamamoto, and M. Kato, “Generation of ultraviolet light by frequency doubling of a red laser diode in a first-order periodically poled bulk LiTaO3,” *Appl. Phys. Lett.*, vol. 70, no. 10, pp. 1201–1203, 1997.

[7] T. Sugita, K. Mizuuchi, Y. Kitaoka, and K. Yamamoto, “Ultraviolet Light Generation in a Periodically Poled MgO:LiNbO3 Waveguide,” *Japanese J. Appl. Physics, Part 2 Lett.*, vol. 40, no. 3 B, pp. 1751–1753, 2001.

[8] P. A. Champert, S. V. Popov, J. R. Taylor, and J. P. Meyn, “Efficient second-harmonic generation at 384 nm in periodically poled lithium tantalate by use of a visible Yb–Er-seeded fiber source,” *Opt. Lett.*, vol. 25, no. 17, p. 1252, 2007.

[9] J. Son, Y. Yuen, S. S. Orlov, and L. Hesselink, “Sub-micron ferroelectric domain engineering in liquid phase epitaxy LiNbO3 by direct-write e-beam techniques,” *J. Cryst. Growth*, vol. 281, no. 2–4, pp. 492–500, 2005.

[10] A. Busacca *et al.*, “Nanopatterned ferroelectric crystals for parametric generation,” *2006 Int. Conf. Transparent Opt. Networks*, vol. 2, pp. 269–272, 2006.

[11] X. Gu, R. Y. Korotkov, Y. J. Ding, J. U. Kang, and J. B. Khurgin, “Backward second-harmonic generation in periodically poled lithium niobate,” *J. Opt. Soc. Am. B*, vol. 15, no. 5, p. 1561, 2008.

[12] L. Ming, C. B. E. Gawith, K. Gallo, M. V. O’Connor, G. D. Emmerson, and P. G. R. Smith, “High conversion efficiency single-pass second harmonic generation in a zinc-diffused periodically poled lithium niobate waveguide,” *Opt. Express*, vol. 13, no. 13, p. 4862, 2005.

[13] C. Canalias and V. Pasiskevicius, “Mirrorless Optical Parametric Oscillator,” *Nat. Photonics*, vol. 1, no. 8, pp. 459–462, 2007.

[14] V. Bermúdez, L. Huang, D. Hui, S. Field, and E. Diéguez, “Role of stoichiometric point defect in electric-field-poling lithium niobate,” *Appl. Phys. A Mater. Sci. Process.*, vol. 70, no. 5, pp. 591–594, 2000.

[15] J. Hirohashi, “Characterization of domain switching and optical damage properties in ferroelectrics”, PhD thesis,, Swedish Royal Institute of Technology, 2006.

[16] M. C. Wengler, M. Müller, E. Soergel, and K. Buse, “Poling dynamics of lithium niobate crystals,” *Appl. Phys. B Lasers Opt.*, vol. 76, no. 4, pp. 393–396, 2003.

Chapter 2

Domain Broadening in Thinned Lithium Niobate

The domain structure of poled deeply thinned lithium niobate is investigated as a function of sample thickness. Free-standing samples of thickness from 25 to 500 μm are prepared by a multiple-cycle polish and annealing procedure and then periodically poled. Using these samples and employing micro Raman scattering and scanning electron, atomic force, and optical microscopy together, the domain broadening and poling voltage are found to vary in a regular and significant manner. The poled domains show a reduction in width spreading of 38% as the sample thickness is reduced from 500 to 25 μm. Micro Raman probe measurements verify the quality and the uniformity of the poled domains and provide insight into their thickness-dependent poling contrast.

2.1 Introduction

Fabrication and design of domain-patterned devices require consideration of domain broadening, a phenomenon in which the reversed ferroelectric domains broaden beyond (or expand wider than) their intended dimensions during the poling process. Because of this difficulty, several materials-based domain-fabrication techniques have been proposed, and in some cases been demonstrated, to achieve small periods and domain structures, such as proton exchange [1], overpoling [2], backswitching [3], and ultraviolet light illumination [4]. Many of these approaches impact the materials properties of domains. Thus proton exchange requires selective alterations to the crystal structure, and overpoling and backswitching tend to produce domains of non-uniform width. As a result of the importance of poled crystals, there have been many studies of these material structures using electron and optical microscopies, proximal probes, and X-ray scattering; see, for example, [5], [6], [7]. These and other studies (cited below) have shown the importance of materials

factors such as poling voltage, strain, temperature, etc. in influencing the domain structure. However, it is interesting that there have been few if any reported systematic studies of the effects of sample thickness on the domain structure, despite the fact that it is generally believed to play an important role in domain structural properties [8], [9].

In this report, periodic-domain poling is performed with the domain widths that are typical for many standard periodically poled lithium niobate devices, i.e., 10s of μm, which are values appropriate for 2nd-order second harmonic generation. In our experiments, freestanding samples are carefully prepared using many cycles of polishing and annealing to have thicknesses ranging from 500 to 25 μm. Measurements are then made of the variation in critical external voltage necessary to pole the sample at each thickness. In addition, optical, electron, and proximal probe microscopy are then used to determine the variation in domain dimensions with thickness. A series of micro Raman measurements at specific $LiNbO_3$ Raman modes are employed to verify the sample properties and to uncover the spatial uniformity of the poled and unpoled domains at each thickness. Raman measurements are also made of the thickness-dependent contrast between the two domain orientations.

2.2 Visualization and Measuring of Domains

After poling, the photoresist pattern was removed using acetone and piranha solution; the sample was then etched with 49% hydrofluoric acid for ~10 min in order to allow visualization of the poled domains by either optical or scanning electron microscopy.

Material characterization, which was a crucial part of this experiment, was carried out using micro Raman spectroscopy and electron (SEM), optical, atomic force microscopy (AFM) imaging. Cross sectional SEM microscopy, so as to observe the depth dependence of the poled region, was carried out by cutting the sample with a diamond saw and then carefully polishing the sliced face, using the polishing procedure described above. The Raman instrumentation consisted of a focused beam, at a fixed excitation wavelength, so to enable an aerial image of the Raman

response to be obtained. The instrument was equipped with an image-processing computer system, which enabled manipulation of the Raman image by spectral content, intensity, etc. as needed. Note that the use of Raman spectroscopy and imaging in LNO has been carried out by several groups, including those examining the effects, such as strain, damage, and composition, from ion-implantation and other forms of materials processing [10], [11], [12], [13]; thus it was an essential materials probe for our experiments.

2.3 Poling Voltage

In order to examine the dimensional effects of ferroelectric poling, measurements were made of the external applied voltage, including the voltage needed to achieve poling, and the domain width as function of the sample thickness. The data showing the measurements of the voltage necessary for poling *vs*. thickness are shown in Figure 2.1. Thus it is seen that the measured plot of poling voltage *vs*. thickness displays a linear behavior with a significant non-zero Y-intercept, indicating a nonzero offset of the poling voltage *vs*. thickness. Our experiments are not focused on obtaining the more basic quantity of the coercive field, which has been used to obtain for example, the magnitude of the internal field [14] or the effects of numerous field reversals on this internal field [15]. Nonetheless it is of interest to note that the coercive field for thicker samples (obtained by a simple spatial average along Z obtained by dividing critical voltage with the sample thickness) is approximately constant and close to a typical value of 22 kV/mm [16], a behavior suggested in earlier publications [17].

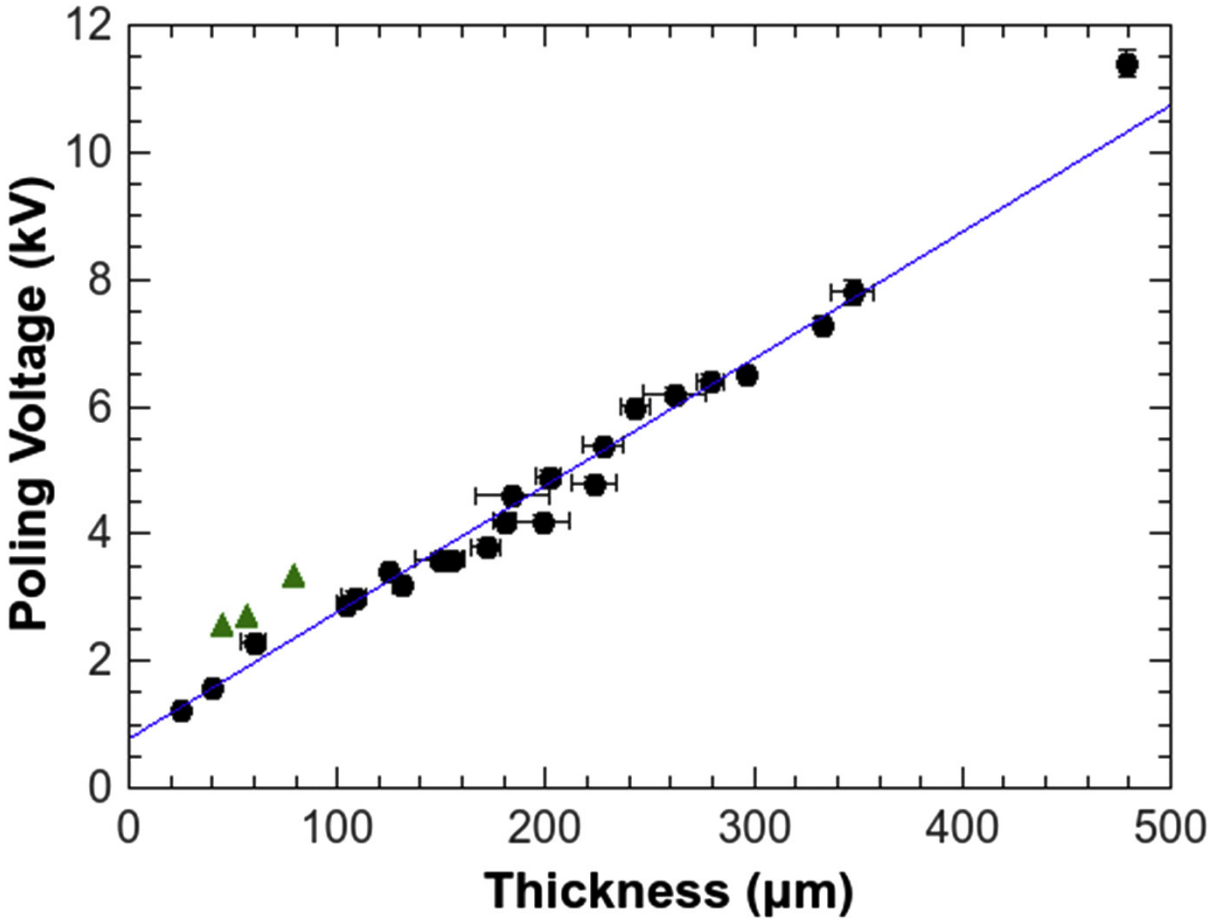

Figure 2.1: The measured poling voltage vs. sample thickness. Notice that the y-axis intercept does not intersect the origin. Thickness error bars are standard deviations from a set of multiple thickness measurements at different locations for each sample. The voltage error bars are determined from the poling voltage step size. The three green triangles towards the lower left corner of the graph correspond to samples from earlier experiments conducted with a less refined polishing technique. The error margin for these three data points was ±0.1 kV and less than ±5 μm. Error bars were removed for visual clarity.

An important observation of our results is the nonzero Y-intercept appearing in the plot of poling voltage *versus* sample thickness. This intercept can be a result of several phenomena. The most obvious one is the existence of an internal field, which is undoubtedly present as a result of defects or defect clusters [13], [18], which dominate the poling energetics for samples without voltage or other conditioning [19], [20]. In addition, our experiments have shown that the presence of surface defects

affects poling voltage significantly, especially for low sample thickness. In particular, these results were suggested by repeated observations in our laboratory that if samples were not properly annealed and polished, the Y-intercept of the poling voltage would increase in magnitude. An example of data from one of these experiments is shown by the green triangles in Figure 2.1. In addition, a related effect has also been clearly shown, for example, in recent experiments in our group using poling of small-area patterns with prior surface polishing defects such as scratches [21]. In those experiments surface scratches were found to correlate with a higher voltage required for poling.

2.4 Domain Broadening

In order to investigate the effect of sample thickness on domain broadening, the widths of the inverted ferroelectric domains were measured via optical microscopy for each sample and the average widths were determined by repeating this measurement across the stripes. The pattern in the photoresist, was found to be 9.3 μm for all samples, thus the domain width after pattern transfer *vs.* poling would be expected to be constant in the absence of any domain broadening. In fact, the data, as shown in Figure 2.2, shows that the domain width decreases with decreasing thickness as suggested, for example, in Ref. [22] and other early work. SEM cross-sectioning was also used to examine the domain broadening; examples of these measurements are shown in Figure 2.3. SEM measurements were also valuable in order to determine the same broadening behavior albeit from the perspective of an instrument with a different contrast mechanism. Further, the cross-section micrographs showed clearly that the domain broadening in a given sample was relatively uniform throughout the crystal depth, except for an induction area within ≤1 μm of the surface, and a possible slight narrowing towards the Z-side. In particular, the average difference in domain width from the Z+ to Z-side was measured to be within 1–2% for each sample, that is, the width of the features were constant within the resolution of the optical image. In addition, there appeared to be

no correlation between sample thickness and domain spreading throughout the depth of the crystal.

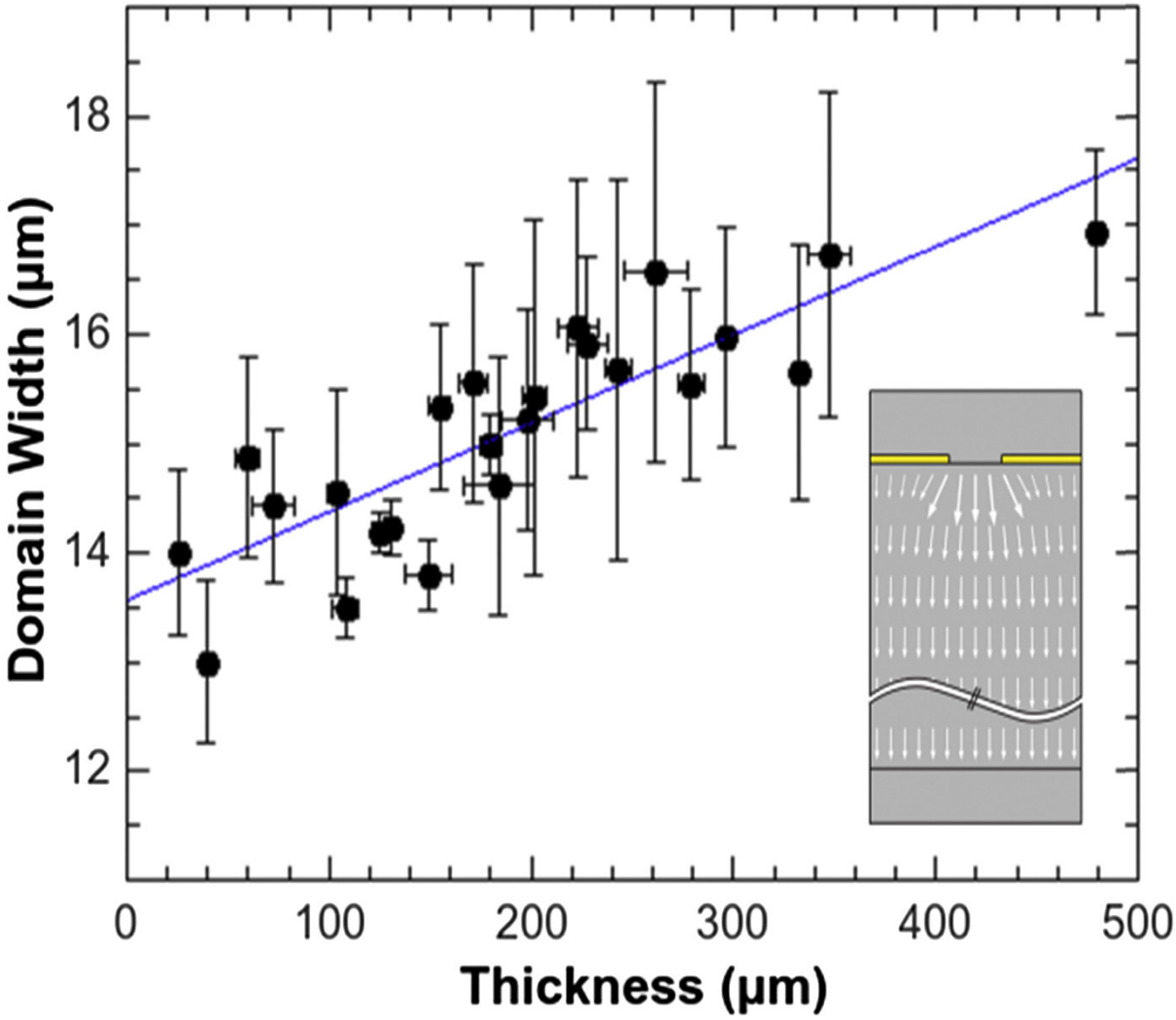

Figure 2.2: Domain width vs. thickness. Both the error bars for the domain width and thickness are standard deviations obtained from a set of multiple measurements, as explained in the caption of Figure 2.1. The inset shows the electric field plot obtained with a high-resolution finite element method Poisson computation for the field in the vicinity of the photoresist opening in the surface mask; the sample is 25 m m thick, and the opening is 9.3 m m in width.

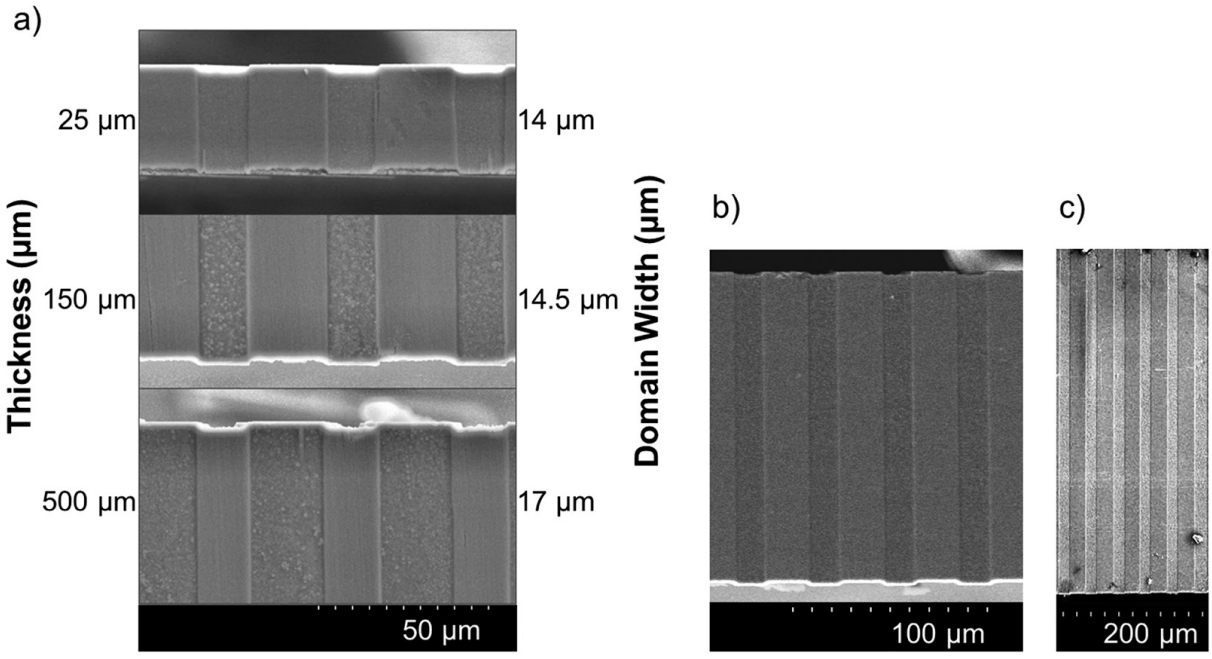

Figure 2.3: (a) SEM cross-section images of poled domains revealed by HF etching. For the 500-µm-thick sample, the domains are clearly wider than the domains in the 150 or 25-µm-thick sample domains. The etching between poled and non-poled domains appears different in this figure because the Y+ face is shown for the 25 and 150-µm samples while the Y- face is shown for the 500-µm sample. Panels (b) and (c) show zoomed out SEM images showing the full cross-section from Z+ to Z- sides with (b) 150-µm and (c) 500-µm-thick samples, respectively. The uniformity of domain width through the depth of the crystal is seen.

Returning now to the decrease shown in Figure 2.2, the overall domain width is well fit with a linear behavior, with a positive slope of the domain width/thickness ratio of 8 nm/µm. While this trend does show a linear relationship between thickness and domain width, the data gives a R_2 correlation coefficient of only 0.7, due to the scatter in the data. The error bars display the variance for each chip and show clearly the measured variability between chips. Note that several of the points are clear outliers since they are far off the measured plot. Clearly, there are additional stochastic factors that affect domain broadening – perhaps due to bubbles in the solution near the sample or the fact that near the onset of poling domain formation is highly nonlinear. Regarding the latter effect, the procedure, in which the voltage of the poling waveform is increased in discrete increments until poling, can lead to such

a stochastic behavior since the value of the off-set to the exact poling voltage could not be determined for each measurement. Thus, for example, in some cases, the sample may be somewhat over-poled by an unknown amount. In fact, as demonstrated in Ref. [16], such over-poling results in domain broadening.

The broadening of domains by electric-field poling in PPLN has been explored theoretically [23] by consideration of the local fringing electric fields and the compensation of charge. This theoretical model is based on a geometry that is very similar to the one used in our experiment. According to this model, in $LiNbO_3$ the domain broadening has been attributed to the very high transverse field near the top-surface edge of the photoresist/bare LNO interface. This field, which extends to a depth on the order of 1 μm in a 500 μm sample [24], causes charge to be injected under the photoresist/LNO interface, thus resulting in domain broadening. The calculation in Ref. [24] was based on the interface of a metal film directly on the oxide surface, thus we have used a model, which matches our materials interface more exactly, namely a polymer (dielectric A) and an electrolyte poling electrode (B). The lateral field is then calculated using a high-spatial-resolution finite element electric-field simulation (see Supplemental Materials Section for method and figure). Our calculation shows that as thickness increases the transverse fringing field magnitude increases; this result is thus consistent with observation that the width of the poled region expands as the thickness increases. This behavior is seen in the domain broadening increase seen in Figure 2.2. Note also that domain broadening will obviously be modified by defect pinning or compositional effects (such as in proton exchange LNO) [25], [26]. Alternately, in congruent LNO such as used here, a particularly important defect is a lithium deficiency [18].

2.5 Micro Raman Measurements

In the experiments above only the physical width of the poled sample and the poling waveform and voltage were measured. However in order to characterize the material properties of poled regions including orientation and spatial resolution, micro Raman spectroscopy was used; see the Supplemental Materials Section. In addition, Raman measurements were used to study any internal structural changes in the

lithium niobate domains induced by the poling, as well as the conditions of the samples following polishing. These measurements, which also included Raman-mode-specific imaging, were also used in examining thickness-dependent effects in poling. The effectiveness of Raman characterization of PPLN has been shown in previous studies [27], [28], [29]. See also an excellent review of this topic in Ref. [30]. Thus to summarize, the Raman spectroscopy measurements used here were essential to determine the quality and uniformity of the poled regions and to also examine several sample-thickness-related effects (see below).

Our choice as to which Raman crystal modes to use, was guided by the fact certain modes involve the motion of certain crystal-ion lithium species. These modes are particularly affected by poling as the lithium ions are displaced during the poling process. In addition, Raman spectroscopy was initially used in our experiments to determine the quality of the samples following polish thinning and in some cases other forms of processing, which strain the sample (see our comments elsewhere in this paper). In one of these cases, for example, it was observed that an application of coarse polishing led to the appearance of a normally forbidden mode, i.e., at 630 cm^{-1}. Only after careful finish polishing and annealing steps (see Section 2: Experimental) was this Raman mode eliminated and the samples used. Thus this result shows that one immediate application of the Raman probe in our work is as a simple probe of the state of the crystal and its near surface.

Figure 2.4 shows a series of linear 1D scans of the surface of the 150-μm sample. The figure is organized so as to display the signals recorded at wavelengths of specific transverse-optical (with the exception of the topmost spectral trace, which is longitudinal) Raman modes. Note that as described in an earlier study in Ref. [12], the domains can be readily detected or mapped by the dramatic changes in the Raman signal at the domain edges of the patterned stripes. In Figure 2.4, the spatial scale is overlaid with a microscope image as seen in the inset and it is apparent that the dimensions of the Raman signals correspond to the edges of poled regions. In addition, as discussed in Ref. [12], a comparison of the Z- and Z+ surfaces showed clearly the reverse symmetry of the edge signals. Our data show, generally, that the optical TE modes exhibit this characteristic asymmetric behavior for the Z+ and Z-

Raman signals, consistent with and attributed to the influence of surface internal fields transverse to the domain wall [12].

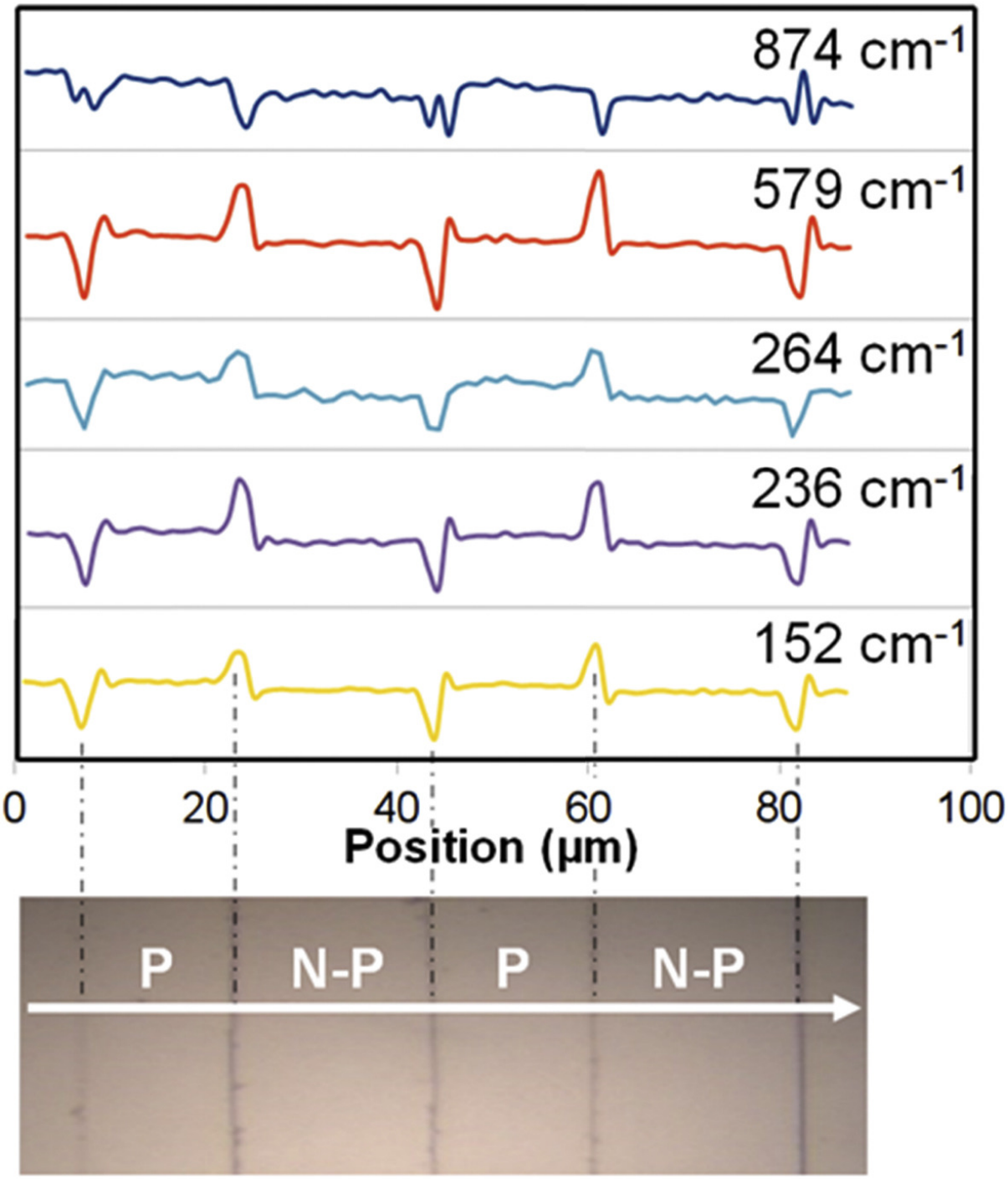

Figure 2.4: A Raman scan using 5 different Raman wavelengths along the top surface of a poled 150 μm sample with the scan direction perpendicular to the long axis of the poling stripe. This microscope image of the poled sample surface shows the path of the scan (horizontal line) and poled (P) and non-poled (N-P) regions.

In addition to simple linear scanning, it was also possible to image the poled regions via scanning over a 2-dimensional grid. Thus Figure 2.5 shows such 2D scans of two modes, i.e., at 236 and 264 cm^{-1}, over the same area of the surface. The images for these two modes show the same two vertically oriented domains, where the sharp edges of the domains are the vertical high contrast lines. Although the two modes show similar features along the domain edges, there are slight differences between the two modes. The 236 cm^{-1} mode, which is primarily a stretching mode between the Nb and O ions [31], has a weaker response in the poled region than does the 264 cm^{-1} mode. Thus it was possible to discern changes in the overall signal levels between the non-edge regions of the poled and non-poled domains regions in both Figure 2.4, Figure 2.5. For example, the 150-μm sample analyzed in Figure 2.4 had an average signal difference between the poled and non-poled regions of 2.3% for the 236 cm^{-1}mode and 2.9% for the 264 cm^{-1} mode.

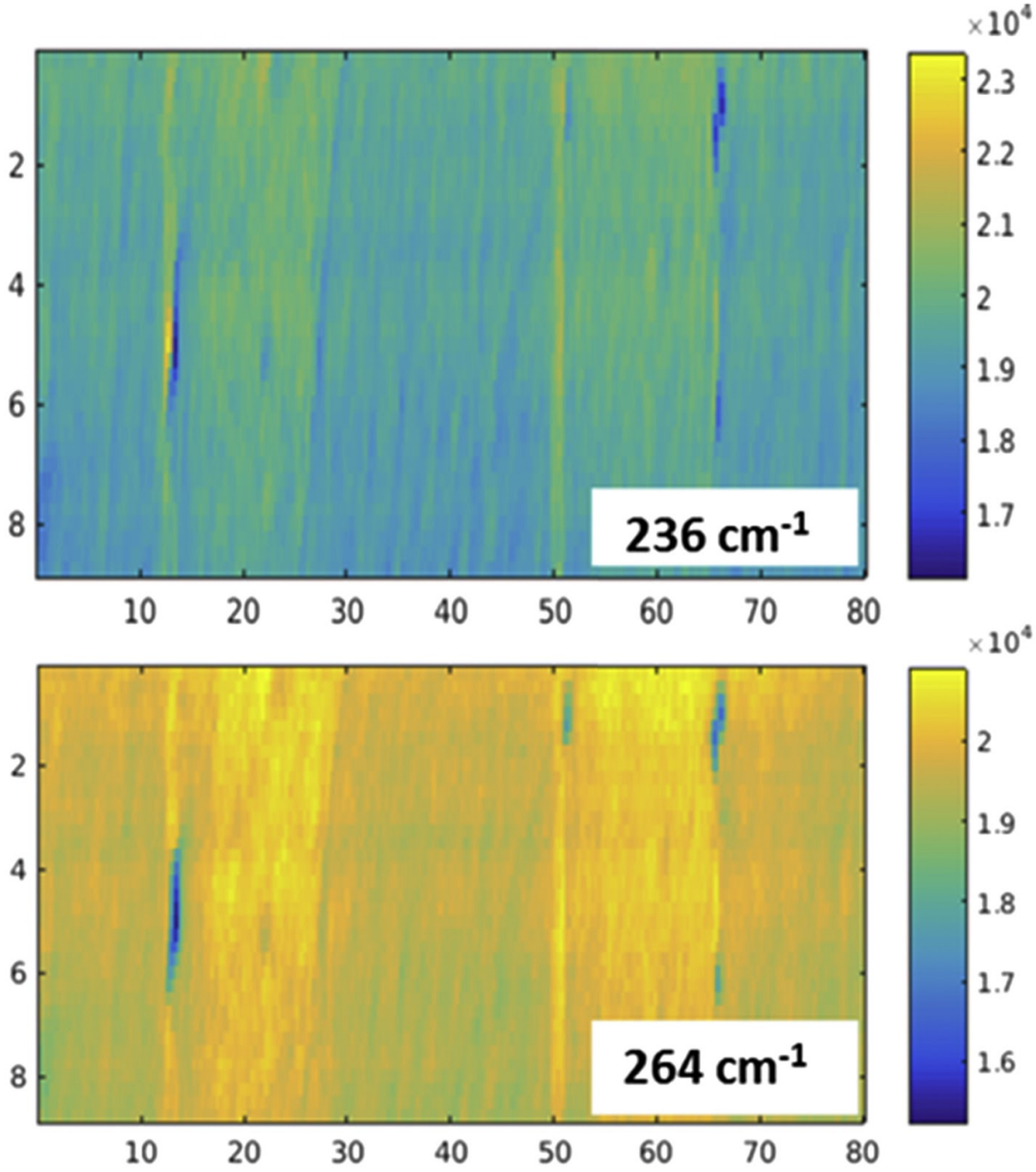

Figure 2.5: Raman images of a poled 150-μm-thick sample at the Raman modes shown in the white boxes. Spatial dimensions are in μm. Note the relative uniformity of the poled region.

Finally, Raman imaging was also used in a more direct way to examine the overall *quality* of the poled regions. Thus, Raman spectromicroscopy was used to find that uniformity in poling did not vary significantly with sample thickness. For example, measuring the Raman intensity of the 264 cm^{-1} mode across poled

samples 500, 150, and 100 μm thick, showed the variations to be 0.56%, 0.61%, and 0.70% in the poled region and 0.69%, 0.57%, and 0.84% in the non-poled region respectively. The other six modes measured here (152, 236, 331, 432, 579, and 874 cm^{-1}) had similar low values (all under 2%) of Raman intensity variation.

Note the presence of dark blue features on the side of the poled regions in Figure 2.5. These features were examined carefully using optical and then AFM images subsequent to a Raman scan. It was found that these features correlated to side edge imperfections in lithographic patterning, most likely due to imperfect beam scan overlap. In addition, measurements were also made of the Raman signal contrast between poled and unpoled regions as a function of sample thickness. Thus measurements were made of three representative sample thicknesses: 500, 150, and 100 μm, by averaging 50 locations on the poled and unpoled regions using an imaging (2-dimensional) scan. Our measurements showed that, for a probe of the 264 cm^{-1} mode, a 500-μm-thick sample had a poled/unpoled peak intensity difference of 1.9%, while a 150 μm sample had 2.9% difference, and a 100 μm sample had a 9.7% difference; similar values were seen for the probing the same three samples with the other six modes. In each case, the intensity difference between poled and unpoled regions increased with decreasing thickness. While this represents a relatively modest change in the poled to unpoled Raman intensity, it was persistent and real. One possible explanation for this effect is that there is a small amount of residual strain in the materials after poling and that this is most pronounced in the thinner samples, since it is known from several recent studies that in the presence of strain, the intensity of allowed Raman modes decreases [10]; note that this effect could be expected to mode dependent, although this dependence is at present unstudied. The small percentage change in the poled/unpoled ratio would make it difficult to detect this strain using a shift in the position of the Raman peak – a method also discussed in Ref. [20]. Finally to summarize this section, our Raman results show that the LNO properties of our poled samples are uniform, with possibly residual thickness-dependent strain.

2.6 Conclusion

The goal of this work was to examine thickness-dependent material effects in the poling of $LiNbO_3$ crystals. Our results show that the domain width increases as the sample thickness increases, a result consistent with the role of the increasing lateral field as the thickness increases. Our experiments also show that previously investigated Raman physics can be used as a reliable probing method to characterize the poled crystal. Our results show, for example, a high uniformity of the poled region of the crystal with well-defined edges even at smaller sample thicknesses as well as a thickness-dependent poling contrast. At present ion-slicing-based methods for poling much thinner samples are being developed and the effects examined here can be examined in these samples, which have micrometer or even submicrometer thicknesses.

2.7 References

[1] S. Grilli, C. Canalias, F. Laurell, P. Ferraro, and P. De Natale, “Control of lateral domain spreading in congruent lithium niobate by selective proton exchange,” *Appl. Phys. Lett.*, vol. 89, no. 3, pp. 18–21, 2006.

[2] A. C. Busacca, C. L. Sones, V. Apostolopoulos, R. W. Eason, and S. Mailis, “Surface domain engineering in congruent lithium niobate single crystals: A route to submicron periodic poling,” *Appl. Phys. Lett.*, vol. 81, no. 26, pp. 4946–4948, 2002.

[3] R. G. Batchko, V. Y. Shur, M. M. Fejer, and R. L. Byer, “Backswitch poling in lithium niobate for high-fidelity domain patterning and efficient blue light generation,” *Appl. Phys. Lett.*, vol. 75, no. 12, pp. 1673–1675, 1999.

[4] C. E. Valdivia *et al.*, “Nanoscale surface domain formation on the +z face of lithium niobate by pulsed ultraviolet laser illumination,” *Appl. Phys. Lett.*, vol. 86, no. 2, 2005.

[5] M. Manzo, F. Laurell, V. Pasiskevicius, and K. Gallo, “Electrostatic control of the domain switching dynamics in congruent LiNbO3 via periodic proton-exchange,” *Appl. Phys. Lett.*, vol. 98, no. 12, pp. 3–6, 2011.

[6] H.-C. Huang *et al.*, “Radiation damage by light- and heavy-ion bombardment of single-crystal LiNbO3,” *Opt. Mater. Express*, vol. 5, no. 5, pp. 1071–1088, 2015.

[7] H.-C. Huang *et al.*, “Characterization of selective etching and patterning by sequential light- and heavy-ion irradiation of LiNbO 3,” *Opt. Mater.*, vol. 46, pp. 1–5, 2015.

[8] M. Yamada and M. Saitoh, “Fabrication of a periodically poled laminar domain structure with a pitch of a few micrometers by applying an external electric field,” *J. Appl. Phys.*, vol. 84, no. 4, pp. 2199–2206, 1998.

[9] K. Mizuuchi, A. Morikawa, T. Sugita, and K. Yamamoto, “Generation of 360-nm ultraviolet light in first-order periodically poled bulk MgO:LiNbO_3,” *Opt. Lett.*, vol. 28, no. 11, p. 935, 2007.

[10] R. F. Schaufele and M. J. Weber, “Raman scattering by lithium niobate,” *Phys. Rev.*, vol. 152, no. 2, pp. 705–708, 1966.

[11] H.-C. Huang, J. I. Dadap, I. P. Herman, H. Bakhru, and R. M. Osgood, “Micro-Raman spectroscopic visualization of lattice vibrations and strain in He^+-implanted single-crystal LiNbO_3,” *Opt. Mater. Express*, vol. 4, no. 2, pp. 338–345, 2014.

[12] H.-C. Huang *et al.*, “A micro-Raman spectroscopic investigation of He+-irradiation damage in LiNbO3,” *Opt. Mater. Express*, vol. 3, no. 2, p. 126–142, 2013.

[13] S. M. Kostritskii and P. Moretti, “Micro-Raman study of defect structure and phonon spectrum of He-implanted LiNbO3 waveguides,” *Phys. Status Solidi C Conf.*, vol. 1, no. 11, pp. 3126–3129, 2004.

[14] V. Gopalan and M. C. Gupta, “Observation of internal field in LiTaO3 single crystals: Its origin and time-temperature dependence,” *Appl. Phys. Lett.*, vol. 888, no. December 1995, p. 888, 1995.

[15] V. Bermúdez, L. Huang, D. Hui, S. Field, and E. Diéguez, “Role of stoichiometric point defect in electric-field-poling lithium niobate,” *Appl. Phys. A Mater. Sci. Process.*, vol. 70, no. 5, pp. 591–594, 2000.

[16] A. Busacca *et al.*, “Nanopatterned ferroelectric crystals for parametric generation,” *2006 Int. Conf. Transparent Opt. Networks*, vol. 2, pp. 269–272, 2006.

[17] G. D. Miller, “Periodically poled lithium niobate: Modeling, fabrication, and nonlinear-optical performance”, Ph.D thesis, Stanford University, 1998.

[18] V. Gopalan, T. E. Mitchell, Y. Furukawa, and K. Kitamura, “The role of nonstoichiometry in 180° domain switching of LiNbO3 crystals,” *Appl. Phys. Lett.*, vol. 72, no. 16, pp. 1981–1983, 1998.

[19] T. Volk, M. Wöhlecke, *Lithium Niobate: Defects, Photorefraction and Ferroelectric Switching*. Springer Science and Business Media, vol. 115, 2008.

[20] S. Kim, V. Gopalan, and A. Gruverman, “Coercive fields in ferroelectrics: A case study in lithium niobate and lithium tantalate,” *Appl. Phys. Lett.*, vol. 80, no. 15, pp. 2740–2742, 2002.

[21] H.-C. Huang, “Investigation of Radiation Damage and Radiation Device Fabrication Techniques in LiNbO3”, Ph.D thesis, Columbia University, 2014.

[22] P. A. Champert, S. V. Popov, J. R. Taylor, and J. P. Meyn, “Efficient second-harmonic generation at 384 nm in periodically poled lithium tantalate by use of a visible Yb–Er-seeded fiber source,” *Opt. Lett.*, vol. 25, no. 17, p. 1252, 2007.

[23] G. Rosenman, K. Garb, A. Skliar, M. Oron, D. Eger, and M. Katz, “Domain broadening in quasi-phase-matched nonlinear optical devices,” *Appl. Phys. Lett.*, vol. 73, no. 7, pp. 865–867, 1998.

[24] M. C. Wengler, M. Müller, E. Soergel, and K. Buse, “Poling dynamics of lithium niobate crystals,” *Appl. Phys. B Lasers Opt.*, vol. 76, no. 4, pp. 393–396, 2003.

[25] C. Canalias and V. Pasiskevicius, “Mirrorless Optical Parametric Oscillator,” *Nat. Photonics*, vol. 1, no. 8, pp. 459–462, 2007.

[26] A. Tagantsev, E. L. Cross, J. Fousek, *Domains in Ferroic Crystals and Thin Films*. Springer, pp. 418-41937, (2010).

[27] R. Hammoum, M. D. Fontana, P. Bourson, and V. Y. Shur, “Characterization of PPLN-microstructures by means of Raman spectroscopy,” *Appl. Phys. A Mater. Sci. Process.*, vol. 91, no. 1, pp. 65–67, 2008.

[28] V. Bermúdez, D. Callejo, F. Caccavale, F. Segato, F. Agulló-Rueda, and E. Diéguez, “On the compositional nature of bulk doped periodic poled lithium niobate crystals,” *Solid State Commun.*, vol. 114, no. 10, pp. 555–559, 2000.

[29] Y. Kong *et al.*, “The asymmetry between the domain walls of periodically poled lithium niobate crystals,” *Opt. Mater. (Amst).*, vol. 27, no. 3, pp. 471–473, 2004.
[30] M. D. Fontana and P. Bourson, “Microstructure and defects probed by Raman spectroscopy in lithium niobate crystals and devices,” Appl. Phys. Rev., vol. 2, no. 4, 2015.
[31] Y. Repelin, E. Husson, F. Bennani, and C. Proust, “Raman spectroscopy of lithium niobate and lithium tantalate. Force field calculations,” *J. Phys. Chem. Solids*, vol. 60, no. 6, pp. 819–825, 1999.

Chapter 3

Poling in Crystal Ion Sliced Lithium Niobate

Crystal ion sliced lithium niobate thin films were fabricated using helium ion implantation, and ferroelectric poling was attempted on these thin film samples. Various fabrication techniques for preparing the 10-μm-thick samples for poling were tested, including chemical mechanical planarization of the ion-implanted layer and annealing. However, the poling attempts on the crystal ion sliced samples were unsuccessful, regardless of preparation procedures.

3.1 Introduction

Crystal Ion Slicing (CIS) is a technique for fabricating thin (order of microns and sub-micron) crystal substrates with similar crystallinity to their single-crystal bulk counterparts. For instance, crystal ion-sliced lithium niobate (CIS-LNO) retains the excellent electro-optical and nonlinear optical properties of the bulk crystal, while thin-film LNO formed by various deposition techniques does not [1]. Due to its optical properties and thinness, CIS-LNO is particularly suited for miniature optical devices and photonic integrated circuits. For example, electro-optically tunable photonic bandgap structures and micro ring resonators have been demonstrated in 600-nm-thick CIS-LNO [2,3].

Implementing CIS on ferroelectrically poled LNO enables additional applications for miniature optical devices. For example, previous researchers in the Osgood group at Columbia have fabricated 10-μm-thick second harmonic generation frequency conversion devices and electro-optic prism scanners by implementing CIS on ferroelectrically poled bulk LNO crystals [4,5]. However, reversing the order of the CIS and ferroelectric poling, in other words, implementing CIS first and then poling the thin ion-sliced crystal, has potential device advantages, but poses additional fabrication challenges. As described in chapter 2 of this work, broadening of the

poled ferroelectric domains decreases with decreasing thickness of the crystal, so poling thin LNO samples, including CIS-LNO, has the potential for higher resolution domain structures. In order to explore this idea, we fabricated 10-μm-thick CIS-LNO samples in collaboration with the Ion Beam Lab at the University of Albany. We attempted to pole the ion-sliced crystals using the traditional electrolyte solution method but were ultimately unsuccessful. Here we describe our attempts and consider alternative procedures in hopes of aiding future researchers.

3.2 Fabrication

Crystal Ion Slicing is accomplished by sending high energy ions into the surface of the crystal. The ions interact with the crystal lattice, lose energy, and are implanted within the crystal. The initial energy of the ions probabilistically determines the implantation depth. Ions energized to a specified level all have a high probability of stopping around the same depth, so a thin implantation layer is formed where the vast majority of ions are buried within the crystal lattice. We simulated the stopping depth of the ions using simulation software, The Stopping and Range of Ions in Matter (SRIM) [6] (Fig. 3.1).

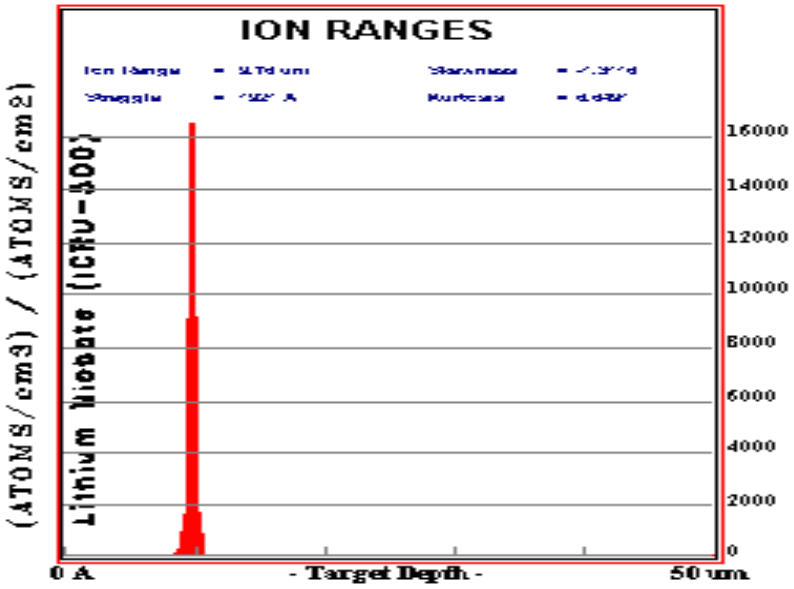

Figure 3.1: Implantation depth distribution from SRIM simulation showing the distribution in stopping depth of helium ions implanted in lithium niobate. The initial

energy of the ions was 3.6 MeV, and the average stopping depth was about 10 μm. The simulation shows that the ions are highly concentrated around the mean stopping distance, which results in a thin ion implanted layer.

In the case of fabricating CIS-LNO, helium ions are often chosen as the implanting species due to their low atomic mass, allowing them to be implanted relatively deep into the crystal. We implanted 500-μm-thick lithium niobate samples with helium ions at the Ion Beam Lab at the University of Albany (Fig. 3.2). The helium ions were energized to 3.6 MeV, directed into the Z+ surface, and formed an implantation layer depth in our crystals of about 10 μm. We used an experimentally optimized dosage of $5x10^{16}$ ions/cm^2 in order to create a sufficiently high concentration of helium ions for crystal ion slicing.

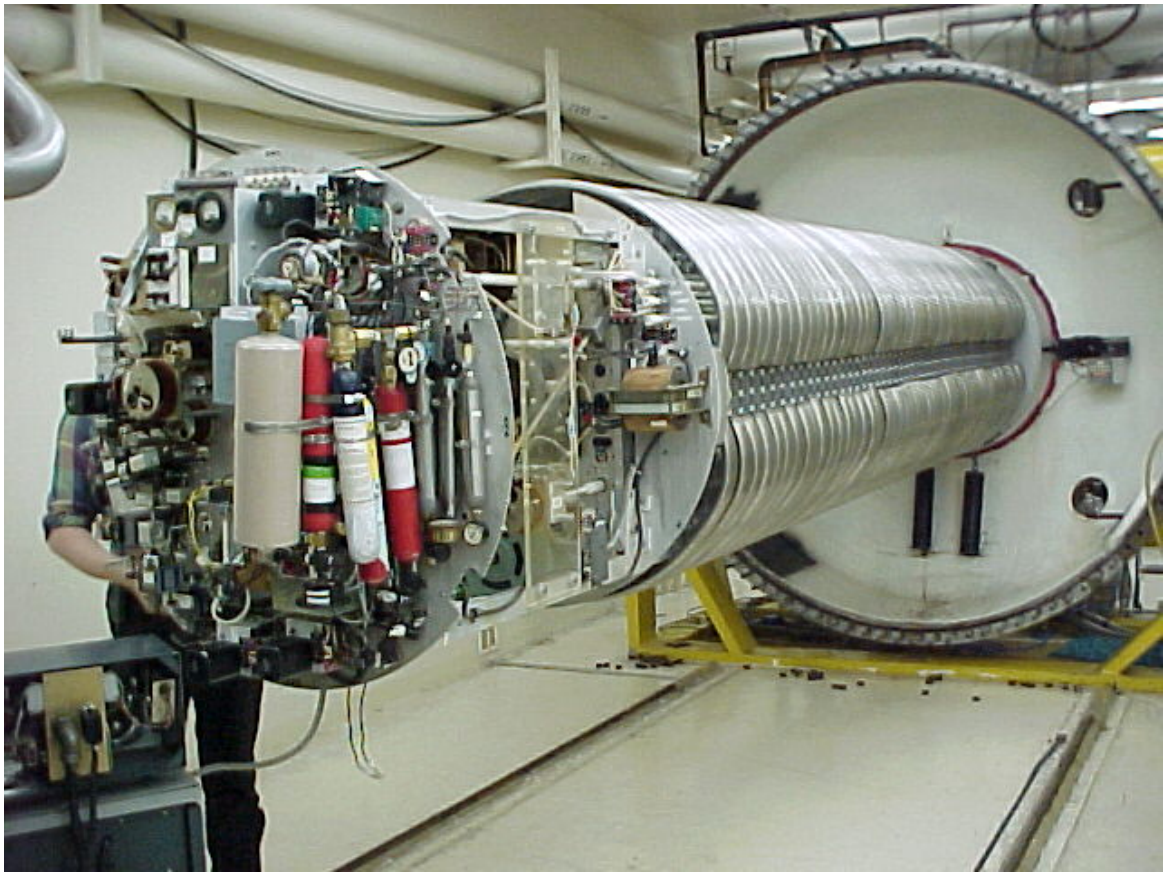

Figure 3.2: Ion beam at University of Albany. This Dynamitron has six installed beamlines, one of which is used for ion implantation. We sent 3.6 MeV helium ions at a dosage of $5x10^{16}$ ions/cm^2 into the Z+ surface of our lithium niobate samples.

After the ion implantation process was complete, the LNO samples were diced using a diamond saw into smaller rectangular samples of approximately 3.5x4 mm. We found larger samples were more likely to break during or after the etching process, so we limited the sample size as a practical measure. The diced samples were annealed at 250 °C for 2 hours. This annealing process formed micro-channels throughout the implanted layer. Then, the samples were submerged in a 5% hydrofluoric acid (HF) solution, and the implanted layer was etched by the HF. The HF solution seeped into the micro-channels formed during annealing process, allowing the implantation layer to be efficiently and uniformly etched. The samples were etched for 24 hours, by the end of which, a 10-μm-thick thin film layer, the CIS-LNO sample, completely detached from the parent bulk crystal. The CIS-LNO thin film was carefully removed from the HF solution using a custom plastic net structure. This is a particularly delicate process as the HF solution is hazardous to touch, and the CIS-LNO thin films is extremely fragile. Tweezers may be used to gently push the sample from the side but may not be used to pick up the sample because the applied force will inevitably break the thin film. The CIS-LNO samples were transferred from the net to either silicon or lithium niobate carrier wafers by careful nudging with tweezers or thin plastic sheets. Although the samples rested on top of the carrier wafers, they were not bonded, and could easily fly off if not handled with care. The etching process did not fully etch away the micro-channels formed during annealing, as they were still visible under microscope on the Z- surface of the CIS-LNO sample and Z+ surface of the parent bulk crystal (Fig. 3.3).

The HF etching process left the CIS-LNO samples slightly warped because the etching tended to begin from the outer edges and move inward. A second annealing process was necessary in order to flatten the samples out and relieve the strain in the material. For this annealing phase, the samples were heated to 600 °C in a tube furnace for six hours while sandwiched in between bulk LNO samples to prevent lithium ion outdiffusion.

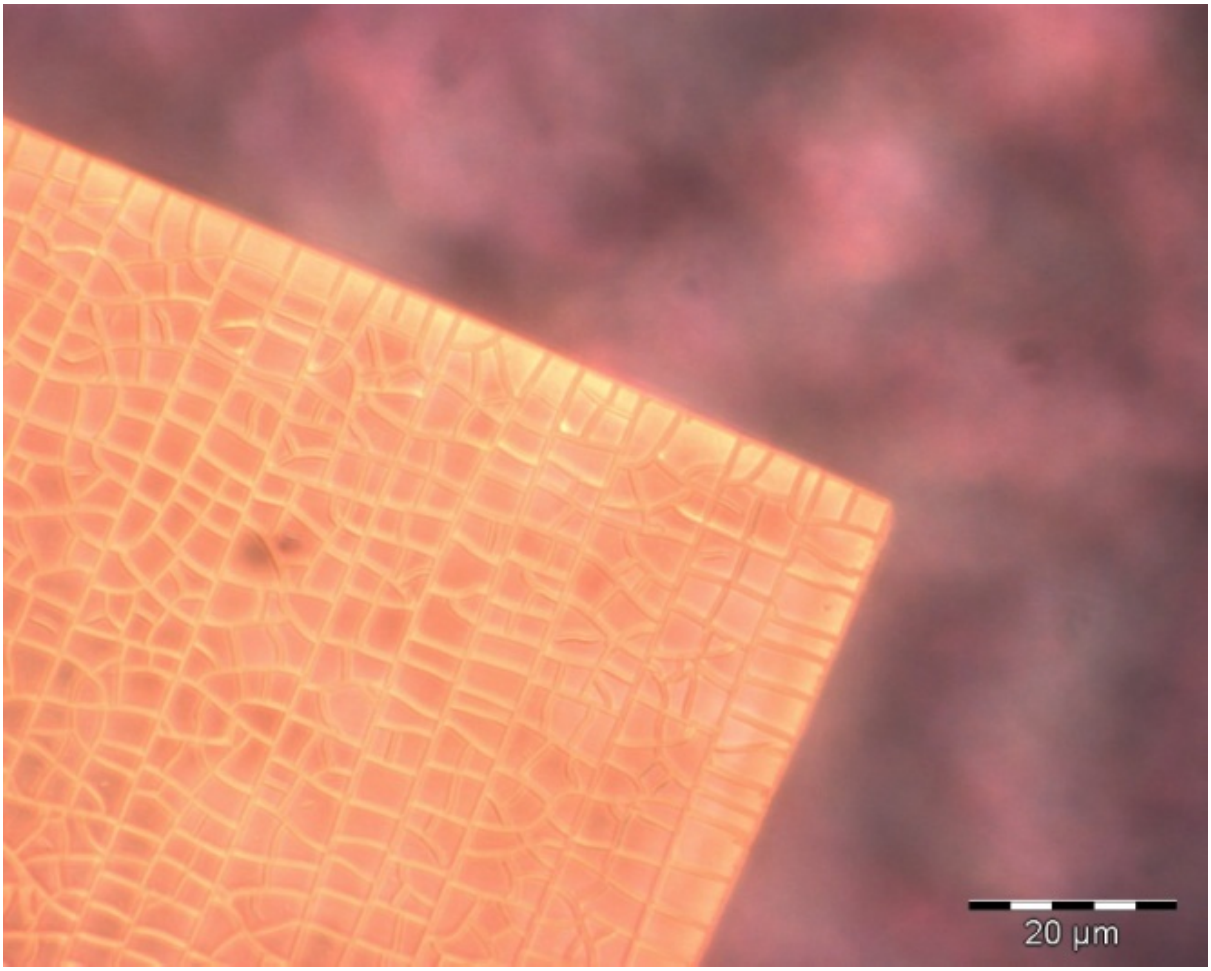

Figure 3.3: Optical micrograph of the Z- surface of a 10-µm-thick CIS-LNO thin film sample. The micro-channels of the implantation layer are visible on this annealed sample before undergoing the CMP polishing process.

3.3 Poling

Crystal Ion Slicing presents several challenges to poling the thin film lithium niobate samples. First, the CIS-LNO thin film samples are very delicate and easily broken. More importantly, the implanted layer is not fully etched away by the HF solution, as evidenced by the visible microchannels on the thin films (Fig. 3.3). This layer alters the crystal lattice structure and increases the coercive field required, making poling more challenging.

The remaining implanted layer may be removed by Chemical Mechanical Planarization (CMP). However, this polishing procedure is extremely delicate,

especially with the thin films, so samples are easily broken. Samples were bonded with acetone-soluble wax to the metal surface of a polishing mount, which controls the maximum polishing depth. The Z- surface with the micro-channels was polished using a lab wheel polisher with progressively finer diamond polishing abrasive pads. The final polishing phase used a colloidal silica-based slurry instead of pads to remove any micro-scratches sustained from the abrasive pads. The polishing was completed when there were no micro-channels or micro-scratches visible via microscope. The entire polishing process took about two hours per sample. The polished samples were removed from the metal polishing mount by dissolving the wax with acetone.

We divided our CIS-LNO thin film samples into three different sets of three samples each to study the effect of the fabrication procedures on poling. The first set of samples was unpolished and retained the remains of the micro-channels on the Z-surface, while the second and third sets were both polished with no visible micro-channels on the Z- surface. The difference between the second and third sets was that the samples in the third set underwent an additional annealing process after polishing to reduce strain obtained during polishing. The samples of the third set were annealed in a tube furnace at 600 °C, following the same procedures as the post-etching annealing process. All samples were mounted using wax on a glass substrate over its 3-mm-diameter through-substrate via, covered with an insulating photoresist layer, and patterned with a laser writer (Fig. 3.4).

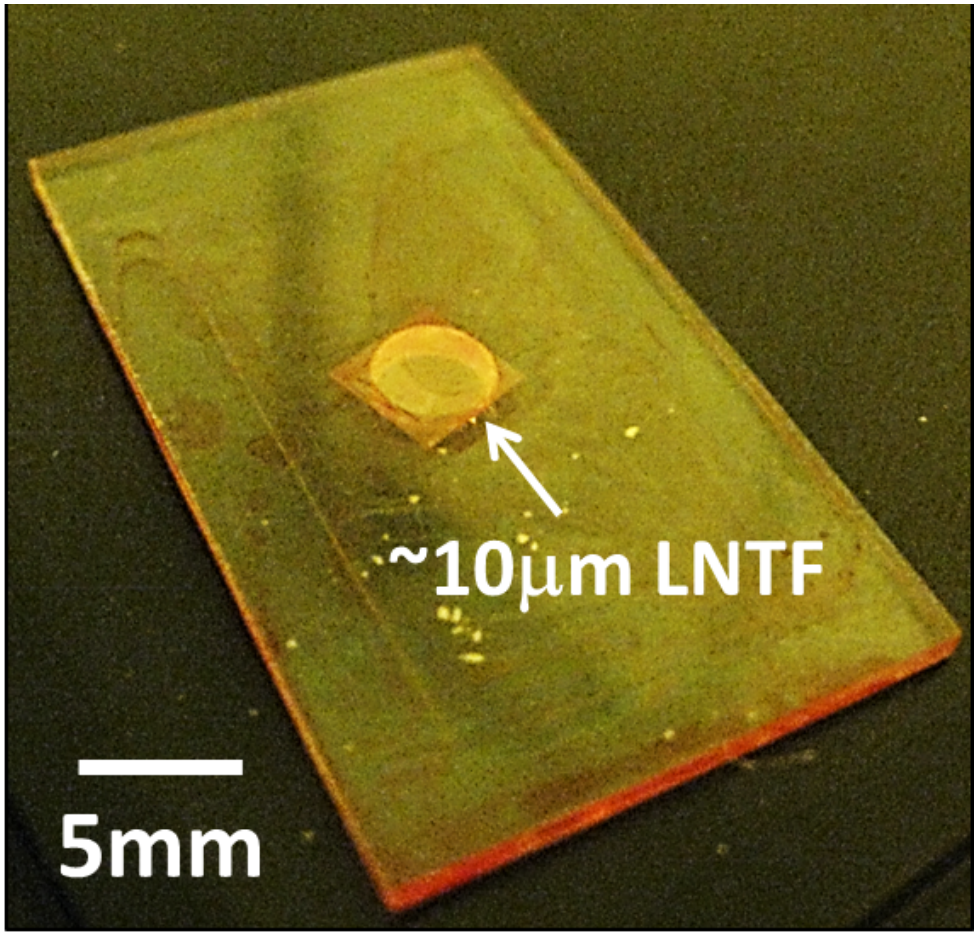

Figure 3.4: 10-µm-thick crystal-ion-sliced lithium niobate thin film (LNTF) sample wax-mounted on glass substrate over 3-mm-diameter through-substrate via. This particular sample has been polished to remove micro-channels from the Z- surface and annealed afterwards to relieve strain. A layer of patterned photoresist covers the sample and specifies the intended periodic poling pattern.

We attempted ferroelectric poling via the electrolyte solution method, as described in chapter 2 of this work, on the three sets of CIS-LNO samples, but we were unsuccessful in poling any of the samples in all three groups. Starting at 100 V, we incrementally raised the poling voltage by 10 V each attempt for each sample. Given the coercive field of lithium niobate of 22 kV/mm [7], we expected poling to occur at an applied voltage of about 220 V or slightly below for the slightly thinner polished samples. However, we continued increasing the poling voltage far above 220 V without the spike in current associated with poling occurring. This suggests

that a common factor, possibly related to the CIS process itself, was preventing samples in all three groups from being poled.

Upon reaching 500 V, we raised the poling voltage in progressively greater increments to find the point at which the applied electric field would cause the sample to break. Among all three sets, the samples eventually broke upon reaching a wide range of poling voltage values: from 2.65 kV to 13 kV. There was no clear correlation between the breaking voltage and sample set, indicating the breaking voltage was not strongly correlated to whether or not the samples were polished or annealed post-polishing. The wide range of breaking voltage values likely indicates that minor unmeasured variations from the fabrication process, such as strain in the crystal lattice or polishing depth, may have had a significant impact on breaking voltage.

3.4 Discussion

Our poling attempts on CIS-LNO were ultimately unsuccessful due to a variety of reasons, not least of which was the relatively low number of attempts. Fabricating CIS-LNO and preparing the samples for poling is a time-intensive and delicate process with numerous opportunities for breaking the samples or compromising the poling process in some way. The polishing process, in particular, poses the greatest challenge. Polishing is necessary to fully remove the ion-implanted layer which resists poling due to its altered crystal structure. However, our CMP process resulted in cracking and breaking many of the CIS-LNO samples, and likely induced strain into even the intact samples. Although the annealing process was conducted in order to reduce strain in the samples, it is possible that some residual strain remained, which may affect the poling process. Furthermore, in our experiments, we assumed that when the micro-channels associated with the ion-implanted layer were no longer visible via microscope, the ion-implanted layer would be fully removed. We did not verify this assumption by other means such as X-ray diffraction, so it is possible that some of the ion-implanted layer remained, even after the completion of our CMP process. The invisible remaining ion-implanted layer may have prevented poling from

occurring, even as we incrementally increased the poling voltage. Improved polishing procedures and adding post-polishing verification that the ion-implanted layer was fully removed may prove helpful in poling of CIS-LNO samples.

Although poling on CIS-LNO using the traditional electrolyte solution method is interesting from a materials science and fabrication perspective, other poling technologies may be more reliable while retaining the practical benefits of poling on CIS-LNO or thin LNO samples in general. For example, recent research has demonstrated poling by atomic force microscopy (AFM) methods on lithium niobate on insulator (LNOI) samples [8]. The LNOI samples consist of ion-sliced LNO films bonded to an insulator substrate and are far more robust compared to the free-standing CIS-LNO samples we studied in our experiments. Regardless of the specific method, ferroelectric poling of ion-sliced LNO provides an effective pathway towards frequency conversion in miniature optical devices and photonic integrated circuits.

3.5 References

[1] M. Levy *et al.*, “Fabrication of single-crystal lithium niobate films by crystal ion slicing,” *Appl. Phys. Lett.*, vol. 73, no. 16, pp. 2293–2295, 1998.

[2] F. Sulser, G. Poberaj, M. Koechlin, and P. Günter, “Photonic crystal structures in ion-sliced lithium niobate thin films,” *Opt. Express*, vol. 17, no. 22, p. 20291, 2009.

[3] G. Poberaj, M. Koechlin, F. Sulser, A. Guarino, J. Hajfler, and P. Günter, “Ion-sliced lithium niobate thin films for active photonic devices,” *Opt. Mater. (Amst).*, vol. 31, no. 7, pp. 1054–1058, 2009.

[4] A. M. Radojevic, A. Kumar, H. Bakhru, M. Levy, D. H. Jundt, and R. M. Osgood, “Second-order optical nonlinearity of 10-μm-thick periodically poled LiNbO_3 films,” *Opt. Lett.*, vol. 25, no. 14, p. 1034, 2000.

[5] D. Djukic, R. Roth, J. Yardley, R. Osgood, S. Bakhru, and H. Bakhru, “Low-voltage planar-waveguide electrooptic prism scanner in Crystal-Ion-Sliced thin-film LiNbO3,” *Opt. Express*, vol. 12, no. 25, pp. 6159–6164, 2004.

[6] J. F. Ziegler, *The Stopping and Range of Ions in Matter*, Elsevier, 2013.

[7] A. Busacca *et al.*, “Nanopatterned ferroelectric crystals for parametric generation,” *2006 Int. Conf. Transparent Opt. Networks*, vol. 2, pp. 269–272, 2006.

[8] T. Volk, R. Gainutdinov, and H. Zhang, “Domain Patterning in Ion-Sliced LiNbO3 Films by Atomic Force Microscopy,” *Crystals*, vol. 7, no. 5, p. 137, 2017.

Part II

Spectroscopic Methods for Whole Blood Analysis

Chapter 4

Apparatus for Portable In Vivo Blood Spectroscopic Analysis with Pressure Induced Time-Dependent Component

Non-invasive, in vivo, visible and near infrared spectroscopy hold great promise for blood metabolite concentration and clinical state estimation. An important step towards this goal is the challenge of identifying the spectrum of blood from the spectral mixture of blood and surrounding tissue. To address this challenge, we describe a computational model and measurement apparatus for portable visible and near infrared spectroscopy for in vivo blood analysis. We measured time-dependent transmission spectra of patients in a large metropolitan hospital neurological intensive care unit. Broadband visible and near infrared light sources illuminated blood vessels in the fifth fingertip of each patient transdermally, and the transmitted and scattered light was detected on the opposite side. Custom measurement clips attached to the fingertip of the patients were used to direct the illuminating light and collect the transmitted light. The measured spectra included a time-dependent increasing component induced by the pressure applied by the clip. A maximum likelihood model was developed to leverage this time-dependent component to extract spectra with features characteristic of whole blood from both the visible and near infrared signals. Keywords: spectroscopy, in vivo, blood, time-dependent

4.1 Introduction

Transdermal spectroscopic methods for non-invasive blood analysis have gained considerable attention in recent years due to the wide variety of biomedical applications these technologies may enable. A primary application of interest is non-invasive glucose monitoring for diabetics. In recent decades, the prevalence of diabetes has increased dramatically, and millions of diabetics worldwide take routine blood glucose level measurements using an invasive and painful finger prick method

[1,2]. Careful glucose monitoring is essential for diabetics to maintain acceptable blood glucose concentration levels for preventing various kidney, vascular, ocular, and neurological complications. A non-invasive method would be less painful, more convenient, and would likely improve compliance [3]. A variety of non-invasive technologies for glucose monitoring have been developed, including electrical impedance measurements that send a current through the skin, electromagnetic sensing using a pair of coupled inductors, ultrasound, glucose-bonding hydrogels in contact lenses, fluid harvesting through laser-induced microholes in the skin, and a wide variety of optical spectroscopic methods [4,5,6]. Spectroscopic methods have gained considerable attention as they are generally the least invasive, even among other non-invasive technologies.

Spectroscopic analysis of blood has many additional useful applications beyond glucose monitoring. Spectroscopic monitoring of hemoglobin levels and oxygenation states has been shown to assist in the diagnosis of sepsis and predict septic shock [7,8]. Monitoring of other forms of hemoglobin, such as carboxyhemoglobin and methemoglobin, can be used to diagnose carbon monoxide exposure and methemoglobinemia respectively [9,10]. Blood tests for levels of a wide variety of metabolites including bilirubin, albumin, urea, glucose, cholesterol, and triglyceride are all used to aid in diagnosis of a similarly wide variety of health conditions related to many organ systems including the liver, kidneys, heart, and brain [11].

However, current gold standard blood analysis lab tests are time and resource-intensive processes generally involving multiple processing techniques including centrifugation, flow cytometry, chromatography, mass spectrometry, electrochemistry, fluorescence, and spectroscopy [12]. The cost of blood analysis for patients in hospital intensive care units is especially high as blood tests are part of routine patient care [13]. A non-invasive spectroscopic monitoring method could supplement the gold standard blood tests and significantly reduce cost and complexity of clinical blood analysis, particularly for intensive care units.

Recent research has demonstrated the feasibility of measuring many blood constituents via spectroscopic methods on whole blood both in vitro and in vivo. Visible spectroscopy in particular is effective for measuring both oxygenated and

deoxygenated hemoglobin and blood oxygen saturation levels in vivo [14]. This is due to the fact that oxygenated and deoxygenated hemoglobin have distinct absorbance peaks in the visible wavelength range [15]. However, due to relatively high absorption of visible light in human skin, particularly below 600 nm [16,17], many of the spectroscopic applications in the visible range are limited to analysis of skin and tissue apart from blood [18,19]. Nevertheless, both light sources and detectors in the visible range are generally inexpensive, stable, and efficient, which makes identifying the relatively weak spectral signal of blood more feasible and somewhat compensates for the high absorbance of skin.

In addition to the hemoglobin peaks in the visible range, whole blood also has distinct spectroscopic features in the near infrared (NIR). The main advantage of NIR spectroscopy for in vivo applications is the low absorption of NIR light in skin [15,16], making the spectrum of blood easier to detect. Blood metabolites, such as glucose, also have spectral features in the NIR range, which have been used to measure the concentration of blood glucose both in vitro and in vivo [20,21]. Spectral measurements of properties of blood apart from metabolite concentrations, such as cerebral blood flow, have also been demonstrated to be effective in the NIR range [22, 23]. Although the light sources and detectors in the NIR are generally more expensive, less sensitive, and less efficient than their visible counterparts, low absorbance in skin tissue makes NIR spectroscopy a powerful technology for non-invasive blood analysis in vivo.

Much of the previous work has been performed in a lab setting, which mitigates some of the challenges of a clinical setting. A lab setting allows for easier control of measurement conditions, which is greatly advantageous for making consistent and robust measurements. In this report, we present our design and implementation of a simple non-invasive spectroscopy system for transdermal blood analysis specifically designed for a clinical setting. Our system is capable of measuring both visible and NIR transmission spectra with a separate light source and spectrometer for each method. Custom clips are attached to the fifth fingertip, and transmission measurements are taken through the finger. The primary challenge for in vivo blood measurements is to separate the spectrum of blood from that of all surrounding tissue, and we accomplished this by measuring and analyzing changes

in the spectrum over time using a probabilistic model. In this report, we analyze a particular subset of our measurements, for which the time-dependent component of the spectrum increased gradually. This time-dependent component of the spectrum likely corresponds to the spectrum of blood, and has similar spectral features as whole blood spectra as previously reported in the literature. The spectral measurements are initiated by simple custom software with a streamlined user interface designed to run on a laptop computer.

4.2 Portable Spectroscopy System

Our non-invasive transdermal blood spectroscopy system is designed for taking time-dependent spectral measurements on patients in the Columbia University Medical Center Neurological Intensive Care Unit (NICU). The entire system resides on a portable cart for convenient transport and is powered by uninterruptible power supply (UPS) (Fig. 4.1). The visible and NIR spectroscopy systems each have their own separate spectrometers, light sources, optical fibers, and clips. The visible light source is a high-brightness LED (Cree Warm 3000K) and is part of the visible system clip while the NIR light source is a Tungsten Halogen lamp (Ocean Optics HL-2000) which uses a liquid light guide (Newport 77634) to direct the light from the lamp to the clip. Both light sources require 10-20 minutes to stabilize in intensity, therefore the UPS allows the system to be moved between rooms without cycling the power, which would require additional time for stabilization.

(a) (b)

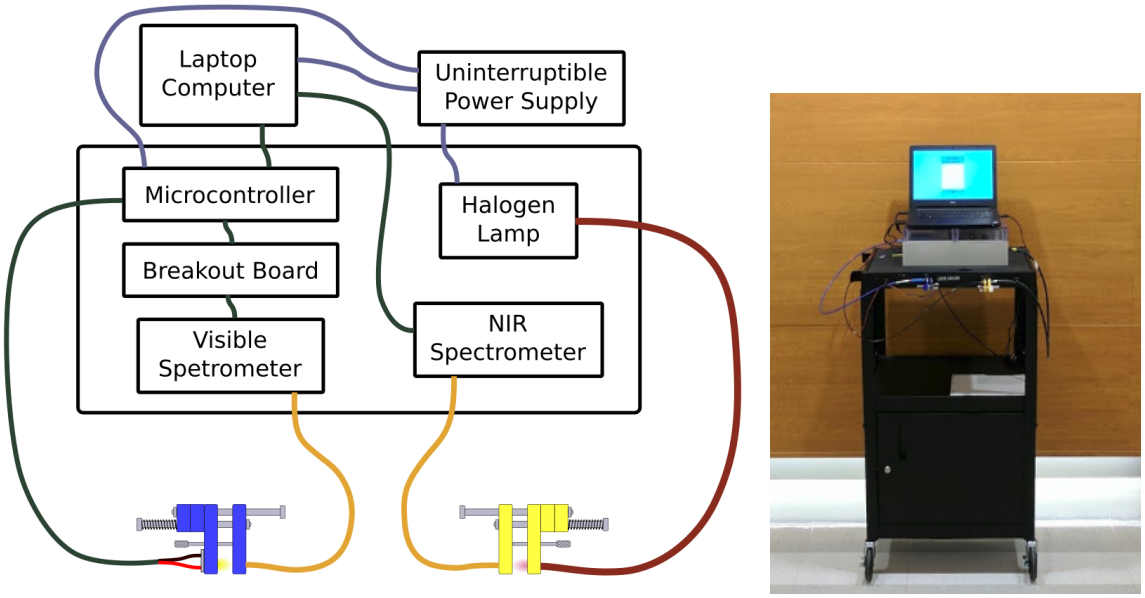

Figure 4.1: (a) Spectroscopy system setup diagram. The spectrometers, microcontroller and associated circuitry, and halogen lamp are all enclosed in a plastic container for protection and efficient disinfecting. (b) Spectroscopy system on portable cart for convenient transport between patients. The laptop computer rests on the plastic container, and the UPS is enclosed in the lower compartment of the cart.

Both spectroscopy systems use low-OH fused silica optical fibers to collect the transmitted light and direct it to their respective spectrometers. The optical fibers and light guide are each 1 meter long and semi-flexible, which aids in positioning the cart within reach of the patient.

The two spectrometers and Tungsten Halogen lamp are enclosed and secured in a plastic container on the cart. This helps prevent these devices from being moved, accessed, or adjusted during transport in any way that might affect the measurements. More importantly, the plastic container can be cleaned and disinfected easily and efficiently, while cleaning individual devices would be more time consuming and error prone. Due to taking measurements in the NICU setting, efficient and effective cleaning of all equipment prevents transmission of infection and is of paramount importance. System components outside of the container are also designed for easy cleaning. For example, the clips, which attach to the patients'

fifth finger, must be thoroughly cleaned after each use using disinfectant wipes. To facilitate easy cleaning, the clips are made out of laser-cut acrylic and metal, both of which are non-porous materials which can be easily disinfected in accordance with NICU safety procedures.

4.3 Measurement Procedure

The clips are designed to attach comfortably and securely to the patient's fifth fingertip. Although other parts of the body, such as the tongue, are advantageous for measuring transmission blood spectra [24], the fingertip is more comfortable for patients and more convenient. The clips consisted of two thin laser-cut slabs of acrylic with the light source (LED or liquid light guide from Tungsten Halogen lamp) on one side and the collecting optical fiber on the other (Fig. 4.2). To take a measurement of transmission spectra, the tip of the fifth finger is placed between the two acrylic slabs. The acrylic slabs are joined together by three bolts acting as vertical shafts, which allow the two acrylic slabs to slide linearly. Preliminary experiments showed that consistent alignment between the light source and collecting fiber was important for repeatable spectral measurements. Therefore, the design required linear movement guided by the vertical shafts because rotational movement guided by a hinge would lead to misalignment due to variation in finger size of the individual. The two slabs are pressed together by two compression springs around two of the vertical shafts for a gentle but secure fit on the finger. An adjustable thumb screw determined the minimum closed space between acrylic slabs and prevented the clip from closing too tightly on the fingertip. The clips are secured to the cart with magnetic hooks when not in use.

(a) (b)

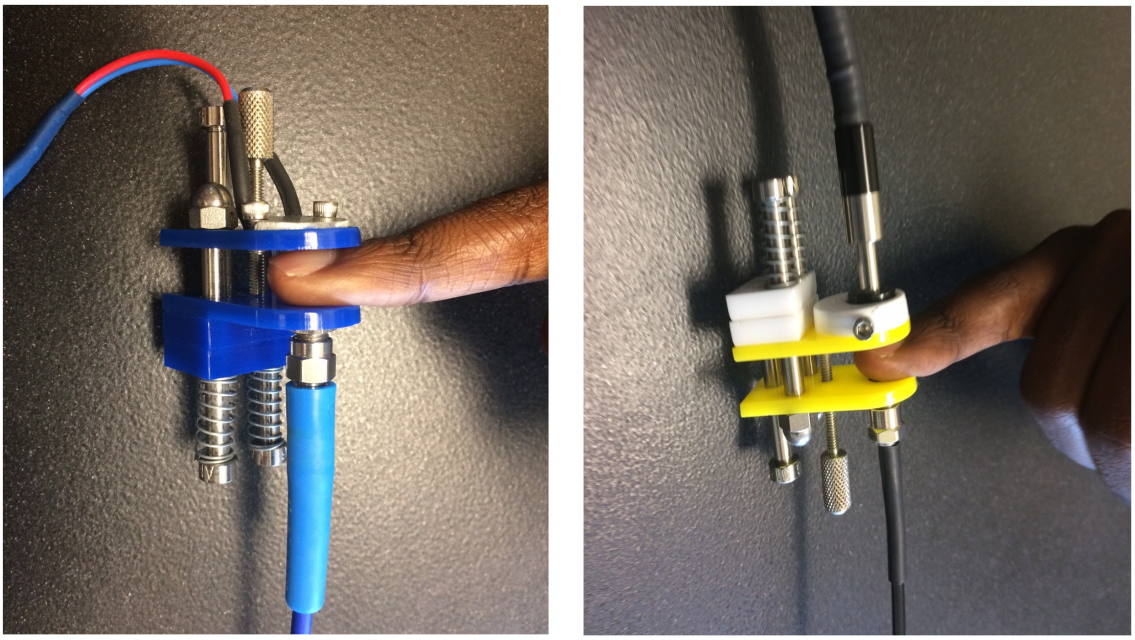

Figure 4.2: Clip design for (a) visible and (b) NIR spectral measurements. The visible design includes the LED light source on the clip itself while the halogen lamp, which acts as the NIR light source, is positioned on the cart, and the light is directed to the clip via liquid light guide.

Both the visible and NIR spectrometers detect the transmitted light via optical fiber. The visible spectrometer (Hamamatsu Mini-spectrometer C12880MA) has a spectral range of 340-850 nm, and weighs only 5 g. It is connected to a microcontroller (STM32 Nucleo), which communicates with the laptop computer via the python library, pyserial. The NIR spectrometer (Ocean Optics Flame-NIR) has a spectral range of 900-1700 nm, and weighs 265 g. It is directly connected to the laptop computer via USB, communicating via the python library, python-seabreeze. Both spectrometers, particularly the Mini-spectrometer, are small and portable, making them easy to work with in a clinical environment.

As the primary task of the NICU staff is to take care of the patients, the spectroscopy system and clips must not impede their workflow in any way. The streamlined user interface of the spectroscopy system is designed to require minimal input from the NICU staff. After attaching the clip to the patient's finger and adjusting the spacing to the correct size with the thumb screw, the spectral measurements

begin with the push of a single button. The integration time is automatically adjusted before measurements are recorded to optimize detected signal while avoiding saturation. Spectra are measured for a total of 60 seconds with the frequency of measurement determined by the integration time. This process is repeated for each clip and spectrometer pair. Dark spectra are taken beforehand with a thin aluminum plank in the clip blocking the optical path.

4.4 Computational Methods

We identified the component of the measured spectra corresponding to blood by analyzing the time-dependent component of the measured spectra. The spectra were modeled as the sum of a time-invariant baseline and a time-dependent component. For both our visible and NIR measurements, the L2-norm of the time-dependent component was less than 5% of that of the time-invariant baseline (Fig. 4.3). The relatively small, but significant time-dependent component of the spectrum was caused by the pressure of the clip on the finger slowly forcing blood away from the fingertip. This decreased the effective path length of blood, while the effective path length of all the surrounding tissue remained relatively constant.

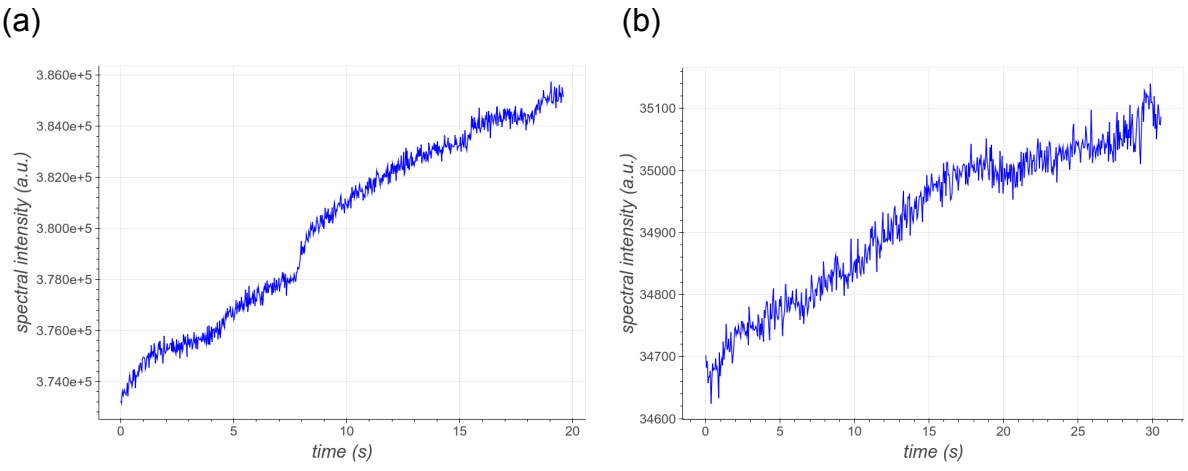

Figure 4.3: L2-norm of (a) visible and (b) NIR spectra over time. Both spectra increase gradually with time due to the decreasing effective path length of blood. The rate of increase in spectral intensity ranges from about 0.1-0.2% per second for the visible spectrum and 0.03-0.07% per second for the NIR spectrum.

We modeled the time-dependent change in effective path length of blood using an iterative Beer-Lambert-based model. The Beer-Lambert law, which formulates the attenuation of light propagating through a medium, is given by equations (1) and (2),

$$T = \frac{I_z}{I_0} = e^{-\tau} \tag{1}$$

$$\tau = \int_0^l \sum_{i=0}^{N} \mu_i(z)\, dz \tag{2}$$

where T is the transmittance, z is the depth in the medium, l is the total path length of the medium, and μ is the attenuation coefficient. For the purposes of our iterative model, we make some simplifying assumptions. We assume that the attenuation coefficient of blood, μ_{bl}, is constant, and the total effective path length through blood is $l_{bl}(t)$. This reformulated expression is given by equation (3),

$$\tau = \mu_{bl} l_{bl}(t) + \int_0^l \sum_{i=0}^{M} \mu_i(z)\, dz \tag{3}$$

where the first term corresponds to the time-dependent component of the spectra associated with blood and the second term corresponds to the time-invariant component of the spectra associated with all other tissue in the optical path. Modeling τ as a Student-t distributed random variable with wavelength-specific scale completed the model which was estimated using the method of maximum likelihood. Using a stochastic gradient ascent procedure based on the Adam algorithm [25], we identified the time-dependent component of each measured spectrum and modeled them as absorption spectra.

4.5 Results

The model-generated absorption spectra in the visible (Fig. 4.4) and NIR (Fig. 4.5) wavelength ranges both show similar spectral features corresponding to blood

spectra reported in the literature. The visible spectrum shows a group of spectral peaks corresponding to hemoglobin at 528 and 568 nm [15]. The measured transmittance at these values is relatively low compared to the transmittance between 600 and 700 nm where absorption in the skin is lower, indicating that the model is isolating time-dependent components of the spectrum corresponding blood rather than intensity drift in the light source. Due to the limited bandwidth of our visible light source, the model is not able to identify any time-dependent component with precision in the low light level regions of the transmission spectrum below about 500 nm and above 750 nm. Therefore, these regions of the absorption spectra show a high level of noise.

(a)

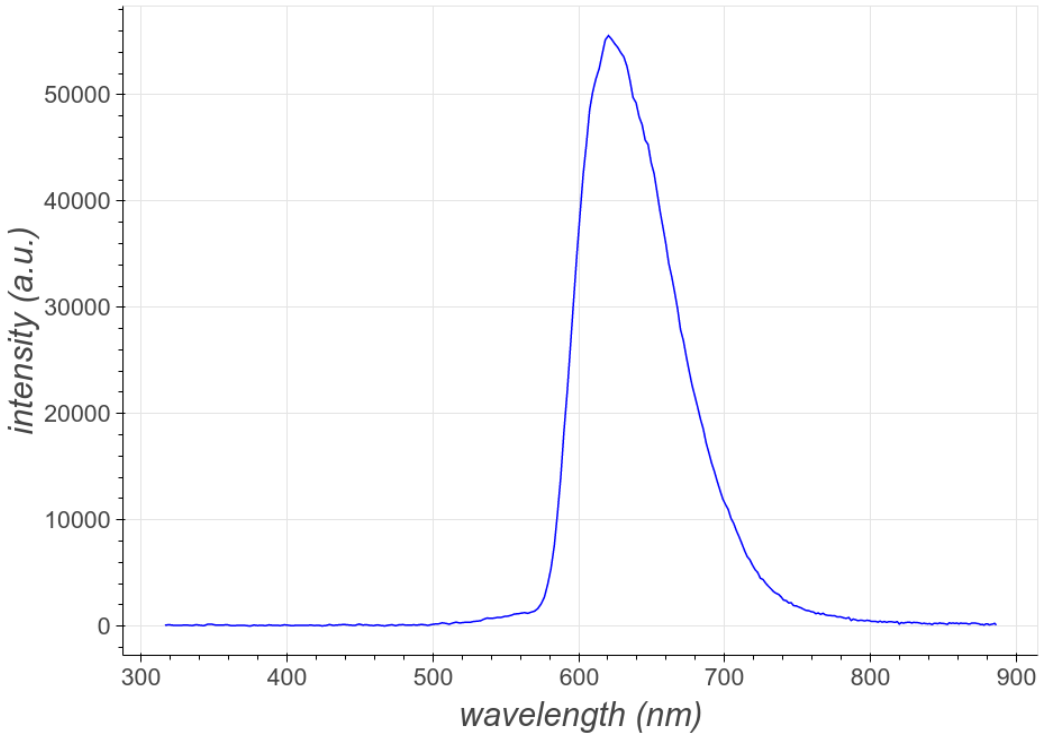

(b)

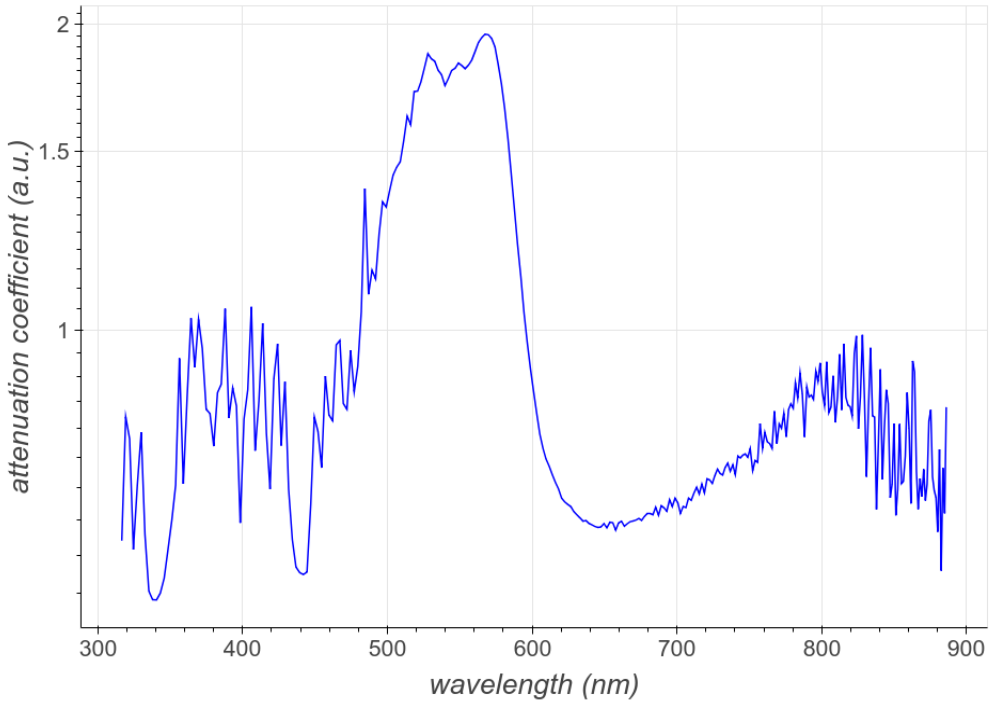

Figure 4.4: (a) Measured visible transmission spectrum (at t=0). (b) Absorption spectrum of blood extracted from time-dependent component of the visible measurement. The spectral peaks at 528 and 568 nm correspond to absorption peaks of hemoglobin. Although the total measured signal is low at these peaks, the time-dependent character was modeled. The regions of high noise on the sides of the blood spectrum correspond to regions of the spectrum outside the bandwidth of the light source.

(a)

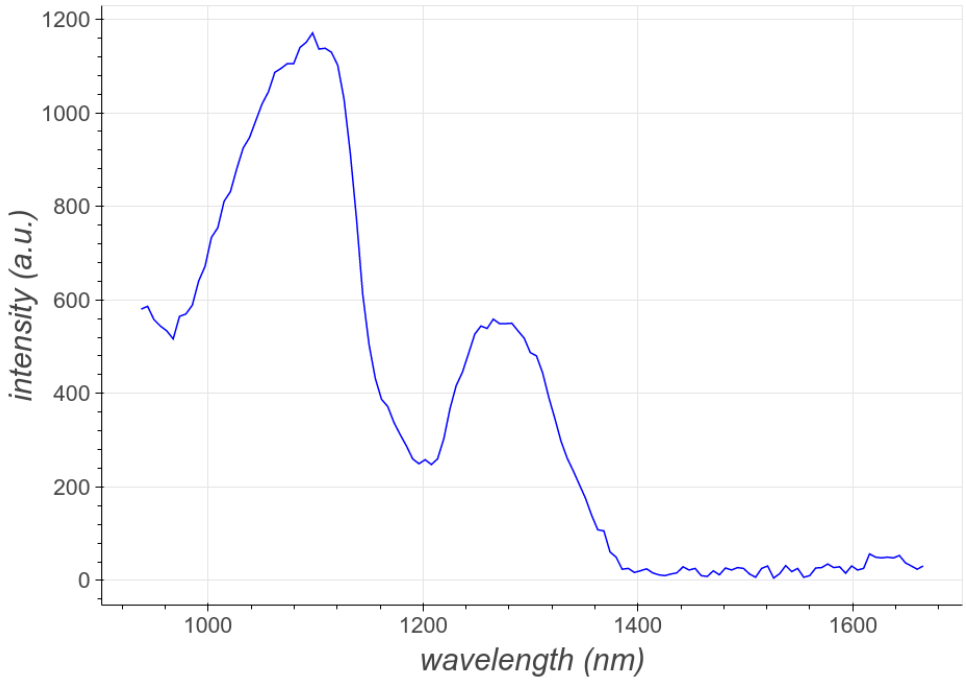

(b)

Figure 4.5: (a) Measured NIR transmission spectrum. (b) Absorption spectrum of blood extracted from time-dependent component of the NIR measurement. In contrast to the visible spectra, due to less absorption by skin and other surrounding

tissue, the NIR absorption spectrum of blood is similar to the inverse of the measured transmission spectrum.

The model-generated NIR absorption spectrum of blood (Fig. 4.5) shows a small spectral peak around 1200 nm and then a gradual positive slope between 1300 and 1400 nm. These spectral features correspond to a combination of oxygenated hemoglobin, deoxygenated hemoglobin, and water [15]. Since skin has low absorbance in the NIR, the absorption spectrum of blood and measured transmission spectrum show similar features (in their respective absorption or transmittance space), indicating blood is a major component of the measured spectrum.

4.6 Discussion

Our method overcomes a significant challenge of in vivo spectroscopic blood analysis in providing reliable way to isolate the spectral component of blood from that of the surrounding tissue in both the visible and NIR ranges. The compression clip induces a decrease in the effective optical path length of blood over time which results in a slow increase in the measured transmission spectra. This time-dependent component is identified by the iterative Beer-Lambert-based model, which models the measured spectra as the sum of a time-independent and time-dependent component. The absorption spectra of the time-dependent component show similar spectral features as spectra of whole blood reported in the literature, which supports our assertion that these absorption spectra correspond predominantly to blood with minimal interference from extraneous tissue. Furthermore, we collected our measurements using a simple transmission spectroscopy system in a hospital NICU, showing that our method may be implemented in a cost-effective manner for a clinical environment.

Further research must be carried out in order to apply our method of isolating the spectrum of blood to monitoring devices for blood glucose, hemoglobin, and other metabolites. In order for these monitoring devices to be successful, they must be able to measure small variations in the blood spectra associated with the

metabolite levels of interest with high accuracy and consistency. Some specific improvements to our measurement system may aid in reaching the necessary measurement resolution. Using broader spectrum light sources for illumination would allow a larger portion of the spectrum to be modeled. For example, due to the limited bandwidth of the visible LED, the modeled visible spectrum of blood was extremely noisy above 750 nm and below 500 nm. The modeled NIR spectrum of blood was similarly noisy above 1400 nm due to the limited bandwidth of the halogen lamp. The compression clip could be improved by controlling the compression distance systematically with motorized actuators and a force sensor feedback system. This would allow for more direct control of the rate of change in effective path length of blood in the fingertip, which would likely improve the accuracy and consistency of the model-generated spectra. Furthermore, the rate of change could be optimized for accuracy and potentially increased to reduce measurement time. Other measurement geometries could be explored beyond our transmission geometry. For example, a backscattering probe in conjunction with the compression clip may prove advantageous due to shorter total path length of light backscattered from blood directly below the surface of the skin.

A key assumption of our method for isolating the spectra of blood from that of surrounding tissue is that the time-dependent component of the measured spectra is due to the change in effective optical path length of blood. Our results support this assumption because the model-generated blood spectra do indeed have similar peaks and characteristics as whole blood spectra reported in the literature, but we do not prove this assumption from first principles in this report. Although it is likely that the total change in effective optical path length is a good approximation of the change in effective optical path length of blood only, the surrounding tissue is likely a factor as well. Further research may quantify the dependence on change in path length of blood in comparison to that of surrounding tissue for the time-dependent component of spectra measured with a compression clip. Both physical simulations and in vivo experiments could be conducted to determine the limits of our path length assumption in regards to time or compression distance. An additional limitation of our computational model is that it only identifies the time dependent component up to a model-determined scaling constant. This is due to the fact that the model cannot

identify the relative magnitudes of the path length and molar extinction coefficient, only their combined magnitude.

This spectroscopic method of identifying blood spectra in vivo has significant potential for portable applications. A wide range of environments, including hospital, military, and home, would greatly benefit from efficient and portable in vivo methods for measuring blood spectra. Our current measurement setup was carried on a cart, which was brought from room to room by the NICU staff for measurements on multiple patients in quick succession, so the system is already portable to an extent. The spectrometers, arguably the most critical components of the system, are relatively small, with the visible Mini-spectrometer weighing only 5 g and the Flame-NIR weighing 265 g. As miniaturization of spectrometers continues to be developed, smaller spectrometers could enable ultra-portable spectroscopy systems, which would be beneficial for routine or long-term blood monitoring devices.

4.7 Human Subjects

Participants were recruited from the patient population of the NICU. Patients were excluded from consideration if they were on contact isolation due to the risk of nosocomial infection and increased sterilization requirements. The results presented in this report are from a representative patient from this cohort. This study was reviewed and approved by the Columbia University Medical Center Institutional Review Board (IRB).

4.8 References

[1] C. E. Ferrante do Amaral and B. Wolf, “Current development in non-invasive glucose monitoring,” *Med. Eng. Phys.*, vol. 30, no. 5, pp. 541–549, 2008.

[2] A. Govada, C. Renumadhavi, and K. B. Ramesh, “Non-Invasive Blood Glucose Measurement,” *Ijarcce*, vol. 3, no. 1, pp. 1–4, 2014.

[3] A. A. Stratonnikov and V. B. Loschenov, “Evaluation of blood oxygen saturation in vivo from diffuse reflectance spectra,” *J. Biomed. Opt.*, vol. 6, no. 4, p. 457, 2001.

[4] M. Anas, N. Nurun, A. Norali, and M. Normahira, “Non-invasive blood glucose measurement,” *2012 IEEE EMBS Int. Conf. Biomed. Eng. Sci.*, no. December, pp. 503–507, 2012.

[5] A. Tura, A. Maran, and G. Pacini, “Non-invasive glucose monitoring: Assessment of technologies and devices according to quantitative criteria,” *Diabetes Res. Clin. Pract.*, vol. 77, no. 1, pp. 16–40, 2007.

[6] M. A. Arnold, “Non-invasive glucose monitoring,” *Curr. Opin. Biotechnol.*, vol. 7, no. 1, pp. 46–49, 1996.

[7] D. E. Skarda, K. E. Mulier, D. E. Myers, et al. “Dynamic near-infrared spectroscopy measurements in patients with severe sepsis,” *Shock*, vol. 27, pp. 348-353, 2007.

[8] K. Ohashi, H. Yukioka, M. Hayashi, and A. Asada, “Elevated methemoglobin in patients with sepsis,” *Acata Anaesthesiol Scand*, vol. 42, pp. 713–716, 1998.

[9] J. Rem, O. Siggaard-Andersen, B. Norgaard-Pedersen, and S. Sorensen, “Hemoglobin Pigments, Photometer for Oxygen Saturation, Caboxyhemoglobin, and Methemoglobin in Capillary Blood,” *Clin. Chim. Acta*, vol. 42, pp. 101–108, 1972.

[10] W. Zijlstra, A. Buursma, and W. Meeuwsen-van der Roest, “Absorption Spectra of Human Fetal and Adult Oxyhemoglobin, De-Oxyhemoglobin, and Methemoglobin,” *Clin. Chem.*, vol. 37, no. 9, pp. 1633–1638, 1991.

[11] L. Lyngsnes Randeberg, E. Bruzell Roll, L. T. Norvang Nilsen, T. Christensen, and L. O. Svaasand, “In vivo spectroscopy of jaundiced newborn skin reveals more than a bilirubin index,” *Acta Paediatr. Int. J. Paediatr.*, vol. 94, no. 1, pp. 65–71, 2005.

[12] H. H. Maurer, “Multi-analyte procedures for screening for and quantification of drugs in blood, plasma, or serum by liquid chromatography-single stage or tandem mass spectrometry (LC-MS or LC-MS/MS) relevant to clinical and forensic toxicology,” *Clin. Biochem.*, vol. 38, no. 4, pp. 310–318, 2005.

[13] P. Merlani, P. Garnerin, M. Diby, M. Ferring, and B. Ricou, “Quality improvement report: Linking guideline to regular feedback to increase appropriate requests for clinical tests: blood gas analysis in intensive care.,” *BMJ*, vol. 323, no. 7313, pp. 620–4, 2001.

[14] A. A. Stratonnikov and V. B. Loschenov, “Evaluation of blood oxygen saturation in vivo from diffuse reflectance spectra,” *J. Biomed. Opt.*, vol. 6, no. 4, p. 457, 2001.

[15] A. Roggan, M. Friebel, K. Dorschel, A. Hahn, and G. Muller, “Optical Properties of Circulating Human Blood in the Wavelength Range 400-2500 nm,” *J. Biomed. Opt.*, vol. 4, no. 1, pp. 36–46, 1999.

[16] R. R. Anderson and J. A. Parrish, “The optics of human skin,” *J. Invest. Dermatol.*, vol. 77, no. 1, pp. 13–19, 1981.

[17] E. Salomatina, B. Jiang, J. Novak, and A. N. Yaroslavsky, “Optical properties of normal and cancerous human skin in the visible and near-infrared spectral range,” *J. Biomed. Opt.*, vol. 11, no. 6, p. 064026, 2006.

[18] J. W. Feather, M. Hajizadeh-Saffar, G. Leslie, and J. B. Dawson, “A portable scanning reflectance spectrophotometer using visible wavelengths for the rapid measurement of skin pigments,” *Phys. Med. Biol.*, vol. 34, no. 7, pp. 807–820, 1989.

[19] I. J. Bigio and J. R. Mourant, “Ultraviolet and visible spectroscopies for tissue diagnostics: Fluorescence spectroscopy and elastic-scattering spectroscopy,” *Phys. Med. Biol.*, vol. 42, no. 5, pp. 803–814, 1997.

[20] J. T. Olesberg, L. Liu, V. Van Zee, and M. A. Arnold, “In vivo near-infrared spectroscopy of rat skin tissue with varying blood glucose levels,” *Anal. Chem.*, vol. 78, no. 1, pp. 215–223, 2006.

[21] K. Maruo, M. Tsurugi, M. Tamura, and Y. Ozaki, “ In Vivo Noninvasive Measurement of Blood Glucose by Near-Infrared Diffuse-Reflectance Spectroscopy,” *Appl. Spectrosc.*, vol. 57, no. 10, pp. 1236–1244, 2003.

[22] A. D. Edwards, J. S. Wyatt, C. Richardson, D. T. Delpy, M. Cope, and E. O. Reynolds, “Cotside measurement of cerebral blood flow in ill newborn infants by near infrared spectroscopy.,” *Lancet*, vol. 2, no. 8614, pp. 770–1, 1988.

[23] C. Cheung, J. P. Culver, K. Takahashi, J. H. Greenberg, and A. G. Yodh, “In vivo cerebrovascular measurement combining diffuse near-infrared absorption and correlation spectroscopies,” *Phys. Med. Biol.*, vol. 46, no. 8, pp. 2053–2065, 2001.

[24] J. J. Burmeister and M. a Arnold, “Evaluation of measurement sites for noninvasive blood glucose sensing with near-infrared transmission spectroscopy.,” *Clin. Chem.*, vol. 45, pp. 1621–1627, 1999.

[25] D. P. Kingma and J. L. Ba, “ADAM: A Method for Stochastic Optimization,” arXiv:1412.6980 [cs.LG], 2015.

Chapter 5

Vibrational Spectroscopy for Analysis of Glucose Solutions

Mid-infrared transmission and spontaneous Raman scattering spectra of aqueous glucose solutions were measured. The concentration of glucose in the solutions ranged from 0 to 10 mM, which was chosen to simulate the normal variation of blood glucose levels in humans. Partial least squares regression models were trained, validated, and tested on the mid-infrared and Raman spectral data sets, and proved to be accurate predictive models of glucose concentration. The mean squared error of the model based on mid-infrared spectra ranged from 0.10 - 0.74 mM, and that of the Raman-based model ranged from 0.26 - 0.93 mM.

5.1 Introduction

Mid-infrared (MIR) and Raman spectroscopy are both techniques for probing the molecular vibrations of a sample. The vibrational spectra of a given molecule are often highly specific [1], and serve as a strong basis for quantitative analysis of an unknown material.

Sugars such as glucose, fructose, maltose, and sucrose all have distinct vibrational spectra that can be measured by MIR and Raman spectroscopy. The intensity of the spectral features corresponding to vibrational modes are dependent on the concentration of a particular substance in a sample [2], so quantitative spectral measurements can be used to indirectly measure the concentration of these sugars in a solution or even blood, as researchers have demonstrated using MIR [3] and Raman spectroscopy [4,5]. Measuring the concentration of glucose is of particular interest due to the fact that millions of diabetics must monitor their blood glucose levels regularly to avoid health complications. In these experiments, we measure MIR and Raman spectra of aqueous glucose solutions of varying concentrations. We use a subset of these spectra to build Partial Least Squares

(PLS) regression models which we use to predict the concentrations of a separate set of glucose solutions based on their spectra.

5.2 MIR Experiment

We measured MIR spectra using a Fourier Transform Infrared (FTIR) spectrometer (Bruker Tensor II). Glucose solutions were placed in liquid cells (Pike) between two AMTIR windows, which are transparent up to about 14 μm, spaced 25 μm apart. In order to obtain consistent measurements, we performed a series of calibration experiments. The result of these experiments showed that in order to obtain consistent amplitude measurements, our protocol should standardize the time the liquid cell spends in the compartment. Subtle changes in the amplitude of the spectra can be observed due to time spent under exposure to the light source. Although they are subtle, they are on the same scale as differences due to metabolite concentration in simulants at physiological concentrations. Although it is out of scope for the current work, we believe that in vitro measurement can benefit greatly from automation of the measurement protocol to eliminate as much human variability as possible.

Using our refined measurement protocols, we performed high-precision MIR measurements on simulation solutions to develop a predictive model for metabolite concentrations (Fig. 5.1). We created solutions with physiological glucose concentrations (0-10mM), and collected MIR spectra for each. So that our model would be robust and account for differences in the measurement environment such as variation in temperature, humidity, the light source, or the liquid cell, multiple trials were conducted on different days.

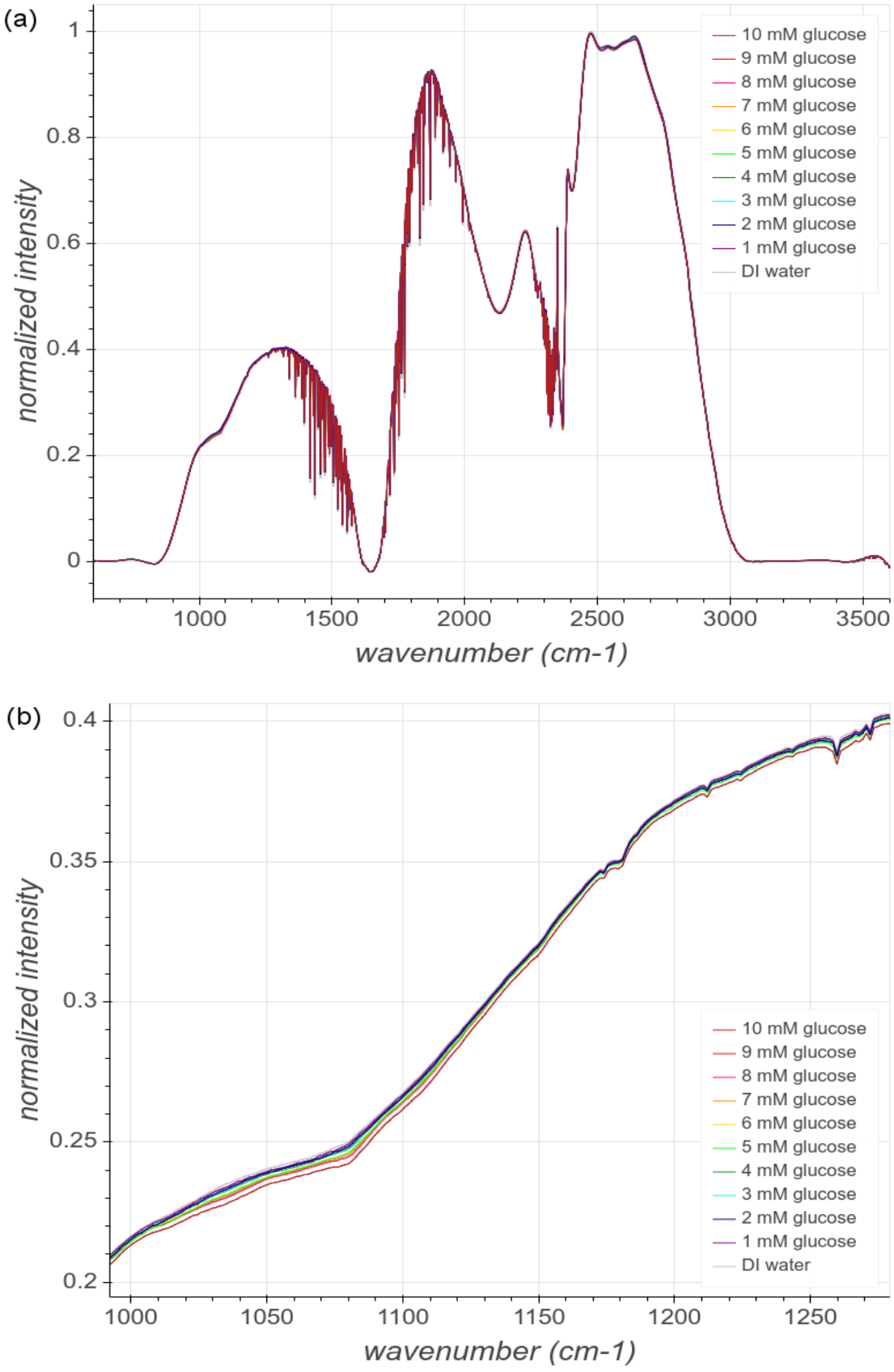

Figure 5.1: MIR glucose spectra with concentrations 0-10 mM. (a) Full spectrum from 600-3600 cm^{-1}. Although the 10 spectra are similar and appear to overlap, there are

subtle differences due to glucose concentration, especially in the 1000-1250 cm^{-1} and 2400-2700 cm^{-1} wavenumber ranges. (b) Zoomed in spectrum from approximately 1000-1250 cm^{-1}. The spectra of higher glucose concentrations have lower intensity in this range, indicating lower transmission or greater absorption due to interactions with glucose.

5.3 Spectral Processing and Modeling

We developed a partial least squares (PLS) regression model based on the MIR spectra of the measured glucose solutions. We trained the model using one set of MIR spectra, validated the model on a second set to prevent over-fitting, and tested its predictive power on a third set. In order to make accurate predictions, we first used our wavelet-based defringing algorithm to remove the fringing artifacts introduced by the parallel inner surfaces of the liquid cell. It was also necessary to take the logarithm of each spectra as transmittance varies with the exponential of concentration. We found that the accuracy of the model was further improved by introducing an internal normalization standard, which was accomplished by dividing each spectra by the spectral intensity at a certain wavenumber. We tested the model with internal normalization over the full range of wavenumbers and found an optimal range that minimized the error of the model. Using one data set as the training set, a second as validation, and a third as the test set, the PLS model predicted the concentrations of the test set with a mean squared error values ranging from 0.10 to 0.74 mM (Fig. 5.2), depending on which sets were used as training and test sets, demonstrating the accuracy of our model.

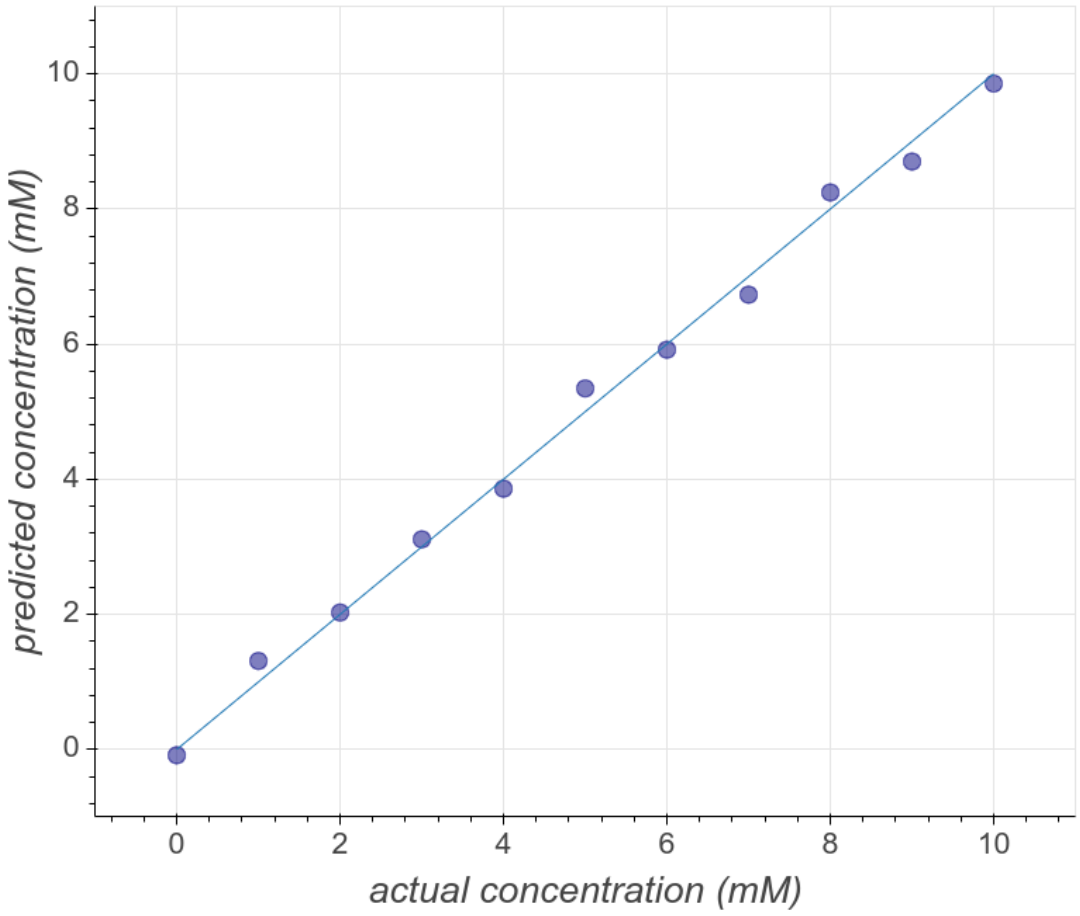

Figure 5.2: PLS glucose concentration prediction based on MIR spectra. Each point represents the glucose concentration prediction of the PLS model using the spectrum from a solution from the testing set. The line represents an idealized glucose prediction model. The data points are generally close to the idealized line, with the greatest deviations being on the order of tenths of mM. The mean squared error is 0.10 mM, indicating the high accuracy of the model.

5.4 Raman Experiment

In order to complement our MIR experiments, we performed a similar set of experiments using Raman spectroscopy. Although MIR and Raman spectra often share similar information about the molecular vibrations of a sample, each spectroscopic method is better suited to certain measurement scenarios. One disadvantage MIR spectroscopy has for in vivo applications is that human tissue, such as skin, greatly absorbs much of the MIR spectrum, making MIR spectral

measurements of anything below the surface of the skin extremely inefficient. Raman spectroscopy has the advantage of being able to use an arbitrary excitation wavelength and chose that most suitable for the measurement application, so excitation wavelengths in the NIR, which have good penetration depth into human tissue are often used for biomedical applications [6,7]. Although absorption isn't an issue for measuring spectra of glucose solutions, we chose 830 nm as our excitation wavelength to show the potential of making similar measurements in vivo.

We measured the spontaneous Raman spectra of aqueous glucose solutions with a modular Raman spectrometer (Wasatch Photonics 830 Raman). The solutions were contained in transparent cuvettes and positioned inside an opaque mounting cell. We first measured glucose solutions with concentrations up to 1000 mM to better identify the key spectral features (Fig. 5.3). These Raman spectra show a significant difference in Raman intensity between the varying glucose solutions, especially at the 1124 cm^{-1} mode and the group of modes at approximately 407, 492, and 592 cm^{-1}.

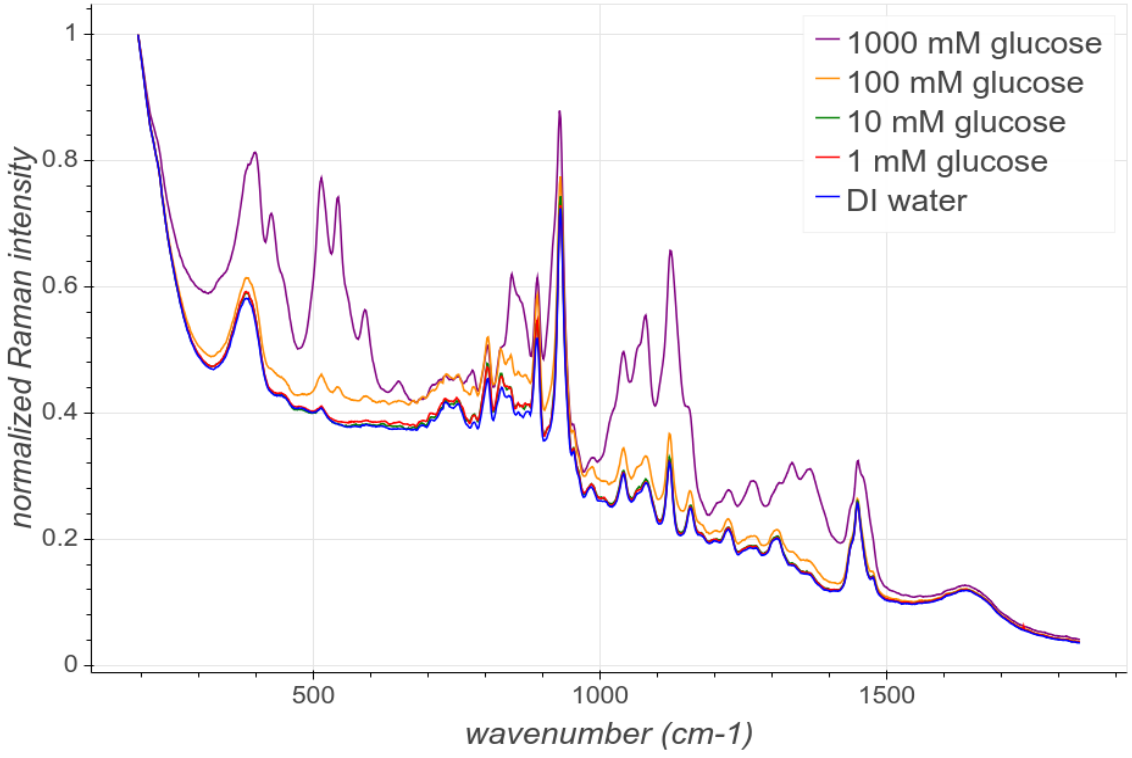

Figure 5.3: Raman spectra of glucose solutions up to 1000 mM in concentration. The high variation in concentration allows better examination of spectral features

corresponding to aqueous glucose. Key features include those at the 1124 cm^{-1} mode and the group of modes at approximately 407, 492, and 592 cm^{-1}.

We also measured a set of solutions with glucose concentrations ranging from 10 mM to 0 mM (only DI water) (Fig. 5.4). This range is useful for study because normal human blood glucose concentration averages at about 5.5 mM. The excitation laser power was 100 mW, and the integration time for spectra point was 10 seconds. Raman spectra were normalized to the highest point on the spectrum in order to account for signal level variation caused by slight differences in cuvette position in the sample mounting apparatus. The Raman spectra of these lower concentration glucose solutions qualitatively appear very similar due to their relatively small differences in concentration. However, there are small, but significant quantitative differences which can be used to make a predictive PLS model (Fig. 5.5). Our PLS model has a mean squared error ranging from 0.26-0.93 mM depending on which sets are used as training, validation, and testing.

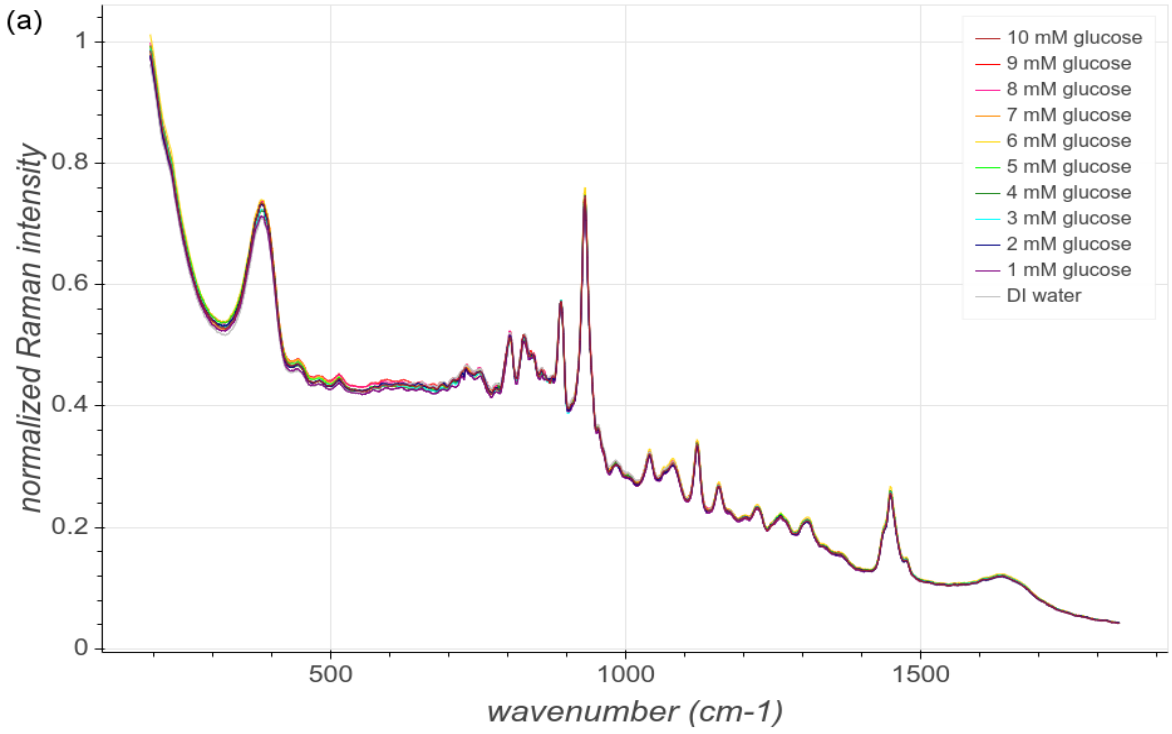

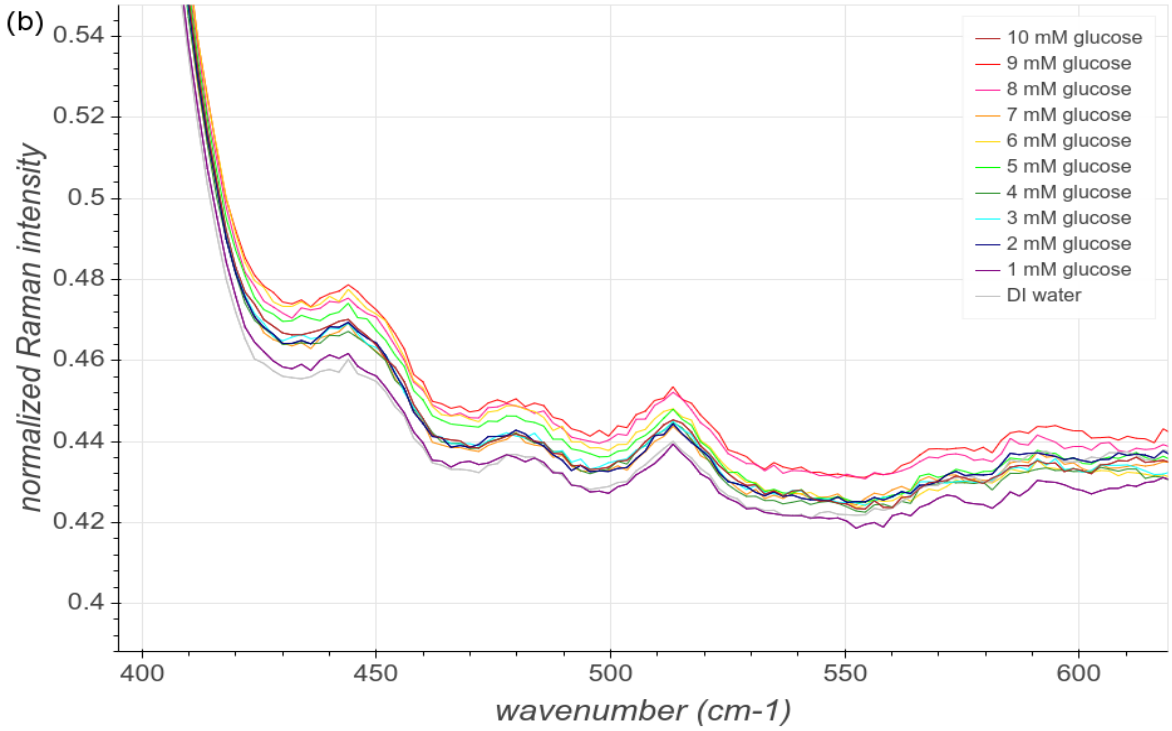

Figure 5.4: Raman spectra of glucose solutions with concentrations 0-10 mM. (a) Full spectrum from about 200-1850 cm^{-1}. Small variations can be seen throughout the spectrum, but especially in the 400-600 cm^{-1} wavenumber range. (b) Zoomed in spectrum. Spectra of higher glucose concentration generally have higher intensity in this range, corresponding to glucose Raman modes.

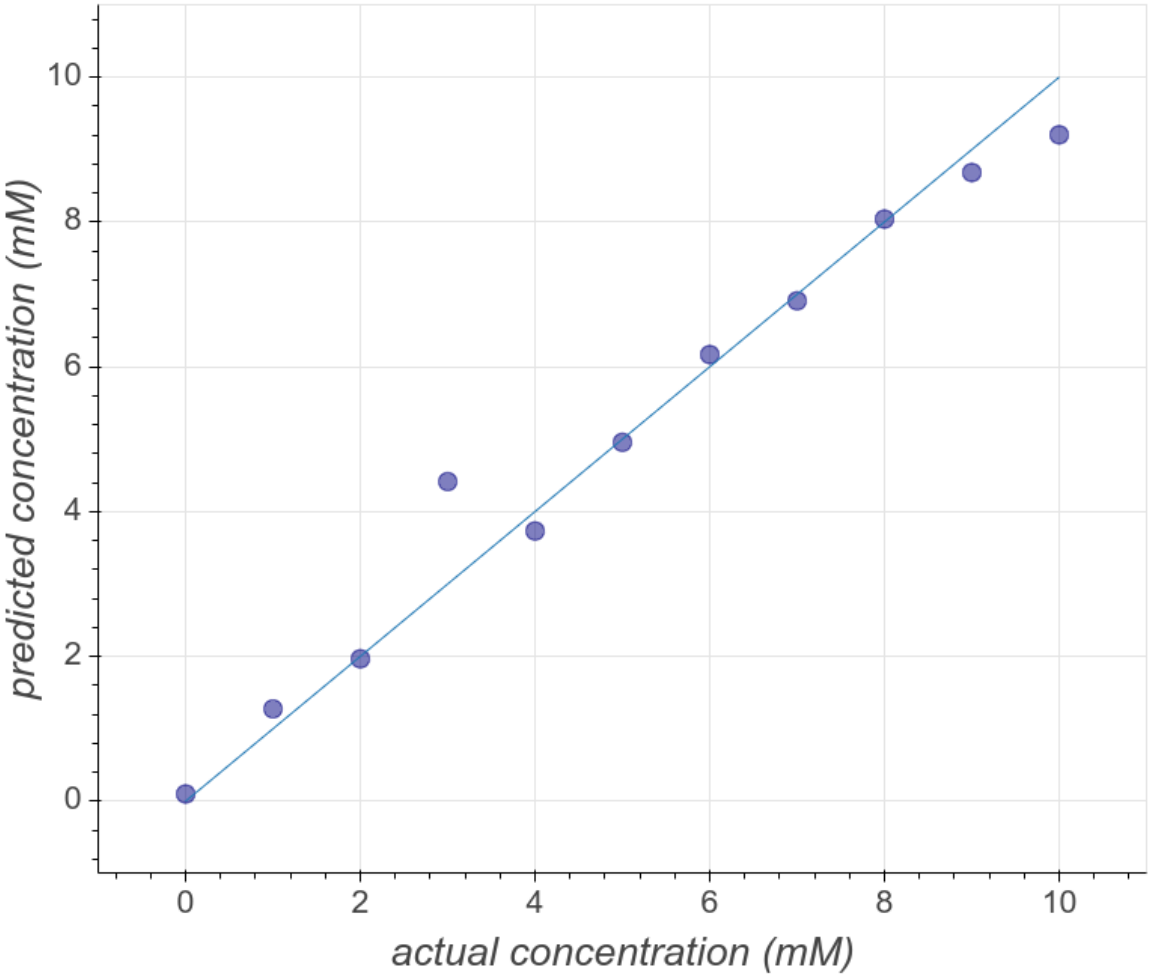

Figure 5.5: Glucose concentration predictions based on Raman spectra of solutions with glucose concentrations from 0 to 10 mM. Each point represents the glucose concentration prediction of the PLS model using the spectrum from a solution from the testing set. The line represents the concentration predictions of an idealized PLS model. The predictions of our Raman-based PLS model are highly accurate for most of the solutions, except for the 3 mM solution. Inaccuracies such as this are to be expected given the small training set of only 11 solutions, and may be due to slight variations in the positioning of the cuvettes in the measurement system. The mean squared error of the PLS model represented here is 0.26 mM. With a different combination of training, validation, and testing sets, the mean squared error of the PLS model varied as high as 0.93 mM, indicating the accuracy of the model is partially dependant on data set.

5.5 Discussion

Although the MIR and Raman spectra of the glucose solutions appear different, they both contain similar information about the vibrational modes of the solutions. The difference in qualitative appearance between the transmission MIR and Raman scattering spectra is to be expected as these are two different spectroscopic modalities with different setups. Furthermore, there was no background subtraction because the PLS algorithm is ambivalent towards background subtraction, and it would only introduce an additional source of error. Our data included the spectrum for DI water, which could be used as a background, but it was more useful as an additional training set for our PLS model. Interestingly, the spectrum of DI water and the spectra of the glucose solutions are similar, indicating that glucose is responsible for only a small component of the overall spectra.

Both the MIR and Raman spectra of 0-10 mM glucose solutions show very subtle differences between spectra of different concentrations. These differences are more clearly visible in the 1000-1250 cm^{-1} range for both modalities and also the 400-600 cm^{-1} range for Raman. In these wavenumber ranges, the intensity generally correlates with concentration, indicating the presence of glucose modes. In other regions of the spectra, there is no correlation between intensity and concentration because either there are no strong glucose modes in these regions or there are other spurious variables obscure them. The PLS model is effective with these data sets because it is able to differentiate between the regions of strong correlation between intensity and glucose concentration and those of weak correlation. Even with relatively small training sets of only 11 spectra, both the MIR-based and Raman-based PLS models were strong predictors of glucose concentration. The mean squared error of the MIR-based PLS model ranged from 0.10-0.74 mM, and that of the Raman-based PLS model ranged from 0.26-0.93 mM. Although the MIR-based model was generally more accurate, both models consistently predicted glucose concentration with error of less than 1 mM. This suggests that as long as the measurements are taken under consistent conditions, as they were in our

experiments, both MIR and Raman spectroscopy have potential for being used in making accurate glucose predictions. Furthermore, building models with larger training sets compensate for small errors, such as that seen in our 3 mM prediction with the Raman-based model. Larger training sets will also be necessary for building accurate models from in vivo measurements, as human tissue has far more constituents than simple glucose solutions, and measured spectra would have greater variation to be accounted for.

5.6 References

[1] F. Shen, Y. Ying, B. Li, Y. Zheng, and J. Hu, “Prediction of sugars and acids in Chinese rice wine by mid-infrared spectroscopy,” *Food Res. Int.*, vol. 44, no. 5, pp. 1521–1527, 2011.

[2] S. Sivakesava, J. Irudayaraj, and A. Demirci, “Monitoring a bioprocess for ethanol production using FT-MIR and FT-Raman spectroscopy,” *J. Ind. Microbiol. Biotechnol.*, vol. 26, no. 4, pp. 185–190, 2001.

[3] S. Sakhamuri, J. Bober, J. Irudayaraj, and A. Demirci, “Simultaneous Determination of Multiple Components in Nisin Fermentation Using FTIR Spectroscopy,” *Process Biochem.*, vol. 37, pp. 371–378, 2004.

[4] J. L. Lambert, J. M. Morookian, S. J. Sirk, and M. S. Borchert, “Measurement of aqueous glucose in a model anterior chamber using Raman spectroscopy,” *J. Raman Spectrosc.*, vol. 33, no. 7, pp. 524–529, 2002.

[5] J. L. Lambert, C. C. Pelletier, and M. Borchert, “Glucose determination in human aqueous humor with Raman spectroscopy,” *J. Biomed. Opt.*, vol. 10, no. 3, p. 031110, 2005.

[6] A Berger, Y. Wang, and M. S. Feld, “Rapid, noninvasive concentration measurements of aqueous biological analytes by near-infrared Raman spectroscopy,” *Appl. Opt.*, vol. 35, no. 1, p. 209, 1996.

[7] A. J. Berger, T.-W. Koo, I. Itzkan, G. Horowitz, and M. S. Feld, “Multicomponent blood analysis by near-infrared Raman spectroscopy,” *Appl. Opt.*, vol. 38, no. 13, p. 2916, 1999.

Chapter 6

Stimulated Raman with Broadband LED Stokes Source for Analysis of Glucose

We demonstrate stimulated Raman gain using a broadband LED Stokes source to measure vibrational spectra of aqueous glucose solutions. This versatile and cost-effective method increases Raman signal for a variety of applications. We measured both stimulated Raman and spontaneous Raman spectra of glucose solutions with concentrations between 2 and 10 mM with a photon counter and lock-in amplifier. We built partial least squares regression models based on both stimulated Raman and spontaneous Raman spectral data measured with each instrument for predicting concentrations of the glucose solutions. The model based on stimulated Raman spectra measured with the lock-in amplifier had the strongest predictive power and predicted the concentrations of the test set of glucose solutions with a mean squared error value an order of magnitude lower than those of the model based on spontaneous Raman spectra.

6.1 Introduction

Stimulated Raman Scattering (SRS) spectroscopy is a powerful technology for high sensitivity quantitative analysis of molecular vibrations. Raman spectra are determined by the fundamental vibrational modes of molecules, and therefore are highly specific compared to spectra generated by other spectroscopic techniques such as NIR absorption spectroscopy [1]. Furthermore, SRS provides a significant signal enhancement compared to the relatively weak spontaneous Raman signal, enabling detection of molecules in highly dilute solutions and a variety of other high sensitivity applications [2]. SRS involves two light sources: pump and Stokes. When the frequency difference between the pump and Stokes sources corresponds to one of the Raman vibrational modes of the molecules in the sample, the molecular

transition probability greatly increases [3]. This technique results in intensity gain at the Stokes frequency, Stimulated Raman Gain (SRG), and intensity loss at the pump frequency, Stimulated Raman Loss (SRL) [4]. Both the SRG and SRL signals can be orders of magnitude higher than the spontaneous Raman signal, and either may be used for molecular detection or imaging [5,6].

The increased stimulated Raman signal enables high sensitivity detection and high contrast imaging with fast integration times and low laser excitation powers, all of which are critical to biomedical applications. Due to the combination of these beneficial attributes, SRS microscopy has been used to great effect for imaging biological tissue in vivo at video-rate speeds [7] In recent years, researchers have developed a wide variety of powerful SRS-based biomedical technologies including three-dimensional spectral imaging of proteins [8], in vivo brain tumor imaging [9], and handheld in vivo SRS microscopes [10]. SRS also holds several advantages compared to Coherent Anti-Stokes Scattering (CARS) spectroscopy, another coherent Raman technology often used for sensitive high-speed imaging. While CARS can be obscured by non-resonant background and autofluorescence, SRS is unaffected by these phenomena [11-13]. Depending on the modulation method used, SRS can reach even higher levels of sensitivity, limited only by shot noise [14]. Finally, SRS spectra are identical to spontaneous Raman spectra, which enables easier analysis and comparison to readily available spontaneous Raman spectra reported in the literature [15].

One limitation of the standard SRS system is that it can only measure the SRG or SRL signal corresponding to a single Raman-active molecular vibration at a time: that with a resonant frequency equal to difference between the pump and Stokes frequencies. This presents a challenge for applications requiring a broader Raman spectrum. Quantitative analysis of complex multi-component samples often relies on a specific vibrational mode, separate from the mode of interest, to serve as a reference measurement or internal standard. For example, in vivo blood glucose level monitoring has been demonstrated via spontaneous Raman spectroscopy with the characteristic glucose mode at 1125 cm^{-1} being the vibrational mode of interest and the hemoglobin mode at 1549 cm^{-1} serving as the internal standard [16]. In order to perform similar types of full spectrum measurements with the benefit of SRS

enhanced signal, researchers have developed innovative SRS systems based on tunable pump or Stokes sources which scan across the Raman spectrum [17,18], tunable optical bandpass filters which filter continuum laser sources down to scanning narrowband pump or Stokes beams [19-21], and femtosecond broadband stimulated Raman spectroscopy (FSRS) [22-24]. FSRS in particular has shown great promise for high speed spectroscopic applications, such as monitoring chemical reactions in real time, due to its high SNR, temporal resolution, and bandwidth. To further reduce noise generated by jitter between the pump and Stokes beam, an FSRS system in which both the narrowband Stokes and continuum pump originate from the same titanium-sapphire laser oscillator has been demonstrated [25]. One drawback of FSRS and many SRS systems in general is the high cost and lack of portability of major components such as femtosecond lasers. Some spectroscopic applications, such as the non-invasive blood monitoring mentioned previously, would benefit from the broadband signal enhancement of FSRS, but must also be cost-effective and adaptable to suit real-world medical environments. For applications in which only a moderate Raman signal enhancement is required, a cost-effective broadband SRS solution is highly desirable.

In this article, we demonstrate a broadband SRS system which uses a high-power LED as the continuum Stokes source and a cw (continuous wave) laser pump. Due to the lower peak power of LEDs compared to pulsed laser sources, this system enhances the Raman signal with lower efficiency than the traditional SRS systems involving two laser sources. However, this prototype system allows for modest SRG of all Raman modes over the spectral width of the LED, while reducing cost and complexity. We test the capability and limitations of this SRS system by measuring Raman spectra of aqueous glucose solutions. We chose to measure glucose solutions as our test samples due to the recent interest in developing non-invasive blood glucose monitoring [16,26,27]. In order to take advantage of the full spectrum data and modest enhancement, we use the measured spectra to build partial least squares regression (PLS) models able to predict the glucose concentration of a solution from its Raman spectrum. Even the modest signal enhancement from our SRS system is valuable for building predictive statistical models such as PLS because data across the entire spectrum contributes to the

model, leading to more accurate predictions [28,29]. We build PLS models from both spontaneous and stimulated Raman spectral data and compare their predictive power for glucose solution concentration.

6.2 Optical Setup

In order to make a fair comparison between broadband stimulated Raman with LED Stokes source and standard spontaneous Raman, we built an optical system capable of employing either spectroscopic technology without any modifications to the optical components. The only difference between the two techniques is that stimulated Raman involves two light sources: both the Stokes LED and pump laser, while spontaneous Raman requires only the pump laser. Regardless of the spectroscopic method, the optical system directs light to the liquid sample, collects and filters the scattered light, and detects the Raman scattered light with a photomultiplier tube (Fig. 6.1). The photomultiplier tube is connected to one of two instruments for the final signal measurement: either a photon counter or lock-in amplifier, and measurements were taken with each instrument for both spontaneous and stimulated Raman for comparison. Optical fibers are used to connect some parts of the optical setup to each other in order to simplify system optimization as adjustments to one portion of the system do not cause misalignment in other parts connected via optical fibers.

For both spontaneous and stimulated Raman spectroscopy, the 532 nm pump (excitation) laser is split by a 10:90 beam splitter, and the smaller portion is reflected towards a photodiode and used as an intensity reference to compensate for laser drift. The transmitted portion of the beam is directed through an aperture stop and laser line filter to clean up the spatial profile of the beam and attenuate any spectral energy apart from the 532 nm laser line. The laser power is 200 mW at the source and is about 150 mW upon reaching the sample. A longpass dichroic beam splitter, oriented 45° with respect to the incident beam, is used to reflect the pump beam to the sample while permitting the LED Stokes beam to be transmitted through towards the same point in the sample. This is possible because the dichroic reflects over 94%

of incident light at or below 532 nm, including the pump beam, and transmits over 93% of light above 541.6 nm, allowing transmission of the Stokes Beam, so that it may stimulate Raman modes with frequency shift of 333 cm^{-1} or greater. The pump and Stokes beams are focused into the volume of the liquid sample by an aspheric lens. Scattered light is collected in the forward direction by an aspheric lens with f-number of 1 and numerical aperture of 0.5. The low f-number and high numerical aperture ensure high collection efficiency. The collected light is collimated and coupled into an optical fiber via coupling lens, filtered by a dielectric longpass filter, and directed into the monochromator. The longpass filter attenuates the intense Rayleigh scattered light from the pump beam to prevent stray light from affecting the final spectra as much as possible. The entrance and exit slits of the monochromator are set at 100 microns to insure enough light passes through while maintaining sufficient spectral resolution. The monochromator must be adjusted manually to measure the Raman signal at each wavelength.

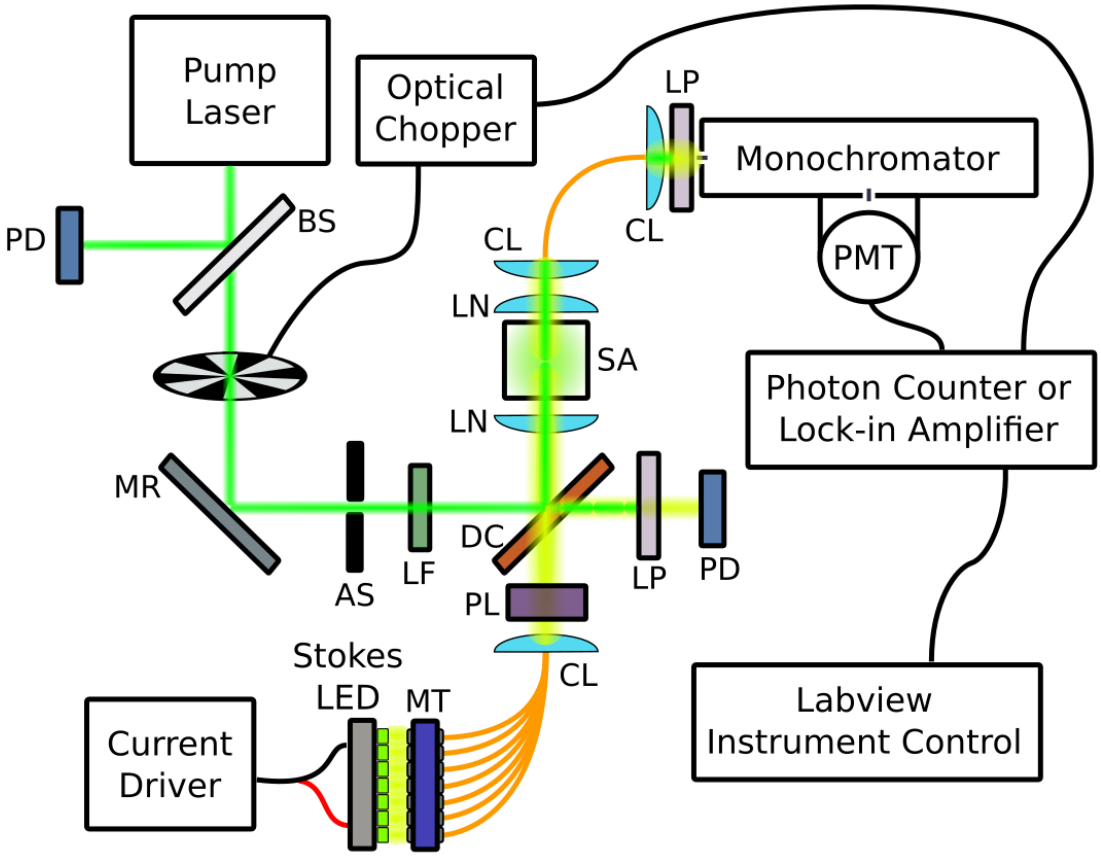

Figure 6.1: Stimulated Raman Spectroscopy system diagram. The beams from the excitation laser and LED are combined via dichroic beam splitter and focused into

the sample. Scattered light is ultimately detected by Photomultiplier Tube (PMT) and measured using either a photon counter or lock-in amplifier. The optical chopper is only used in conjunction with the lock-in amplifier and provides the reference frequency. PD = photodiode, BS = beam splitter, MR = mirror, AS = aperture stop, LF = line filter, DC = dichroic beam splitter, LN = lens, SA = sample, CL = collimating/coupling lens, LP = longpass filter, PL = polarizer, MT = optical fiber mount

Light passing through the monochromator is detected by the photomultiplier tube (Hamamatsu R4220P) and the signal is measured by either the photon counter (Stanford Research Systems SR400) or Lock-in Amplifier (Stanford Research Systems SR810). Our photomultiplier tube is optimized for visible light measurements, which is one of the reasons we chose to use visible pump and Stokes sources. The photomultiplier tube is reverse biased at 1.1 kV, a value chosen to optimize sensitivity without introducing excess noise. The photomultiplier tube is wrapped in layers of aluminum foil to block out stray light from the room. Measurements are taken with the room lights out to further minimize stray light, and the room is cooled to about 15 °C, resulting in a low dark current of 0.48 counts per second measured by the photon counter. Both the photon counter and lock-in amplifier data collection is automated with Labview software.

For stimulated Raman measurements, the Stokes beam is generated by seven high powered LEDs centered at 567 nm. The LEDs are wired together in series and soldered to a single aluminum PCB base with a heat sink for temperature stabilization. The total initial optical power from the LEDs is about 550 mW and is collected by seven ends of a multi-furcated optical fiber connected to a 3D-printed optical fiber mount. The high power is necessary for efficient SRS, especially due to the significant loss inherent to coupling incoherent light into optical fibers. The Stokes beam enters the main portion of the optical system via the multi-furcated optical fiber from the direct opposite side of the dichroic from the sample. The beam is collimated and vertically polarized to match the polarization of the pump beam for optimal stimulated Raman gain. The collimated and polarized beam is transmitted through the dichroic and focused into the sample through the same lens as the pump beam

in order to increase spatial overlap between the focal volumes of the two light sources. At the position of the sample, the Stokes beam power is about 10 mW. A small portion of the beam is reflected by the dichroic beam splitter towards a photodiode and used as an intensity reference. A small portion of the pump beam is also transmitted through the dichroic and is filtered out by a longpass filter so the photodiode monitors only the Stokes beam. By monitoring a reference intensity for both pump and Stokes sources, we found that after turning the light sources on, the intensity decreased over the course of several hours by about 5% and 15% respectively before stabilizing. To mitigate the effect of intensity drift, we took all measurements a minimum of 24 hours after turning on both light sources.

The aqueous glucose solutions are contained in transparent cuvettes (Eppendorf UVette). The path length through the cuvette is 1 cm, and volume of the solutions is 2 mL. The glucose solutions are composed of DI (deionized) water and pharmaceutical grade D-glucose (Sigma Aldrich). The cuvettes are mounted in a 3D-printed mount to insure precise and consistent positioning between the two lenses to minimize any systematic error between different samples due to cuvette position.

6.3 Stimulated Raman Measurements

When taking stimulated Raman measurements with the photon counter, two measurements are required for each data point: a combined signal (I_{com}) in which both the pump and Stokes beams are present and the Stokes signal (I_{Stokes}) in which the pump is blocked. The Stokes measurements were taken immediately after the combined measurement by blocking the pump laser with a manual shutter. The Raman gain, defined as the quotient of the combined and Stokes signals, is increases exponentially with the concentration of the Raman-active molecule and the intensity of the pump signal [22], as shown in equation (1),

$$Raman\ gain = \frac{I_{com}}{I_{Stokes}} = \exp\left(a\,\sigma_R\,c\,z\,I_{pump}\right) \tag{1}$$

where *a* is a proportionality constant, σ_R is the Raman cross section, *c* is the concentration, and *z* is the focal depth in which the beams overlap spatially. We tested our stimulated Raman system on methanol solutions for this relationship between pump intensity and Raman gain. We choose methanol for our test solution because it has greater Raman response than the glucose solutions and has a prominent Raman mode at 565 nm (1062 cm^{-1}), which is close to one of the main glucose Raman modes at 567 nm (1120 cm^{-1}). We increased the pump power from 200 mW to 1 W and found that the Raman gain increased exponentially with the pump power (Fig. 6.2).

(a) (b)

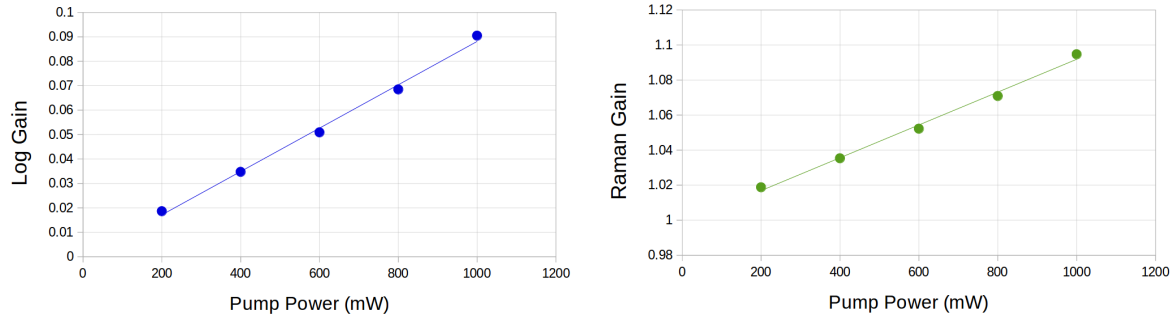

Figure 6.2: (a) Natural logarithm of Raman gain as a function of pump power for 1062 cm^{-1} mode in methanol. The natural logarithm follows a linear trend with respect to pump power with R^2 value of 0.995, indicating that the variation between Raman gain and pump power may be modeled by an exponential fit. (b) However, the Raman gain itself also follows a linear trend with respect to pump power with R^2 value of .993, indicating that the Raman gain may appropriately be modeled by its first-order expansion in equation (3) at these pump power levels.

However, in most stimulated Raman experiments, including ours, which use low to moderate power levels for the pump beam, the gain is relatively small, and equation (2) is satisfied,

$$\gamma = a\,\sigma_R\,c\,z\,I_{pump} \ll 1 \tag{2}$$

so we can approximate the exponential as its first-order expansion (3).

$$e^{\gamma} \approx 1 + \gamma \tag{3}$$

To make the significance of our results more apparent, we define the difference between the combined and Stokes measurements to be the stimulated Raman gain signal (ΔI_{SRG}) (4).

$$\Delta I_{SRG} = I_{com} - I_{Stokes} \tag{4}$$

Then, substituting equations (3) and (4) into equation (1), we arrive at equation (5):

$$\frac{I_{com}}{I_{Stokes}} = \frac{I_{Stokes} + \Delta I_{SRG}}{I_{Stokes}} \approx 1 + a \sigma_R c z I_{pump} \tag{5}$$

which simplifies to

$$\Delta I_{SRG} \approx a \sigma_R c z I_{pump} I_{Stokes} \tag{6}$$

showing that the SRG signal is proportional to both the pump and Stokes intensities in our small signal approximation.

All stimulated Raman spectra measured using the photon counter were calculated as a difference between the combined and Stokes signals for a particular glucose solution sample (Fig. 6.3) according to equation (4) instead of as the quotient in equation (1) in this report. This approximation is made in order to make comparing spectra more straightforward as both spontaneous and SRG difference spectra share the same units of counts while the Raman Gain quotient is a unitless quantity. Furthermore, the measurements taken by the lock-in amplifier are essentially difference measurements as the lock-in signal is proportional to the amplitude of the component of the input signal varying at the frequency of the optical chopper. Although the SRG difference signal is proportional to the Stokes signal which varies with frequency shift, this did not significantly affect the predictive power of our partial least squares regression models.

(a)

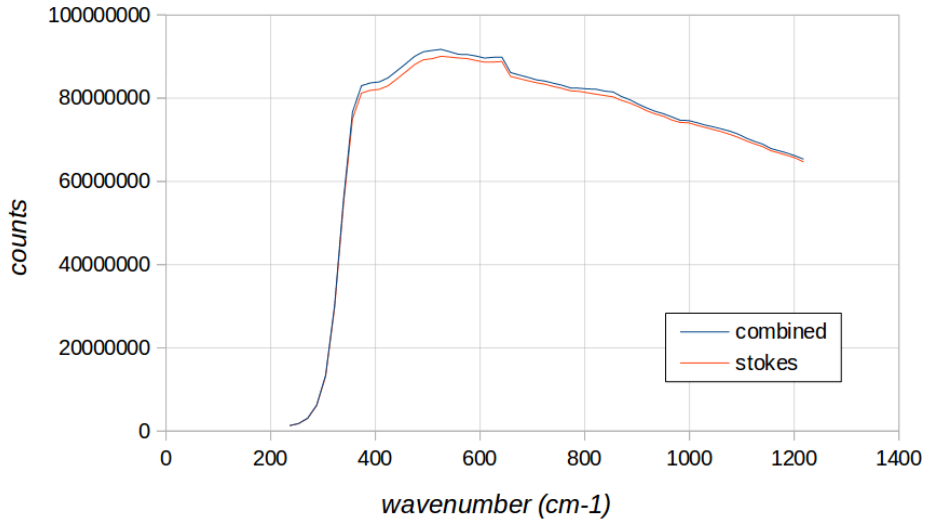

(b)

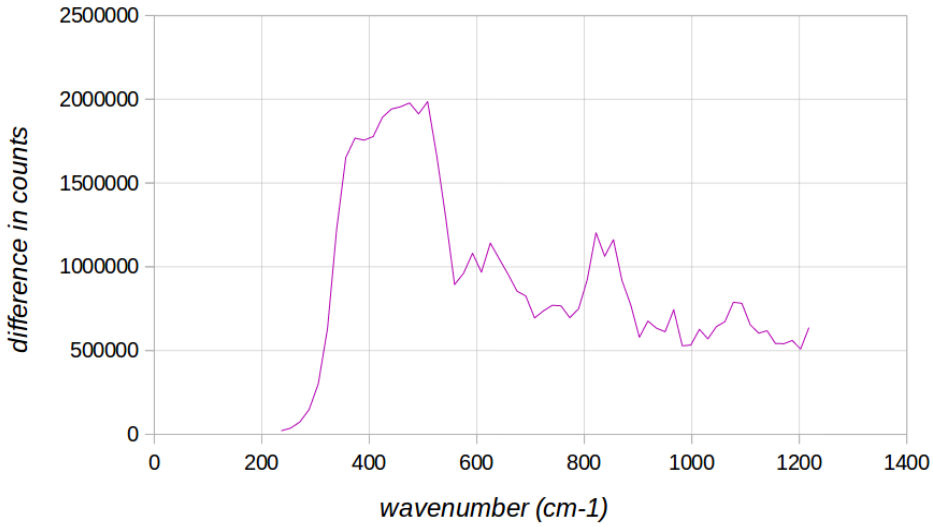

Figure 6.3: (a) Combined (pump laser and Stokes LED) and Stokes (only Stokes LED) signals for 10 mM glucose sample measured via photon counter. (b) Unnormalized Stimulated Raman Gain signal is approximated as the difference between the combined and Stokes signals.

In order to build robust numerical models that account for intensity drift of the pump laser and Stokes LED throughout the data collection process, intensity references were taken for both light sources with photodiodes for each data point. Since the stimulated Raman gain is proportional to both the pump and Stokes

intensity, each stimulated Raman gain measurement was divided by both the pump and Stokes reference taken for that point before the spectra were used by the partial least squares model. In order to compare these processed normalized Raman spectra to the spontaneous Raman spectra, each spontaneous measurement was divided by the pump reference for that point and the average of the Stokes references for the stimulated measurements since the spontaneous measurements do not involve the Stokes LED but must still be divided by an average Stokes reference for fair comparison to the normalized stimulated spectra. This normalization process improved the predictive power of our partial least squares models overall with the normalization to the pump reference being more significant than that of the Stokes reference.

6.4 Experimental Process

We measured the spontaneous and stimulated Raman spectra of aqueous glucose solutions with our optical setup. The solutions were contained in cuvettes and glucose concentrations ranged from 10 mM to 0 mM (only DI water). This range is useful for study because normal human blood glucose concentration averages at about 5.5 mM. Using both the photon counter and lock-in amplifier, we collected both spontaneous and stimulated Raman spectra for three separate glucose solutions at each concentration level. This would allow us to conveniently divide the data into training, validation, and test sets later when analyzing the data. We collected data from 540 to 570 nm on our monochromator for each sample, which resulted in Raman spectra from 289 to 1262 cm^{-1} (conversion to wavenumbers includes an instrument-specific calibration offset). Measurements were taken one data point at a time every 0.5 nm from 540 to 570 nm, which accounts for most of the significant spectral features of glucose. The integration time for each measurement was 5 seconds using the photon counter and the time constant for the lock-in amplifier was 3 seconds. The average dark current of 2.4 counts per 5 seconds was subtracted from each photon counter measurement.

6.5 Spontaneous and Stimulated Raman Comparison

The glucose solution spectra measured via spontaneous and stimulated Raman spectroscopy methods show similar spectral features as those investigated in the literature [30,31]. Due to using a monochromator and taking one data point rather than a full spectrum at a time, our spectra have relatively low resolution, but we can identify groups of characteristic Raman modes. The spectral feature around 1092-1139 cm^{-1} likely corresponds to the COH bending mode characteristic of glucose, that between 853-918 cm^{-1} is the combination of C-H and C-C bending and stretching modes of both alpha and beta glucose anomers, that around 675-724 cm^{-1} is composed of deformations in the ring structure, and the large group of features between 424-575 cm^{-1} is likely the combination of C-C-O deformation modes and endocyclic vibrational modes of the ring structure. The normalized Raman intensity is generally higher for the stimulated Raman measurements compared to the spontaneous Raman measurements throughout the spectra for both measurements taken with the photon counter and with the lock-in amplifier (Fig. 6.4). This suggests that the the pump laser is interacting with the Stokes LED and causing stimulated Raman gain in the glucose solutions. It is likely that our stimulated data are the result of both the spontaneous and stimulated Raman effects scattering light simultaneously, but here we are concerned only with the total signal measured using both the pump and Stokes LED and not what portion of this signal is generated by the stimulated Raman effect.

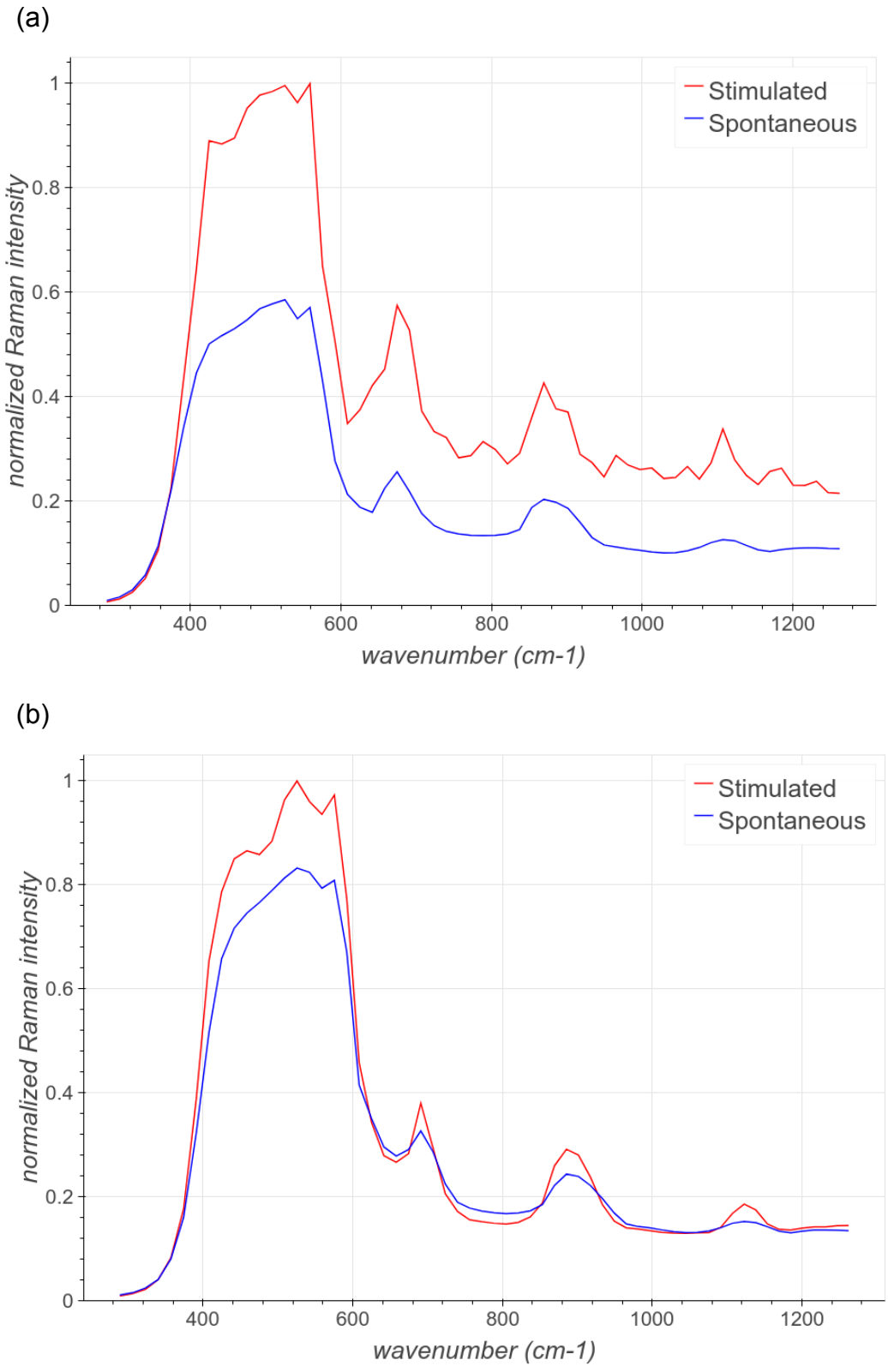

Figure 6.4: Comparison of stimulated and spontaneous Raman spectra of a 10 mM glucose solution measured with (a) photon counter and (b) lock-in amplifier. The enhancement between stimulated and spontaneous spectra is greater with the

photon counter spectra, but the stimulated photon counter spectra also has significantly higher noise.

The relative intensity increase between stimulated and spontaneous Raman was greater for for the measurements taken with the photon counter than those taken with the lock-in amplifier. For the photon counter, the stimulated measurements were 1.5-3 times higher than the spontaneous measurements across the spectra for a given glucose solution. However, this enhancement factor was not strongly correlated with the Raman modes, so the relative increase between stimulated and spontaneous measurements was similar for both Raman-active and non-Raman-active regions of the spectra. In contrast, the stimulated measurements taken with the lock-in amplifier were only 1.05-1.3 times higher than the spontaneous measurements, but this enhancement factor was strongly correlated with the Raman modes. The enhancement factor was 1.2-1.3 around the Raman-active regions while only 1.05-1.15 for the non-Raman-active regions. The contrast between the Raman-active and non-Raman-active regions in the lock-in amplifier measurements is advantageous for numerical analysis since the intensity of the glucose Raman modes are proportional to glucose concentration.

In addition to having lower contrast between Raman-active and non-Raman-active regions, another weakness of our photon counter stimulated Raman measurements is noise. Across all spectra, the average coefficient of variation, a measure of relative noise and defined as the quotient of the standard deviation and mean, is 16% for photon counter stimulated, 0.38% for photon counter spontaneous, 0.29% for lock-in stimulated, and 0.31% for lock-in spontaneous measurements. The photon counter stimulated Raman measurement noise is almost 2 orders of magnitude higher than all other measurement techniques, which can be confirmed qualitatively by the noiser photon counter stimulated Raman spectra (Fig. 6.5). While the lock-in amplifier did reduce the noise slightly from 0.38% to 0.31% for the spontaneous measurements, it is clearly most useful in reducing the stimulated measurement noise from 16% to 0.29%. Although monitoring the reference intensities of both the pump laser and Stokes LED compensated for intensity drift to some extent, the Stokes signal alone measured by the photon counter was almost 2

orders of magnitude higher across the spectrum, so any fluctuations in the LED would have a relatively large effect on the stimulated Raman signal. Overall, the additional noise introduced by the LED is a greater detriment to the stimulated photon counter data than any signal enhancement for numerical analysis.

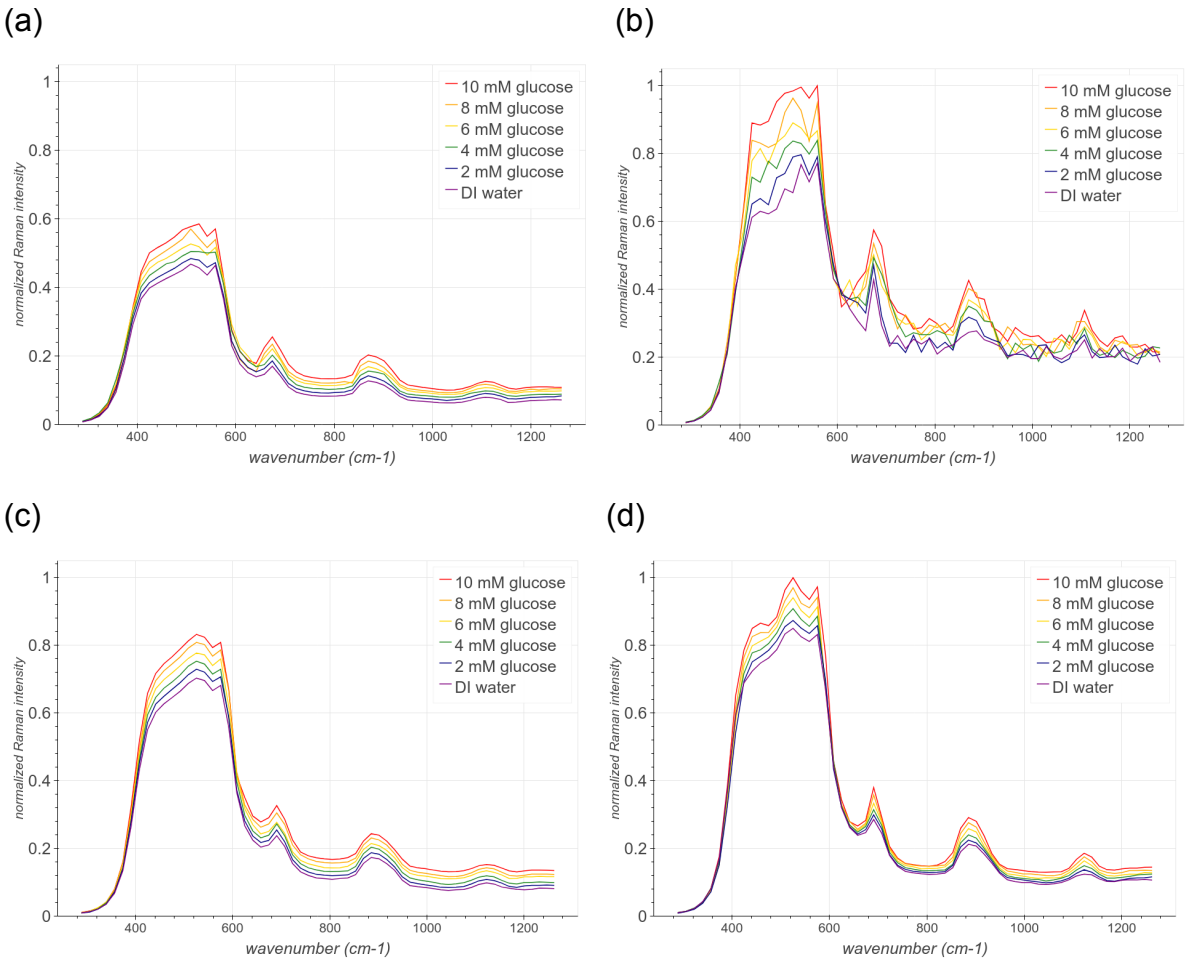

Figure 6.5: (a) Photon counter spontaneous, (b) photon counter stimulated, (c) lock-in spontaneous, (d) lock-in stimulated Raman spectra of glucose solutions with concentrations from 0-10 mM. Both sets of photon counter spectra are normalized to the highest point of the photon counter stimulated data, and both sets of lock-in spectra are similarly normalized to the highest point of the lock-in stimulated data. Differentiation between the glucose solutions of different concentration can be seen for all measurement techniques. The relative Raman intensity is generally higher for the stimulated spectra compared to the respective spontaneous spectra, but the enhancement factor between stimulated and spontaneous measurements is higher for the photon counter measurements overall. The photon counter stimulated spectra

are significantly noisier than the other spectra. The stimulated lock-in spectra show slightly narrower spectral features than the corresponding spontaneous spectra, and Raman modes can be resolved to a slightly higher degree in the 424-575 cm^{-1} region.

Both spontaneous and stimulated Raman spectra of glucose solutions measured with either the photon counter or lock-in amplifier show a significant difference in Raman intensity between the varying glucose solutions (0, 2, 4, 6, 8,10 mM), especially at the group of Raman features between 424-575 cm^{-1} (Fig. 6.5). This enables any of the four sets of data to be used as a training set for a statistical model, such as partial least squares, which would predict the glucose concentration of an unknown solution given its Raman spectrum. However, the stimulated Raman spectra measured with the lock-in amplifier is the best set of data for building the predictive model because of its enhanced signal and low noise. Compared to the spontaneous lock-in spectra, the stimulated lock-in spectra are slightly enhanced, with the regions immediately surrounding Raman modes showing the greatest signal increase. These regions are strongly correlated with glucose concentration, and are useful in differentiating spectra from solutions of different concentrations. Although the stimulated photon counter spectra show even greater overall enhancement than the stimulated lock-in spectra, the enhancement factor is less correlated with Raman modes, and more importantly, these spectra have significantly greater noise, making them a weaker data set for building a predictive model.

6.6 Partial Least Squares Regression Model

The partial least squares (PLS) regression is a simple statistical model which can be used for predicting concentrations based on spectral data. In this study, we use PLS to test and compare the predictive power of our spontaneous and stimulated Raman spectral data for predicting concentrations of glucose solutions. We programmed our PLS model in Python using the scikit-learn package [32]. We analyzed our Raman data over the full collected spectral range of 289-1262 cm^{-1},

and two smaller portions of the spectrum: 458-625 cm^{-1} and 642-1129 cm^{-1}. Since we measured three separate glucose solutions for each concentration value, the first set of measurements for all concentrations 0-10 mM was the training set, the second was the validation set, and the third was the test set. In order to find the optimal number of PLS components for the model, we trained and validated the model using a progressively higher number of PLS components until the mean squared error of the prediction increased, signifying overfitting. Therefore, the previous number of components was optimal. The optimal number of components for the PLS model based on photon counter stimulated spectra was 2 for each spectral range, likely due the greater noise of these spectra. The number of components for the PLS model based on photon counter spontaneous spectra was 3 or 4 depending on spectral range, and that for the lock-in spontaneous and stimulated spectra was 4 or 5 depending on spectral range. Generally, the greater number of components the PLS model can use without overfitting, the stronger the predictive power of the model. Then, the trained and validated model predicted the glucose concentrations based on the test data set, and these predictions were compared to the actual glucose concentration values (Fig. 6.6). The mean squared error between the predicted and actual glucose concentration measured the predictive power of each model (Fig. 6.7), with lower error signifying higher predictive power of the model.

(a) (b)

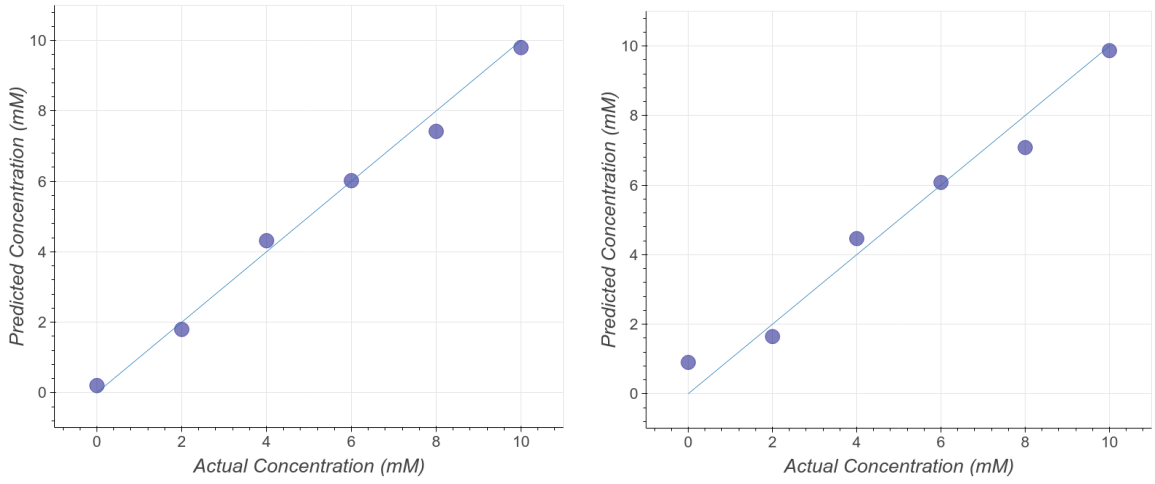

(c) (d)

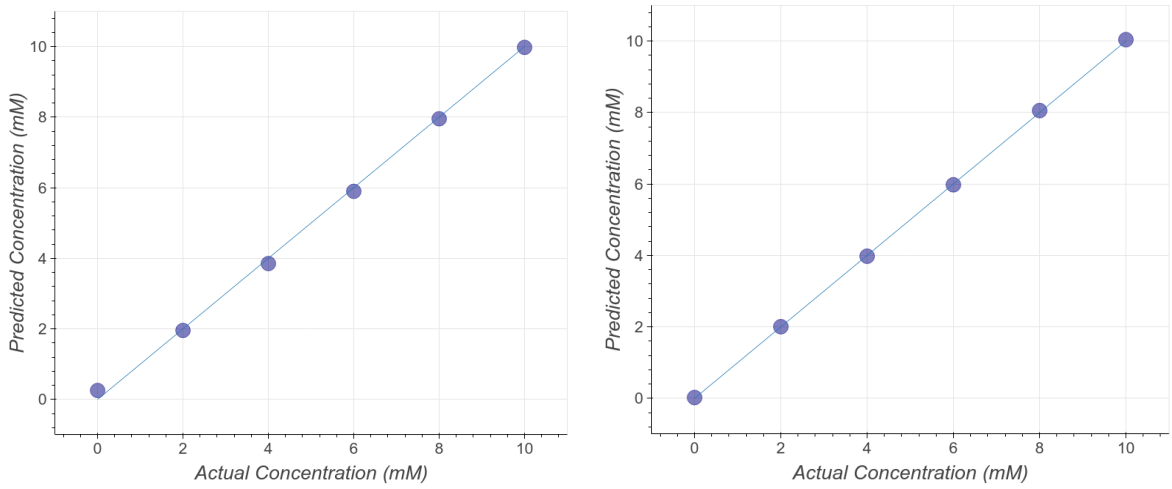

Figure 6.6: PLS model predicted glucose concentration with respect to actual concentration using the full spectrum of data from each of the four measurement methods: (a) Photon counter spontaneous (R^2 = 0.9995), (b) photon counter stimulated (R^2 = 0.987), (c) lock-in spontaneous (R^2 = 0.9998), (d) lock-in stimulated (R^2 = 0.9998). The greater the strength of the linear regression fit, the lower the mean squared error, and the stronger the predictive power of the PLS model.

Photon Counter

Range	Spontaneous	Stimulated
289-1262 cm^{-1}	0.0141 mM	0.694 mM
458-625 cm^{-1}	0.0933 mM	0.337 mM
642-1139 cm^{-1}	0.0467 mM	0.806 mM

Lock-in Amplifier

Range	Spontaneous	Stimulated
289-1262 cm^{-1}	1.70×10^{-2} mM	9.96×10^{-4} mM
458-625 cm^{-1}	7.02×10^{-3} mM	1.84×10^{-3} mM
642-1139 cm^{-1}	1.73×10^{-2} mM	1.04×10^{-3} mM

Figure 6.7: Mean squared error between predicted and actual glucose concentrations for each measurement method over three different spectral ranges. Lower mean squared error values indicate stronger predictive power of the model, so

the PLS model based on lock-in stimulated data was consistently the strongest predictive model.

The mean squared error between predicted and actual glucose concentrations for the PLS model based on the full spectral range of lock-in stimulated Raman data is as low as 9.96×10^{-4} mM, which is the lowest mean squared error from any of the models based on data from any of the measurement methods. The mean squared error values from the lock-in stimulated Raman data are about an order of magnitude smaller than those from either of the spontaneous Raman data and over 2 orders of magnitude smaller than the mean squared error values from the photon counter stimulated Raman data. When using the lock-in amplifier to reduce error caused by the Stokes LED, the PLS models based on stimulated Raman data are consistently the strongest glucose concentration predicting models. Interestingly, the Raman intensity values from the lock-in stimulated data are only slightly increased compared to the spontaneous data, but the PLS model based on stimulated data is significantly stronger, likely due in part to the slightly narrower Raman modes of the stimulated spectra. The stimulated model's higher R-squared value of the linear regression between predicted and actual concentration further corroborates this result. Furthermore, when the training, validation, and test sets are switched around; for example, the second set is training, third is validation, and first is test; the results are similar, showing that the lock-in stimulated model is robust and consistent.

6.7 Discussion

This study demonstrates the viability of broadband stimulated Raman with an LED Stokes source and shows the stronger predictive power of a PLS model based on this stimulated Raman data compared to spontaneous Raman when using a lock-in amplifier to reduce noise. With further developments, this technology may be useful for improved cost-effective spectroscopic molecular identification and concentration prediction in a variety of fields. Prediction of glucose concentration has particularly useful biomedical applications in non-invasive blood glucose level

monitoring. However, it is important to note that this technology has several limitations, and the enhancement of Raman modes achieved by stimulated Raman gain this way is relatively small compared to traditional SRS, broadband FSRS, and other enhancement technologies, such as surface-enhanced Raman spectroscopy (SERS). That being said, broadband LED stimulated Raman is intended to be a cost-effective solution for applications that would benefit from a more modest signal enhancement.

While our setup was designed to demonstrate broadband stimulated Raman, the detection system, specifically the monochromator and photomultiplier tube, could be improved to make taking spectral measurements more practical while removing sources of signal loss. We decided to use the photomultiplier because of its high sensitivity and dynamic range. This was necessary because the unfiltered light from the Stokes LED would saturate a detector with lower dynamic range, and we needed to detect the relatively small stimulated Raman signal on top of the LED signal. Due to using a photomultiplier tube, a monochromator was necessary to isolate a single wavelength, so measuring a full spectrum was accomplished one point at a time. This made taking measurements a time-intensive and impractical process. Furthermore, our signal experienced significant loss through the monochromator. Replacing the monochromator and photomultiplier with a high dynamic range spectrometer would dramatically speed up the measurement process and potentially increase overall signal to noise ratio.

The LED introduces several challenges to the Raman system. As an incoherent light source, the LED light diffracts quickly, and loses a significant amount of signal when coupled into the multi-furcated fiber. This results in a Stokes source orders of magnitude lower in intensity than the pump at the sample, which leads to low stimulated Raman gain. The LED also adds noise though fluctuations and intensity drift, which may counteract the benefit of creating stimulated Raman. Since the intensity of the Stokes LED is almost 2 orders of magnitude higher than that of the stimulated Raman signal, even the Poisson noise of the LED is significant relative of the stimulated signal. This effect of noise from both the LED and laser was greatly mitigated by using an optical chopper to modulate the pump beam and detecting the stimulated Raman gain signal with a lock-in amplifier synchronized to

the modulation of the pump. However, using a lock-in amplifier adds a significant cost to the system, especially if a multi-channel lock-in amplifier would be used to measure a full spectrum all at once. Given cost-effectiveness is one of the main goals of this LED-based stimulated Raman system, the high cost of multi-channel lock-in amplifiers is currently a significant barrier to the practical application of this technology, but the development of cost-effective digital lock-in amplifiers is an active area of research [33,34]. It may also be possible to use the relatively noisy data collected without the lock-in amplifier, using a photon counter in our case or potentially a spectrometer, if the statistical models used were more robust to noise than our partial least squares model. This could be done, in part, by designing a model that includes a penalty that guards against overfitting.

We designed our stimulated Raman system for monitoring glucose concentrations rather than imaging, but broadband LED stimulated Raman also has potential imaging applications. However, aberrations of the LED light would have to be considered, and the imaging resolution would be limited by LED spot size, which is slightly larger than the laser spot size in our setup. Biomedical imaging would require further modifications including lowering the laser power to prevent burning of biological tissue and using NIR wavelengths instead of visible for greater depth of penetration.

6.8 Temperature Stability

Temperature changes in the glucose solution sample could potentially alter the Raman spectra, so we conducted a series of experiments to test whether or not the long exposure of the focused laser and LED beams had any effect on the resulting Raman measurements, either spontaneous or stimulated. Using the 10 mM glucose sample and the same integration time of 5 seconds as in the other experiments, we first continuously measured the spontaneous Raman intensity at a single frequency shift value for 10 minutes, for a total of 120 individual measurements. Then, we measured the stimulated Raman intensity for 10 minutes at the same frequency shift value by subtracting the alternating combined and

Stokes measurements as usual. Given each stimulated Raman measurement is the difference of two consecutive measurements, this resulted in 60 stimulated Raman measurements total. This process was performed at 592, 886, 1124, 2101, and 3400 cm^{-1}. The Raman modes at 592 and 1124 cm^{-1} are two of the most prominent in the spectra we collected, with that at 592 cm^{-1} being the global maximum and that at 1124 cm^{-1} being the mode which experienced the greatest increase between stimulated Raman and spontaneous Raman. We decided to also take measurements at 886 and 2101 cm^{-1} in order to test if there was a temperature effect on the baseline or off-peak regions, and the highest point of the strong group of water modes, 3400 cm^{-1}, was chosen to see if the spectral features related to water would change. Since we were testing the possibility of the laser heating the samples and effecting the Raman measurements, there was a 10 minute gap between rounds of measurements so the sample could cool if needed. Three rounds of measurements were taken at each of the five frequency shift values.

Our experiments showed no significant time-dependent Raman intensity change in any of the tests, suggesting that whatever heating effect the beams may have had on the samples was not significant enough to alter the Raman spectra. This is important because it rules out heating as a potential systematic source of error for our spectral measurements and allows us to make fair comparisons between our spontaneous and stimulated Raman measurements.

6.9 References

[1] N. C. Dingari, I. Barman, G. P. Singh, J. W. Kang, R. R. Dasari, and M. S. Feld, “Investigation of the specificity of Raman spectroscopy in non-invasive blood glucose measurements,” *Anal. Bioanal. Chem.*, vol. 400, no. 9, pp. 2871–2880, Jul. 2011.

[2] P. Nandakumar, A. Kovalev, and A. Volkmer, “Vibrational imaging based on stimulated Raman scattering microscopy,” *New J. Phys.*, vol. 11, no. 3, p. 33026, 2009.

[3] J.-X. Cheng and X. S. Xie, “Vibrational spectroscopic imaging of living systems: An emerging platform for biology and medicine,” *Science (80-.).*, vol. 350, no. 6264, pp. aaa8870-aaa8870, 2015.

[4] C.-S. Liao and J.-X. Cheng, “In Situ and In Vivo Molecular Analysis by Coherent Raman Scattering Microscopy,” *Annu. Rev. Anal. Chem.*, vol. 9, no. 1, pp. 69–93, 2016.

[5] E. R. Andresen, P. Berto, and H. Rigneault, “Stimulated Raman scattering microscopy by spectral focusing and fiber-generated soliton as Stokes pulse,” *Opt. Lett.*, vol. 36, no. 13, p. 2387, 2011.

[6] D. Zhang, M. N. Slipchenko, and J. X. Cheng, “Highly sensitive vibrational imaging by femtosecond pulse stimulated raman loss,” *J. Phys. Chem. Lett.*, vol. 2, no. 11, pp. 1248–1253, 2011.

[7] B. G. Saar, C. W. Freudiger, J. Reichman, C. M. Stanley, G. R. Holtom, and X. S. Xie, “Video-Rate Molecular Imaging in Vivo with Stimulated Raman Scattering.,” *Sci. (Washington, DC, United States)*, vol. 330, no. 6009, pp. 1368–1370, 2010.

[8] C. W. Freudiger, W. Min, G. R. Holtom, B. Xu, M. Dantus, and X. S. Xie, “Highly specific label-free molecular imaging with spectrally tailored excitation-stimulated Raman scattering (STE-SRS) microscopy,” *Nat. Photonics*, vol. 5, no. 2, pp. 103–109, 2011.

[9] M. Ji *et al.*, “Detection of human brain tumor infiltration with quantitative stimulated Raman scattering microscopy,” *Sci. Transl. Med.*, vol. 7, no. 309, p. 309ra163-309ra163, 2015.

[10] C. S. Liao *et al.*, “In Vivo and in Situ Spectroscopic Imaging by a Handheld Stimulated Raman Scattering Microscope,” *ACS Photonics*, vol. 5, no. 3, pp. 947–954, 2018.

[11] T. W. Kee and M. T. Cicerone, “Simple approach to one-laser, broadband coherent anti-Stokes Raman scattering microscopy,” *Opt. Lett.*, vol. 29, no. 23, pp. 2701–2703, 2004.

[12] H. T. Beier, G. D. Noojin, and B. A. Rockwell, “Stimulated Raman scattering using a single femtosecond oscillator with flexibility for imaging and spectral applications,” *Opt. Express*, vol. 19, no. 20, p. 18885, 2011.

[13] K. Yen, T. T. Le, A. Bansal, S. D. Narasimhan, J. X. Cheng, and H. A. Tissenbaum, “A comparative study of fat storage quantitation in nematode Caenorhabditis elegans using label and label-free methods,” *PLoS One*, vol. 5, no. 9, pp. 1–10, 2010.

[14] Y. Ozeki, F. Dake, S. Kajiyama, K. Fukui, and K. Itoh, “Analysis and experimental assessment of the sensitivity of stimulated Raman scattering microscopy,” *Opt. Express*, vol. 17, no. 5, p. 3651, 2009.

[15] W. Min, C. W. Freudiger, S. Lu, and X. S. Xie, “Coherent Nonlinear Optical Imaging: Beyond Fluorescence Microscopy,” *Annu. Rev. Phys. Chem.*, vol. 62, no. 1, pp. 507–530, 2011.

[16] J. Shao *et al.*, “In Vivo Blood Glucose Quantification Using Raman Spectroscopy,” *PLoS One*, 2012.

[17] P. N. Malevich *et al.*, “Ultrafast-laser-induced backward stimulated Raman scattering for tracing atmospheric gases,” *Opt. Express*, vol. 20, no. 17, p. 18784, 2012.

[18] T. Steinle *et al.*, “Synchronization-free all-solid-state laser system for stimulated Raman scattering microscopy,” *Light Sci. Appl.*, vol. 5, no. 10, pp. 1–6, 2016.

[19] Y. Ozeki, W. Umemura, K. Sumimura, N. Nishizawa, K. Fukui, and K. Itoh, “Stimulated Raman hyperspectral imaging based on spectral filtering of broadband fiber laser pulses,” *Opt. Lett.*, vol. 37, no. 3, p. 431, 2012.

[20] D. Fu *et al.*, “Quantitative Chemical Imaging with Multiplex Stimulated Raman Scattering Microscopy,” *J. Am. Chem. Soc.*, vol. 134, no. 8, pp. 3623–3626, 2012.

[21] Z. Meng, G. I. Petrov, and V. V. Yakovlev, “Pure electrical, highly-efficient and sidelobe free coherent Raman spectroscopy using acousto-optics tunable filter (AOTF),” *Sci. Rep.*, vol. 6, no. February, pp. 1–7, 2016.

[22] D. W. McCamant, P. Kukura, S. Yoon, and R. A. Mathies, “Femtosecond broadband stimulated Raman spectroscopy: Apparatus and methods,” *Rev. Sci. Instrum.*, vol. 75, no. 11, pp. 4971–4980, 2004.

[23] P. Kukura, D. W. McCamant, and R. A. Mathies, “Femtosecond Stimulated Raman Spectroscopy,” *Annu. Rev. Phys. Chem.*, vol. 58, no. 1, pp. 461–488, 2007.

[24] E. Ploetz, S. Laimgruber, S. Berner, W. Zinth, and P. Gilch, “Femtosecond stimulated Raman microscopy,” *Appl. Phys. B Lasers Opt.*, vol. 87, no. 3, pp. 389–393, 2007.

[25] K. Seto, Y. Okuda, E. Tokunaga, and T. Kobayashi, “Development of a multiplex stimulated Raman microscope for spectral imaging through multi-channel lock-in detection,” *Rev. Sci. Instrum.*, vol. 84, no. 8, 2013.

[26] S. K. Vashist, “Non-invasive glucose monitoring technology in diabetes management: A review,” *Anal. Chim. Acta*, vol. 750, pp. 16–27, 2012.

[27] M. S. Wróbel, “Non-invasive blood glucose monitoring with Raman spectroscopy: Prospects for device miniaturization,” *IOP Conf. Ser. Mater. Sci. Eng.*, vol. 104, no. 1, 2016.

[28] D. M. Haaland and E. V. Thomas, “Partial Least-Squares Methods for Spectral Analyses. 1. Relation to Other Quantitative Calibration Methods and the Extraction of Qualitative Information,” *Anal. Chem.*, vol. 60, no. 11, pp. 1193–1202, 1988.

[29] K. P. J. Williams and N. J. Everall, “Use of micro Raman spectroscopy for the quantitative determination of polyethylene density using partial least-squares calibration,” *J. Raman Spectrosc.*, vol. 26, no. 6, pp. 426–433, 1995.

[30] M. Mathlouthi and D. Vinh Luu, “Laser-raman spectra of d-glucose and sucrose in aqueous solution,” *Carbohydr. Res.*, vol. 81, no. 2, pp. 203–212, 1980.

[31] P. D. Vasko, J. Blackwell, and J. L. Koenig, “Infrared and raman spectroscopy of carbohydrates.,” *Carbohydr. Res.*, vol. 23, no. 3, pp. 407–416, 1972.

[32] Scikit-learn: Machine Learning in Python, Pedregosa et al., JMLR 12, pp. 2825-2830, 2011.

[33] A. Kar and M. Chandra, “A Low-Cost , Portable Alternative for a Digital Lock- In Amplifier Using TMS320C5535 DSP,” *2015 Annu. IEEE India Conf.*, 2014.

[34] J. Lu, D. Pan, and L. Qiao, “The principle of a virtual multi-channel lock-in amplifier and its application to magnetoelectric measurement system,” *Meas. Sci. Technol.*, vol. 045702, no. iii, p. 11, 2007.